UNIVERSIDADE FEDERAL DO PARANÁ

ELOISA PEREIRA CARDOZO

ADDITIVE MANUFACTURING OF NIOBIUM AND NIOBIUM ALLOYS

CURITIBA

2023

ELOISA PEREIRA CARDOZO

ADDITIVE MANUFACTURING OF NIOBIUM AND NIOBIUM ALLOYS

Tese apresentada como requisito parcial para a obtenção do título de Doutora em Engenharia Mecânica, Setor de Tecnologia, área de concentração Manufatura, no Programa de Pós-graduação em Engenharia Mecânica, Universidade Federal do Paraná.

Orientador: Prof. Ana Sofia C. M. D`Oliveira
Co-orientador: Prof. Moataz Attallah

CURITIBA

2023

TERMO DE APROVAÇÃO

Os membros da Banca Examinadora designada pelo Colegiado do Programa de Pós-Graduação ENGENHARIA MECÂNICA da Universidade Federal do Paraná foram convocados para realizar a arguição da tese de Doutorado de **ELOISA PEREIRA CARDOZO** intitulada: **ADDITIVE MANUFACTURING OF NIOBIUM AND NIOBIUM ALLOYS**, sob orientação da Profa. Dra. ANA SOFIA CLÍMACO MONTEIRO DE OLIVEIRA, que após terem inquirido a aluna e realizada a avaliação do trabalho, são de parecer pela sua APROVAÇÃO no rito de defesa.

A outorga do título de doutora está sujeita à homologação pelo colegiado, ao atendimento de todas as indicações e correções solicitadas pela banca e ao pleno atendimento das demandas regimentais do Programa de Pós-Graduação.

CURITIBA, 13 de Março de 2023.

Assinatura Eletrônica
14/03/2023 15:56:44.0
ANA SOFIA CLÍMACO MONTEIRO DE OLIVEIRA
Presidente da Banca Examinadora

Assinatura Eletrônica
15/05/2023 17:35:53.0
FERNANDO JOSÉ GOMES LANDGRAF
Avaliador Externo (UNIVERSIDADE DE SÃO PAULO - USP)

Assinatura Eletrônica
14/03/2023 16:47:38.0
SERGIO LUIZ HENKE
Avaliador Interno (UNIVERSIDADE FEDERAL DO PARANÁ)

Assinatura Eletrônica
28/04/2023 16:59:42.0
OSVALDO CINTHO
Avaliador Externo (UNIVERSIDADE ESTADUAL DE PONTA GROSSA)

Assinatura Eletrônica
14/03/2023 16:15:47.0
SILVIO FRANCISCO BRUNATTO
Avaliador Interno (UNIVERSIDADE FEDERAL DO PARANÁ)

ACKNOWLEDGEMENTS

RESUMO

As ligas à base de Nióbio são consideradas as mais adequadas para substituir as ligas de Níquel na fabricação de componentes para a nova geração de aeronaves, já que as ligas de Níquel não conseguem mais atender aos requisitos de performance exigidos. O Nióbio é considerado um material estratégico para o avanço da tecnologia em nível mundial e o Brasil detém mais de 90% das suas reservas em todo o mundo. O desenvolvimento e viabilização da fabricação de componentes à base de Nióbio e suas ligas permitirá elevar a temperatura de operação de aeronaves, assim como a redução de peso dos seus componentes, aumentando sua performance. Embora a fabricação de ligas de Nióbio seja desafiadora, as técnicas de processamento por Manufatura Aditiva têm o potencial de realizá-la. Um processo aditivo bem conhecido é a Fusão a Laser em Leito de Pó (LPBF). A Deposição por Plasma por Arco Transferido (PTA-DED), amplamente utilizada para procedimentos de reparo e revestimento, também é uma técnica aditiva promissora para fornecer tais condições de processamento. Além disso, é a única técnica a arco que permite realizar a síntese *in-situ* de ligas durante a deposição de misturas de pós elementares. Tanto os equipamentos de LPBF quanto os de PTA-DED possuem um sistema de gás inerte que protege o material depositado, uma grande vantagem no processamento de materiais reativos como o Nióbio. Pouco se sabe sobre o processamento do Nióbio puro e suas ligas por técnicas aditivas, bem como as propriedades destes componentes finais. Esta investigação dá um passo importante para viabilizar o processamento de ligas de Nióbio, contendo compostos de siliceto de alta dureza e baixa tenacidade, realizando a síntese *in-situ* destes compostos durante o processamento de multicamadas.

Neste estudo, as técnicas LPBF e PTA-DED são exploradas para processar multicamadas de Nb e ligas de Nb com o objetivo de avaliar o impacto de diferentes complexidades de mistura de pós na síntese *in-situ*, nos caminhos de solidificação, na estabilidade aos múltiplos ciclos térmicos e na resistência à oxidação .

Palavras-chave: Plasma por Arco Transferido, Processamento com Mesa de Pós a Laser, Ligas de Nióbio, Nióbio puro, Manufatura Aditiva.

ABSTRACT

Niobium based alloys are considered the most appropriate to replace Nickel alloys for new generation aircrafts, because Nickel alloys can no longer meet the extreme environmental requirements. Niobium is considered a strategic material for the advancement of technology worldwide and Brazil holds more than 90% of its reserves worldwide. The development and feasibility of manufacturing components based on Niobium and its alloys will allow raising the operating temperature of aircrafts, as well as reducing the weight of its components, increasing their performance. Although the fabrication of Niobium alloys is challenging, the emerging Additive Manufacturing processing techniques have potential to overcome it. A well-known additive process is the Laser Powder Bed Fusion (LPBF). The striking feature of this process is the high geometry resolution and the high thermal gradients generated by the energy source. The Powder Plasma Transferred Arc Direct Energy Deposition (PTA-DED) widely used for cladding and coating procedures, is also a promising additive technique to provide such processing conditions. Furthermore, it is the only arc-based technique that allows to perform *in-situ* synthesis during the deposition of elemental powder mixtures. Both LPBF and PTA equipments have an inert gas system that protects the deposited material, a great advantage when processing reactive materials, such as Niobium.

Little is known about the processing of pure niobium and niobium alloys by additive techniques, as well as the properties of these additive parts. This investigation takes an important step to process sound Niobium alloys containing high hardness low toughness silicide compounds as multilayers, taking advantage of the *in-situ* synthesis of alloys during the processing of multilayers.

In this study, the LPBF and the PTA-DED techniques are explored to process Niobium and Niobium alloy multilayers aiming to assess the impact of different powder mixture complexities on the *in-situ* synthesis, solidification paths, stability to multiple thermal cycles and the oxidation resistance.

Keywords: Plasma Transferred Arc, Laser Powder Bed Fusion, Niobium alloys, pure Niobium, Additive Manufacturing.

LIST OF FIGURES

LIST OF TABLES

LIST OF SYMBOLS, ABBREVIATIONS AND ACRONYMS

CAPES – Coordenação de Aperfeiçoamento de Pessoal de Nível Superior

Finep – Financiadora de Estudos e Projetos

UK – United Kingdom

LPBF – Laser Powder Bed Fusion

PTA – Plasma Transferred Arc

DED – Directed Energy Deposition

AM – Additive Manufacturing

SEM – Scanning Electron Microscopy

EBSD – Electron Backscatter Diffraction

XRD – X-Ray Diffraction

TGA – Thermogravimetric Analysis

EDS – Energy Dispersive Spectroscopy

DoE – Design of Experiments

DBTT – Ductile to Brittle Transition Temperature

MMC – Metal Matrix Composite

LSF – Laser Solid Forming

TIG – Tungsten Inert Gas

HDH – Hydride Dehydride Process

EBM – Electron Beam Melting

EDM- Electric Discharge Machine

OM – Optical Microscopy

LAMSE – Laboratory of Additive Manufacturing and Surface Engineering

DSC – Differential Scanning Calorimetry

HIP – Hight Isostatic Pressure

BCC – Body Cubic Centered

T_m – Melting Point

λ_W – Thermal conductivity of Tungsten

λ_{Nb} – Thermal conductivity of Niobium

P - Power

v - Speed

h – Hatching Space

k – Conductivity

Nb_{ss} – Niobium Solid Solution

$T_{deposition}$ – Deposition Temperature

$T_{remelting}$ – Remelting Temperature

$T_{reheating}$ – Reheating Temperature

Ti_{ss} – Titanium Solid Solution

TABLE OF CONTENTS

1. INTRODUCTION

1.1. CONTEXT AND PROBLEM

For many years refractory alloys were explored with the aim to design high-strength alloys for very high temperatures. Niobium (Nb) is considered the most promising refractory metal due to its low ductile-to-brittle transition temperature (DBTT), relatively low density ($8,48g/cm^3$) and high melting point (2745^oC) (BEDFORD et al., 1996; SHABALIN, 2014). However, the poor fabricability and low oxidation resistance still impose many challenges (PHILIPS; CARL; CUNNINGHAM, 2020).

The development of Additive Manufacturing (AM) techniques, together with new software and computational methods, make the manufacture of Niobium based refractory components increasingly possible (GHOSH; OLSON, 2007). Also, in-situ synthesis of low toughness compounds during the deposition of elemental powder mixtures may bring an alternative route to process additive manufactured refractory parts (CARDOZO; D'OLIVEIRA, 2022). However, the literature lacks studies exploring the potential of additive techniques as a path to process Niobium and Niobium alloys. A sound understanding on the behaviour of pure Niobium processed by AM techniques can offer an opportunity for optimizing advanced niobium-based alloys.

Pure Nb is a versatile material that finds applications in aerospace, chemical, nuclear, electronic and medical industry. The mechanical properties of niobium and niobium alloys can be highly influenced by the presence of relatively small amounts of interstitial impurities. Therefore, combining ductility, strength, toughness, and oxidation resistance, mainly when working at high temperatures, is challenging (KIM, Jin Hak et al., 2004; KONG et al., 2016; LORIA, 1987; SANKAR; BALIGIDAD; GOKHALE, 2013; SHEFTEL; BANNYKH, 1994; YANG et al., 2019).

Pure Niobium can also be used to fabricate Metal Matrix Composites (MMCs), using a Nb based matrix reinforced with hard particles with improved properties, such as wear resistance (ARRAVIND et al., 2020). Typical reinforcements used in MMCs are SiC and WC particles (CHAWLA; CHAWLA,

2006). However, to achieve high performance at high temperatures, alloying Niobium is mandatory.

MATHIEU et al. (2012) reported that silicon is the most suitable alloying element to be added to Niobium due to a two-fold effect: the formation of silica scale at high temperatures and the synthesis of silicide compounds, improving oxidation and creep resistance, respectively. High strength silicides, together with a ductile Nb-based solid solution, provide a tough material with good balance between high and low-temperature strength. KIM, Won-Yong et al. (2001) mentioned that the Nb–Si alloy system can provide good *in-situ* composites, with a variety of microstructures and properties. Complex systems with enhanced properties can be achieved by alloying Nb with Ti, Al, Hf, and Cr.

Powder Additive Technologies might allow *in-situ* synthesis of complex alloys during the deposition of elemental powder mixtures. Directed Deposition Additive processes also allow to gradually change composition layer by layer to build a functionally graded component. Furthermore, the layer-by-layer approach offers high geometric complexity and material usage efficiency. Few studies have been published on AM of pure Niobium and Niobium alloys, but results confirmed AM as a promising approach for processing these materials (ALLEN, A. *et al.*, 2019; GUO *et al.*, 2018; PHILIPS; CARL; CUNNINGHAM, 2020). Furthermore, to the best of our knowledge, there are no published studies on Powder Plasma Transferred Arc Additive Manufacturing for Niobium alloys.

This study will explore Niobium and Niobium alloys processed with powder bed fusion and directed energy deposition additive techniques, namely Laser Powder Bed Fusion (LPBF) and Powder Plasma Transferred Arc (PTA-DED). Solidification structures, stability, and oxidation resistance of multilayers processed with these two techniques will be analysed and discussed. The fabricability of pure Niobium, Niobium-based MMCs, and Niobium-silicide based alloys is assessed.

1.2. GENERAL OBJECTIVES

The main objective of this study is to assess the fabricability of Niobium and Niobium alloys processed by additive manufacturing techniques, evaluating

the solidification sequence and oxidation resistance of processed multilayers. In particular, this research focuses on the follow targets:

1.3. SPECIFIC OBJECTIVES

1- To establish the correlation between processing parameters and multilayers features of pure Nb, Niobium-based MMCs;

2- To comprehend the solidification sequence and the impact of thermal cycling of multilayers of Niobium-silicide based alloys obtained *in-situ* during multilayer processing of elemental powder mixtures;

3- To understand how the powder mixture complexity interferes on *in-situ* synthesis of Nb silicide alloys and metallurgical stability of the multilayers processed by PTA-DED;

4- To assess the role of alloying elements Ti, Si, Al, Zr, and Cr on the oxidation resistance of multilayers;

5- To discuss the effectiveness of the gas shield of PTA-DED on mitigating the oxygen solubility into the molten pool.

2. LITERATURE REVIEW

Little is known about AM for Niobium and Niobium alloys, hence a brief review on AM for refractory materials is the start to better understand motivations, constraints, and to assess where pure Niobium and Niobium alloys fit .

2.1. REFRACTORY METALS

The space race and the defence industry boosted the research on refractory materials from 1950 to 1976 as recently mentioned by (PHILIPS; CARL; CUNNINGHAM, 2020). The design of many refractory alloys was put forward from this period and some alloys are still being used. This is the case of C103 (Nb-10Hf-1Ti) Nb based alloy that became a major alloy in the marketplace because of its excellent fabricability, measured by how easy it is to transform an ingot to a sheet or other semi-finished product. A lot of effort was put into designing other functional and cost-effective refractory alloys, but high melting points and poor oxidation resistance were always the main withdraws. The fabrication of these alloys is costly and difficult, hence the advantages for the application must be significant. These challenges frustrated the promise on refractory alloys and, around 1976, an abrupt discontinuity on the research with these materials occurred.

Motivations for a change in this scenario starting to rise from land-based gas turbines and air-craft engines, where increasing the combustion temperature and decreasing materials density generally leads to efficiency improvements. The efficiency can also be improved by reducing the cooling air demand. For both conditions, an increase in metal temperature capability can improve the performance. More recently, the increased need for thermal efficiency of high-temperature equipment, together with a more severe environmental legislation that imposes carbon emission reduction, has fuelled the search for materials that can withstand very high-temperature conditions. It brings back the refractory alloys as interesting materials. New manufacturing technologies enhanced with new software and computational methods, are opening new possibilities for refractory metals.

High-temperature applications have long used Nickel-based alloys. However, above 1100°C, metallurgical degradation and high oxidation rates compromise even the most advanced Nickel superalloy, which melt at approximately 1350°C (BEWLAY; JACKSON; ZHAO; SUBRAMANIAN, 2003). In this industrial scenario, refractory alloys stand out as a competitive alternative due to the ability in keeping properties at higher temperatures.

The targets for oxidation resistance of the new alloys are set for short term and long-term. The short-term target is to achieve a mass-loss lower than 200μm after 10h at 1370°C. The long-term target is to make available alloys that exhibit a mass-loss less than 25μm following exposure for 100h at 1315°C. This mass loss is the same as that of the second-generation Ni superalloys at 1150°C (BEWLAY; JACKSON; ZHAO; SUBRAMANIAN; et al., 2003). From 1998 to 2000, developments on refractory alloys offered 10 times increase in oxidation resistance. (BEWLAY; JACKSON; ZHAO; SUBRAMANIAN; et al., 2003) reported that in 2003 Nb-silicide-based composites offered mass loss lower than 25um after 100h at 1200°C. However, a lot of effort has been made to achieve the long-term 1315°C oxidation-resistance goal together with the rupture fatigue, fatigue strength and fracture toughness goals.

Refractory metals can be manufactured by arc-cast, powder metallurgy, spark plasma sintering, chemical vapor deposition, and hot isostatic pressure. However, when there is a need to manufacture high hardness components with complex structures, these previously mentioned technologies are limited. Additive Manufacturing of refractory metals will allow increasing design complexity and material efficiency together with its advantageous high-temperature properties.

Compared with other refractory materials, Niobium has a set of properties that can make it stand out for AM. However, in order to better apply it for new technologies, it is mandatory to review basic concepts, historical constraints as well as understand different approaches to explore applications for Nb-based alloys.

2.2. NIOBIUM PROPERTIES AND CHALLENGES

Among the refractory materials, Niobium has the lowest density (8,58g/cm^3), lower Ductile to Brittle Temperature Transition (DBTT), higher solubility of interstitial elements, and is considered the most suitable to be used under ultra-high-temperature applications, where Ni-superalloys are no longer functional (SHEFTEL; BANNYKH, 1994). Since the end of 1960, the need for new structural materials suitable for aerospace applications, with high-temperature strength, good workability, and low density, focused the attention on Nb-based alloys (BARRETT; COREY, 1960; SMITH, 1960). Recently, the use of Nb alloys was also extended to other fields such as nuclear and chemical industries, heat exchangers, and electronic components (MURAYAMA; HANADA, 2002).

The mechanical properties of niobium alloys can be highly influenced by the presence of even relatively small amounts of interstitial impurities, such as oxygen. The oxygen, as an interstitial solute atom in the body-centered cubic structure site causes a considerable distortion in crystal lattice, interacting with dislocations and causing a pinning effect, increasing the hardness and yield strength. Furthermore, if the solute concentration is above the equilibrium solubility, brittle oxide phases might precipitate (SANKAR; BALIGIDAD; GOKHALE, 2013; YANG et al., 2019).

Enabling industrial applications of niobium finds two major challenges: poor workability and low oxidation resistance. The former is related to restrictions imposed by conventional manufacturing methods, such as the need for expensive and complex casting molds (BALSONE et al., 2001; MENG et al., 2018). Alloy ductility, strength, toughness, and oxidation resistance, mainly when working at high temperatures, is a big challenge (KIM, Jin Hak et al., 2004; KONG et al., 2016; LORIA, 1987; SANKAR; BALIGIDAD; GOKHALE, 2013; SHEFTEL; BANNYKH, 1994; YANG et al., 2019)

The low oxidation resistance of Nb alloys is associated with the high solubility of oxygen at high temperatures, the high diffusion rate of oxygen in niobium, and high reactivity of niobium with oxygen (FROMM; JEHN, 1969; LAING, 2001; SANKAR; BALIGIDAD; GOKHALE, 2013). Due to the high

22

solubility and diffusion coefficient of oxygen in niobium at high temperatures, oxygen can be easily captured in the liquid niobium metal during manufacturing, which will impair final properties. At room temperature, the mentioned distortions in the crystal lattice interact with both edge and screw dislocations resulting in a pinning effect helping to increase the dislocation density stored and the yield strength (SANKAR; BALIGIDAD; GOKHALE, 2013; YANG *et al.*, 2019). To mitigate the influence of trapped oxygen, the components might be processed in argon atmosphere.

Furthermore, the Nb_2O_5 oxide have low stability at high temperatures compromising its role as a protective oxide film . Because of the higher diffusion of oxygen anions, the Nb_2O_5 oxide have a growth rate 3 times higher compared to SiO_2. It contributes to form a non-protective oxide scale that impairs the oxidation resistance of niobium-based alloys even at temperatures as low as 500°C (GUPTA, 1993; MITRA, 2019; TIETZ; WILSON, 1965).

It is possible to improve Nb oxidation resistance both by using oxidation-resistant coatings or adding alloying elements. The latter is related to the ability of other elements to form a dense, adherent, regenerative, and slow growth rate oxide scale on a bulky material (BARRETT; COREY, 1960). This approach is of significant relevance because, in case of failure of the coating, it might ensure the good performance of the structural material. To preserve niobium solid solution and other phases in the microstructure of the bulky material it is recommended the addition of preferentially oxidizing elements that can produce protective oxide scales. However, the addition of solutes atoms will decrease the melting point of the alloy and, therefore, it is of relevance to guarantee an appropriate balance of properties to maintain the competitiveness of the material. The addition of Si in Nb alloys has been widely explored to improve oxidation resistance while maintaining other properties (BACH, 2009; BARRETT; COREY, 1960; MURAKAMI *et al.*, 2001).

Regarding the manufacturing of pure Niobium and Niobium alloys, including Nb-Si alloys, the high solubility of oxygen in Nb at high temperatures, together with the high melting point and low toughness, is a challenge for conventional manufacturing. When processing Nb alloys at high temperatures, the high solubility of oxygen in Nb retains oxygen in solid solution, which might

induce internal oxidation (MATHIEU *et al.*, 2012). Hence, these alloys must be manufactured in a reduced or non-oxygen environment (DYMEK *et al.*, 2003; GHOSH; OLSON, 2007; KIM, Jin Hak *et al.*, 2004). The high melting point of Nb makes conventional manufacturing processes that rely on melting require expensive and complex die casting molds, which is less competitive. Also, the low toughness and high hardness of intermetallic compounds in the microstructure of refractory alloys, such as Nb-Si alloys, might compromise manufacturing by conventional techniques such as forging, forming, and milling (WANG, Yan Hang *et al.*, 2006; WESTBROOK; FLEISCHER, 2013).

In-situ alloying during the deposition of powder mixtures has been proved to successfully process coatings with tailored properties (ALMEIDA *et al.*, 2011; CANGUE; D'OLIVEIRA, 2010). Extrapolating these procedures to the processing of parts layer by layer offers an opportunity to manufacture hard and complex alloys. This additive approach also offers the possibility to design a composition/property gradient in a multilayered component. However, little has been assessed regarding Nb-based alloys additive manufactured for high-temperature components. This study contributes to this challenge exploring the processability of multilayers of Nb based materials by additive techniques.

2.3. NIOBIUM SILICIDE-BASED ALLOYS

Since the early 1990s, alloys based on Nb intermetallic compounds are seen as potential candidates for high-temperature structural applications (MENDIRATTA; LEWANDOWSKI; DIMIDUK, 1991; SHEFTEL; BANNYKH, 1994). Silicon is considered the most suitable alloying element to be added to Niobium. Its effects are two-fold, forming silica at high temperatures and silicide compounds, improving oxidation and creep resistance. The SiO_2 oxide is stable at higher temperatures than Al_2O_3 and the lower activation energy for oxygen diffusion in silica make it also more effective than alumina at higher temperatures (PERKINS; CHIANG; MEIER, 1987).

Intermetallic compounds have a complex crystal structure, large unit cell size, and restricted slip systems, leading to intrinsic brittleness (KIM, Won-Yong *et al.*, 2001). To improve the fracture toughness of Nb/Si alloys, it is possible to

incorporate ductile phases, named "ductile phase toughening". Niobium solid solution is frequently used as a ductile matrix that accommodates the brittle silicide phases (MATHIEU *et al.*, 2012; MURAYAMA; HANADA, 2002). Nb–Si alloy system has a wide two-phase region where Nb_5Si_3 and the ductile Nb solid solution (Nbss) can coexist offering a variety of microstructures and properties to produce "*in-situ*" composites (KIM, Won-Yong *et al.*, 2001). The Nb-silicide based alloys with the mentioned composite like features are usually explored for compositions in the range from 12 to 25 at% Si, indicated in Figure 1, because there is intrinsic thermodynamic stability of the phases in these alloys which is a critical feature for long-term applications at high temperatures (BEWLAY; JACKSON; ZHAO; SUBRAMANIAN, 2003). It also helps to find a balance between high and low-temperature strength (BEWLAY; JACKSON; ZHAO; SUBRAMANIAN, 2003; MATHIEU *et al.*, 2012).

However, the addition of alloying elements to niobium-silicide alloys is considered mandatory to reach physical and chemical properties required for high-temperature applications (MATHIEU *et al.*, 2012). Many studies report that Al can increase the toughness of Nb/Si alloys, even at high temperatures, and also improve the oxidation resistance of niobium solid solution (Nbss) (CHUNG; ENOKI; KISHI, 2002; MURAYAMA; HANADA, 2002). Literature reports low weight gain for alloys built by spark plasma sintering with the composition Nb47Si20Al (at%) as well as the formation of a thin adherent Al_2O_3 at 1300°C (MURAKAMI *et al.*, 2001).

BEWLAY; JACKSON; ZHAO; SUBRAMANIAN; et al. (2003) reported that the processing-microstructure-property relationship for Nb-silicide-based composite-like alloys have not been sufficiently well defined, but they already know that the experience with the fabrication methods indicated that processing these materials is very difficult. However, other studies show some compositional trends to optimize properties such as toughness, oxidation, and creep resistance. This knowledge has been the driving force for the investigation of many alloys aiming to better understand the effect of processing technique on microstructure and properties. Nb-Si alloys containing Ti, Al, Hf have shown impressive gain in oxidation resistance by about an order of magnitude because Ti, Al and Hf oxides,

as alloying elements, have lower free energy of formation compared to SiO_2 (MITRA, 2019).

Figure 1 - Binary Nb-Si phase diagram representing the basis for the development of Nb-Si-based composites.
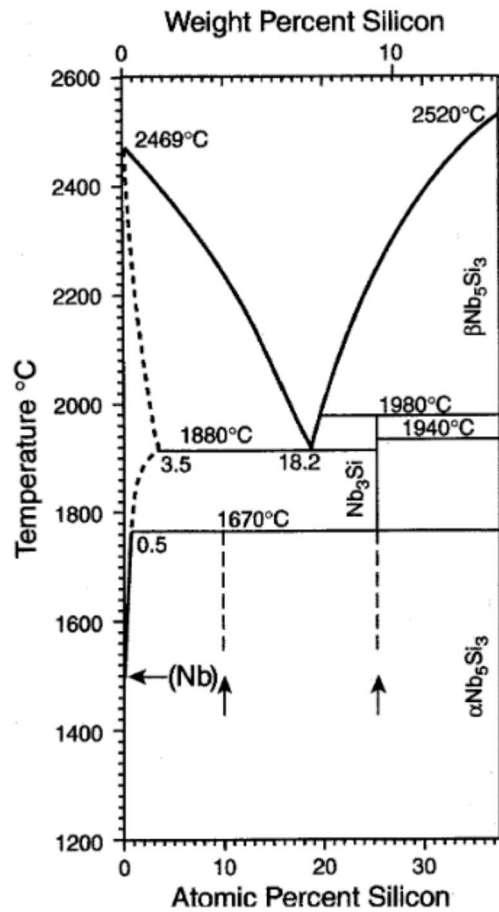
SOURCE: Bewlay et al. (2003).

MENON; MENDIRATTA; DIMIDUK (2001) reported that when Al is added to Ti-free Nb-Si alloy it results in eutectic solidification (Nbss + Nb_5Si_3) and usually the Nbss/eutectic interface oxidizes preferentially compared to niobium silicide. Zr, Cr and Mo alloying elements are considered to provide additional performance to Nb-Si alloys. These are known as Nb-Si based multicomponent alloys (MITRA, 2015). The addition of Ti can improve the fracture toughness of Nb-Si alloy (MURAYAMA; HANADA, 2002). However, to ensure the high melting temperature of Nb-Si based alloys, the content of Ti is generally required to be less than 25at.%. The addition of Zr to Nb-Ti-Si alloy improves the room

temperature toughness, hardness, and yield strength, but further studies should be carried out to clarify the role of Zr in this alloy (LI, Yunlong et al., 2019). The oxidation resistance of Nb-Si alloys can also be improved by the addition of Cr and/or Al at the expense of mechanical properties due to the increased ductile-brittle transition temperature and the decrease in melting point (GUO et al., 2018b; PHILIPS; CARL; CUNNINGHAM, 2020).

Studies show that on Nb-24Ti-16Si-2Hf-2Al-10Cr and Nb-24Ti-16Si-2Hf-6Al-17Cr alloys, the mass gain of alloy with higher Al content was seven times lower after exposure at 1200°C for 100h. The oxidation kinetic followed a parabolic rate law and the oxides $CrNbO_4$, $TiNb_2O_7$ and SiO_2, made the oxide scale dense, compact, and protective (MITRA, 2019).

The General Electric Company has developed a composite with the composition Nb–25Ti–2Cr–8Hf–16Si–2Al (at%) that has become the main alloy for research in many countries (KARPOV et al., 2019). This alloy has a fracture toughness of 18,2-23,3 MPa $m^{1/2}$, which meets the minimum requirements of fracture toughness value of 20 MPa $m^{1/2}$ when fabricated with the directional solidification technique (WANG, Qi et al., 2022).

However, in order to further improve the properties of Nb-Si based alloys, other studies are being developed using the Nb–25Ti–2Cr–8Hf–16Si–2Al (at%) alloy composition as a reference. QIAO; GUO; ZENG, (2017) reported that the oxidation resistance at 1250°C of these Nb-Si based alloys can be improved by Zr addition. Considering also that Zr is chemically similar to Hf, WANG, Qi et al. (2022) substituted the Hf content in Nb–25Ti–2Cr–8Hf–16Si–2Al (at%) alloy by Zr. The author highlights that Zr can further improve the room temperature fracture toughness, reduce the density and the cost of Nb-Si based alloys since Zr is cheaper and lighter than Hf. The addition of Mo, in turn, can improve the fracture toughness of Nb-Si based alloys by increasing the continuity of Nbss matrix, can promote the solid solution strengthening of Nbss to higher temperatures.

Powder additive techniques may facilitate the development and fabrication by in-situ synthesis of complex Nb based alloys using elemental powder mixtures. These techniques might also allow to build functionally graded materials varying the composition layer by layer.

2.4. METAL MATRIX COMPOSITES

Metal Matrix Composites (MMCs) fit into the group of advanced materials and present unique properties not seen in monolithic ceramics or metals. Like all composites, MMCs consist of at least two chemically and physically distinct phases distributed to provide properties not provided by the individual phases. The matrix can be a metal or a metallic alloy. Typically, MMCs are reinforced with either particles, short fibers, or continuous fibers, as show Figure 2 (CHAWLA; CHAWLA, 2006).

Comparing metallic composites and polymer composites, MMCs offer the following advantages: major weight savings due to higher strength-to-weight ratio; dimensional stability; high-temperature stability; improved cyclic fatigue performance. It is common to find MMCs reinforced with oxides or carbides. Table 1 shows the most frequently used reinforcements. Ceramic particles are widely used and are the most common reinforcements in surface cladding layers as well as in MMCs. The particle size used as reinforcement varies from 1 μm to 1000μm (CHAWLA; CHAWLA, 2006)

Figure 2 - Different types of metal matrix composites.
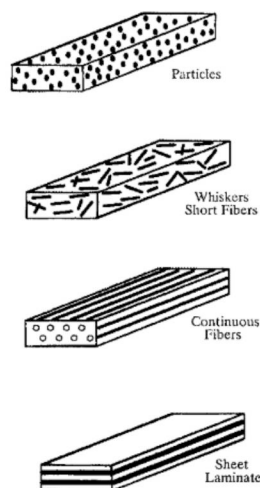
SOURCE: (CHAWLA; CHAWLA, 2006).

Table 1 - Typical Reinforcements Used in Metal Matrix Composites.

Type	Aspect Ratio	Diameter [μm]	Examples
Particle	1-4	1-25	SiC, Al_2O_3, BN, B_4C, WC
Short Fiber or whisker	10-10000	1-5	C, SiC, Al_2O_3, $Al_2O_3+SiO_2$
Continuous Fiber	>1000	3-150	SiC, Al_2O_3, C, B, W, Nb-Ti, Nb_3Sn

Source: (CHAWLA; CHAWLA, 2006)

MMCs based on refractory materials are difficult to manufacture by casting (LIU *et al.*, 1994). The additive manufacturing offers a path to fabricate these alloys, allowing to build components layer by layer using a powder material like in powder bed fusion processing. This study will explore the effect of the addition of WC ceramic particles in pure Niobium. Phase diagram in Figure 3 show the maximum temperature at which WC particles remain stable.

Figure 3 – W-C phase diagram.
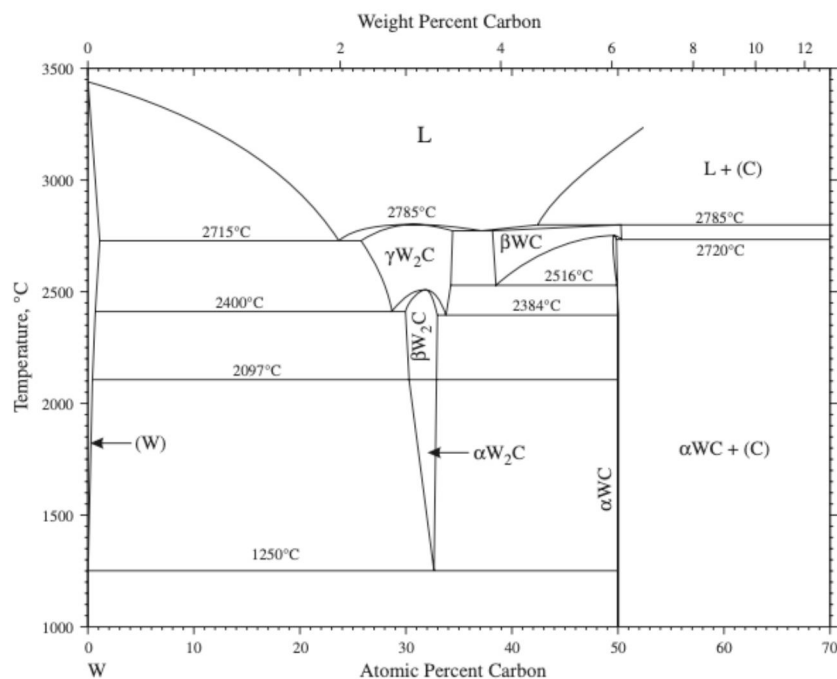
Source: OKAMOTO (2008)

To better understand the contribution of the reinforcement, it is important to know its basic properties. The melting point allows to predict if it can easily dissociate during the additive process. Table 2 shows relevant properties for these ceramic particles (LOVRIĆ *et al.*, 2019). They are known to increased wear resistance and are expected to reinforce the Niobium metal matrix mainly by dislocation pinning and grain refining, at room temperature.

Table 2 - Properties of the WC ceramic.

Property	Tungsten Carbide
Density [g/cm³]	WC = 15,63
Melting point	WC = 2870°C
Thermal conductivity [W/mK]	63
Thermal expansion [.10^{-6}/K]	a = 5,2 b = 7.3
Hardness [HV]	2243

2.5. ADDITIVE MANUFACTURING

The processing technique also plays a big role on features and performance of alloy. According MULSER; SEEMÜLLER (2014), until 2014, the processing techniques to manufacture Nb-Si alloys were mainly casting, directional solidification, arc melting and subsequent extrusion, physical vapor deposition and hot extrusion of gas atomized powders. Authors also highlight that to fabricate near-net shape Nb-Si components for industry is a challenge.

LI et al. (2019b) observed the fracture toughness of different Nb-16Si based alloys prepared by different processing techniques, Figure 4, and highlighted that the fracture toughness of Nb-22Ti-16Si-2Hf-2Al-2Cr alloy prepared by arc melting is higher that prepared by reactive hot press sintering. Furthermore, the higher fracture toughness was achieved by the alloy Nb-22Ti-

16Si-5Zr processed by Laser Direct Deposition Metal Additive Manufacturing, called by the author as Laser Solid Forming (LSF).

Figure 4 - Fracture toughness of Nb-16Si alloys prepared by different process techniques.
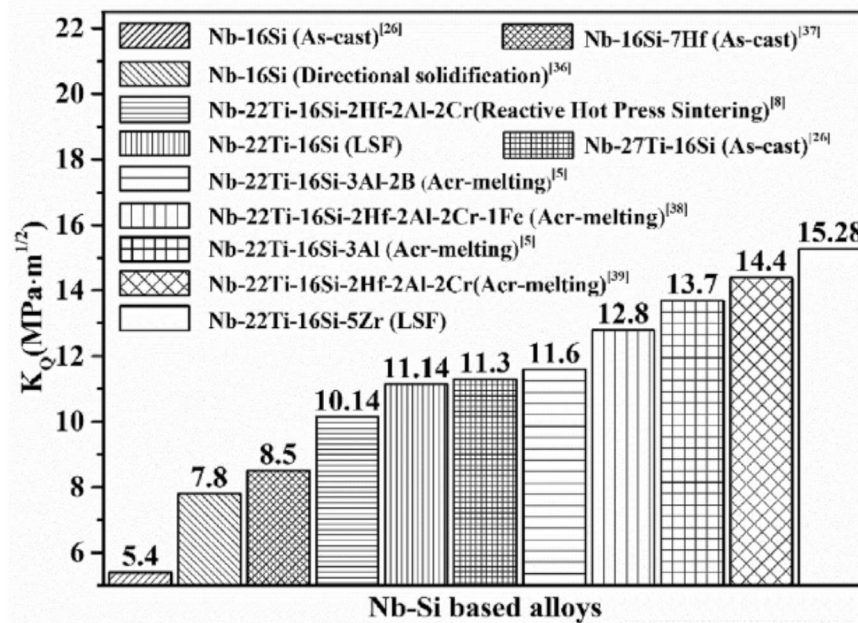
Source: LI et al. (2019)

Additive manufacturing technologies are emerging to meet industrial demands such as cost reduction by eliminating tools, reducing material waste, manufacturing steps, and fabricate components with high geometrical complexity. The common feature between these techniques is the build of a component layer by layer, whereas many features can differentiate them such as the nature of the energy source, the type of feedstock material, and the way the material is placed against the energy beam.

This study explores two technologies that allow performing additive manufacturing: Powder Plasma Transferred Arc (PTA-DED) and Laser Powder Bed Fusion (LPBF). Both techniques use powder as feedstock but differences such as powder particle size, energy source, and equipment size account for differences in the final component, such as in layer width, as show Figure 5, and in the solidification structure.

Figure 5 - Layer thickness resulted by different AM techniques.
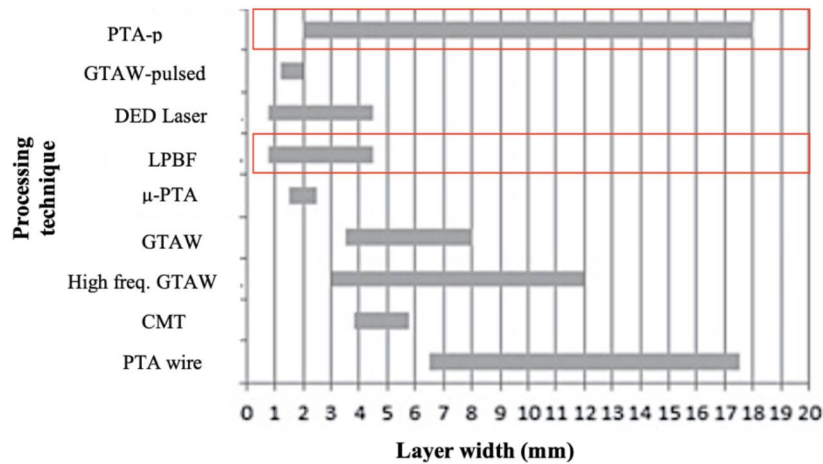
2.5.1. Powder Plasma Transferred Arc

The Plasma Transferred Arc is widely used for coating components to increase wear resistance, corrosion resistance, and high-temperature performance (SINGH; JAIN, 2015). This is the only arc process that uses powder feedstock and has proven to successfully *in-situ* synthesize Nb-Si binary alloys (CARDOZO; D'OLIVEIRA, 2022). On the Additive Manufacturing approach, PTA-DED emerges in a competitive processing window where high deposition rates (up to 100g/min) and large components can be obtained compared to other powder DED techniques (WITHERS; BHADESHIA, 2001).

In this system, the powder is conducted through the nozzle towards the plasma arc that melts the powder that solidifies on a substrate as a dense layer. Successive layers can be deposited until the desired volume is fabricated. As feedstock, either atomized, pre-alloyed or elemental powder mixtures of can be used. It is also possible to use powders with irregular morphology. The system also allows to use a wide range of particle size: from 50 to 180 um (CARDOZO; D'OLIVEIRA, 2022). The workpiece can remain stationary while the arc is moving or vice-versa. An example of application of this system is the reconditioning of worn or damaged components (FRAZIER, 2014). In powder-fed PTA-DED

processes, alloys can be produced *in-situ* with composition variations in strategic regions of the component. To better take advantage of this technique for Additive Manufacturing, understanding the basic concepts is required.

The term plasma designates a state of matter resulting from the ionization of a gas that becomes sufficiently heated to the point of becoming ionized, made up of free ions and electrons in equilibrium. The gas ceases to be insulating and starts to conduct an electric current. The higher the degree of ionization, the higher the plasma temperature and the lower the electrical resistivity. This reduced resistivity is used by the plasma welding process to transfer a high current intensity to the parts, generating heat and melting the material.

Figure 6 illustrates a PTA torch (BOULOS; FAUCHAIS; PFENDER, 2017). The ignition of the arc requires the aid of a primary pilot arc that, under the presence of ionized gas flow, has the unique function of creating an electrical conduction path between the electrode and the workpiece, allowing the ignition of the main plasma arc. The plasma arc is formed when a gas flow (plasma gas) is continuously fed into a torch through a cavity that has a non-consumable tungsten electrode positioned concentrically. The gas is heated by the intense heat generated by the pilot arc and is ionized generating the plasma. The pressure generated by the gas flow and the effect of a thermal expansion near the torch nozzle releases the plasma throughout a constricted orifice at high speeds, being collimated. Another gas flow, called shielding gas, is used to protect the weld pool against the ambient atmosphere and a third gas systems is used to carried out the feedstock into the plasma arc.

The plasma welding process is like the TIG (Tungsten Inert Gas) process, except for the constricted arc that increases the mechanical effects on the melt pool with an arc pressure about 6 to 10 times greater than that of an equivalent unconstrained arc. Using a constricted arc, the area of incidence is reduced, which leads to an energy concentration three (3) times higher. The higher speed of the plasma jet makes it more rigid, which guarantees greater stability to disturbances and better driveability during the depositions (REIS and SCOTTI, 2007).

Figure 6- PTA torch with details of its operation.

The formation of a weld bead depends on both thermal and mechanical effects. Thermal effects are related to two phenomena: thermal coupling between the electric arc with the substrate material, and gas ionization enthalpy. From a thermal point of view, what is expected is that the more intense the heat reaching the part, the greater the melted volume. This heat is proportional to the current intensity and inversely proportional to the welding speed. Regarding the mechanical effect, the impact and influence of the plasma jet on the liquid metal might be considered. It is expected that a high plasma gas flow and density will promote high mechanical action on the melt pool, as well as an increase in the current intensity. Typically, the plasma gas flow ranges from 0.25 to 2.5 l/min and the shielding gas from 10 to 30 l/min.

Mechanical effects on the liquid metal might be better understood by looking at the forces acting on the melt pool. The movement of the fluid in the melt pool can happens in four ways: by the Buoyancy force, by the convection induced by the Lorentz force, by the shear stress induced by the fluid surface tension gradient, and by shear stress induced by the plasma jet, as show Figure 7 (KOU, 2002). The ability to produce a low-dilution coating without porosity and flexible layer thickness, allows PTA to generate a high-quality product using less material and less energy input (AMERICAN ROLLER COMPANY, 2015).

Figure 7 - Driving forces for convection in melt pool: buoyancy force (a, b); Lorentz force (c, d); shear stress caused by differences in surface tension (e, f); shear stress caused by the plasma arc (g, h).
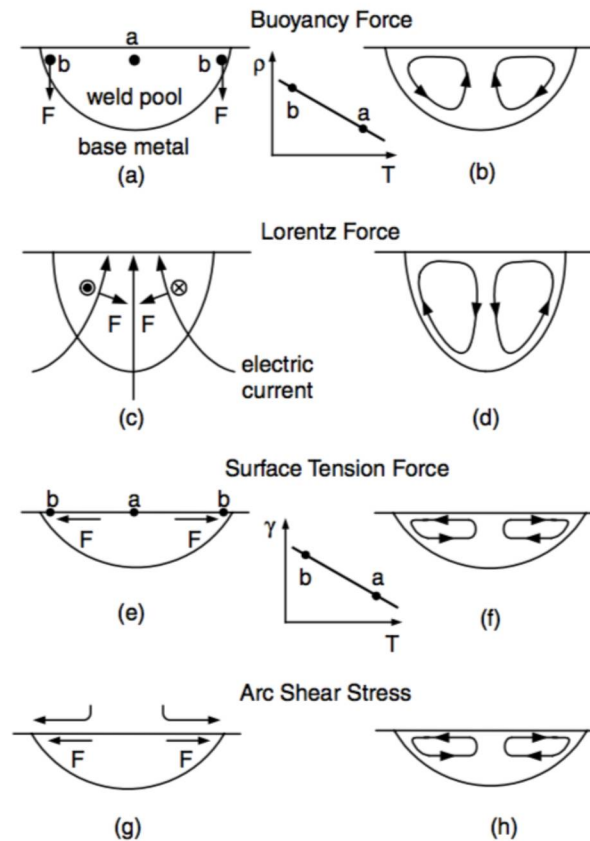
Source: KOU (2002)

From a point of view of solidification of the material being deposited, when building components layer by layer, these forces acting on the melt pool can account for segregation, as well as incorporation of inclusions and other defects that might lead to failure of components.

PTA-DED is the only technique that allows performing Powder Arc Additive Manufacturing. However, the literature lacks studies on Powder Plasma Transferred Arc (PTA-DED) and refractory alloys. The possibility to fabricate complex Nb alloys using PTA-DED *in-situ* synthesis open new possibilities for manufacturing of Niobium and Niobium-silicide based alloys.

2.5.2. Laser Powder Bed Fusion

In Laser Powder Bed Fusion (LPBF) processing, also known as Selective Laser Melting (SLM), the powder is first spread over the working area. The energy source (laser) emits energy to the powder bed and locally melt or sinter the powder according to a pre-defined geometry. After melting each layer, a powder recoater removes the excess powder and spreads a new thin layer of powder. The process is repeated multiple times until the component is finished. Powder grain size is within the range 10-60μm, and the process has a strong dependence on the feedstock features (DEBROY *et al.*, 2018). LPBF process allows to build components with high resolution, high dimensional control, and high geometric complexity, including internal channels. Figure 8 illustrates the LPBF process.

Figure 8 - Schematic of an Additive Manufacturing system that uses a powder bed.
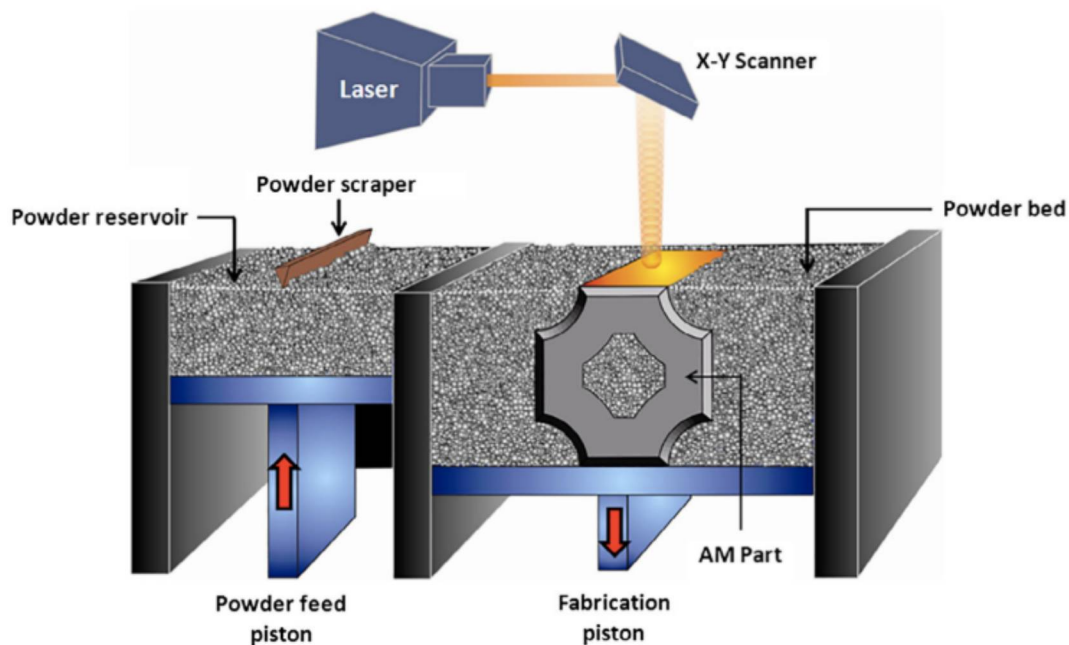
Source: SOLA; NOURI (2019)

LPBF of pure refractory metals has been explored in recent years. However, the knowledge regarding the relationship between process parameters and microstructure evolution, mandatory to improve components performance, is still very limited. The intrinsic properties of these materials can contribute to the

formation of defects such as balling and lack of fusion, usually caused by inhomogeneous heating. To mitigate these defects, careful control of process parameters is mandatory (ZHOU *et al.*, 2015). Figure 9 shows the interaction between the energy source and the powder bed.

Figure 9 - Schematic representation of the interaction between energy beam and powder bed.
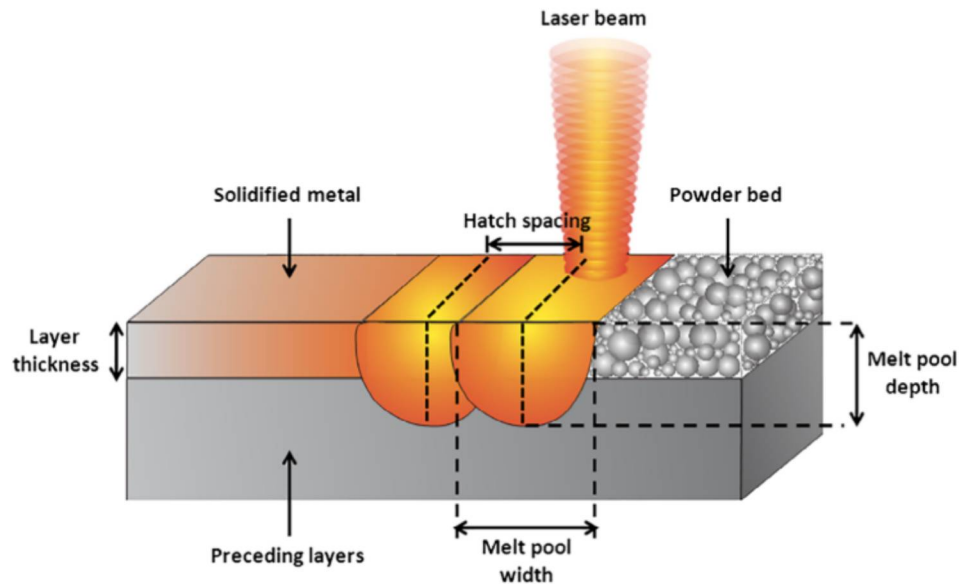
Source: SOLA; NOURI (2019)

The high melting point and high heat conductivity of refractory metals, leading to a fast cooling due to the high heat flow increases the challenge of processing. These phenomena affect the wettability hence the densification of parts (BRAUN *et al.*, 2019; FAIDEL *et al.*, 2015). With the aim to enable fabricability, studies investigate the processing parameters that allow to obtain fully dense tungsten parts, avoiding keyhole pores, splash, and to ensure the wettability to guarantee a good metallurgical bond with the neighbouring scanning tracks. Literature report that laser speed plays an important role ensuring the consolidation of the part because it is a path to control and increase the energy density (GUO, Meng *et al.*, 2019).

Studies on both tungsten and molybdenum show that these refractory metals face similar challenges when processed by LPBF. Both form coarse

columnar grains combined with weak grain boundaries due to the segregation of oxygen. Also, LPBF processing of molybdenum parts shows that the main challenge are hot cracks related to oxygen impurities that weaken grain boundaries and elevate the Ductile-to-Brittle Transition Temperature (DBTT) (KASERER *et al.*, 2019). The oxygen can also influence the presence of oxides related to nucleation sites for pores (KASERER *et al.*, 2019).

Compared to other refractory materials, Niobium has interesting properties that make it stand out. The melting point of pure niobium is the lowest within the refractory materials (2468°C) and it has the lowest thermal conductivity, which might contribute for a better processability by LPBF. Furthermore, the low density, high low-temperature ductility, higher solubility of interstitial elements put it among the most suitable alloys to work at ultra-high temperature applications where the Ni-superalloys are no longer functional (SHEFTEL; BANNYKH, 1994). The use of Nb alloys has been also extended to fields such as heat exchangers, electronic components, nuclear, aerospace, medical and chemical industries (MURAYAMA; HANADA, 2002).

Recently, few studies on Niobium additive manufactured have been published. However, the understanding of the relationship between processing parameters and microstructure evolution is still very limited and further research on the behavior of the niobium solid solution LPBF parts may pave the way for the optimization of advanced niobium-based alloys. The feedstock quality can also be a challenge for powder-based additive processes. The Niobium powders available as feedstock for powder-based additive processes are usually fabricated by Hydride Dehydride Process (HDH). Typically, resulting in particles with irregular morphology, which may impact the flowability in powder bed, as reported for pure niobium irregular powder when working with Electron Beam Melting (MARTINEZ *et al.*, 2013).

2.5.3. Important features of Additive Manufacturing

A very important and unique feature of AM is the effect of multiple thermal cycles on the microstructure of the final component. As AM is carried out layer by layer, each layer undergoes not only the thermal cycle related to its deposition

but also the thermal cycles of the subsequent layers. Figure 10 illustrates the thermal profile of a Ti alloy single layer processed by Additive Manufacturing. The layer undergoes two liquid/solid transformations and two alpha/beta transformations. This profile depends on numerous variables related to the equipment set up, temperature, and time interval between layers (FRAZIER, 2014).

Figure 10 - Thermal profile illustrating a layer of Ti-6Al-4V during additive processing.
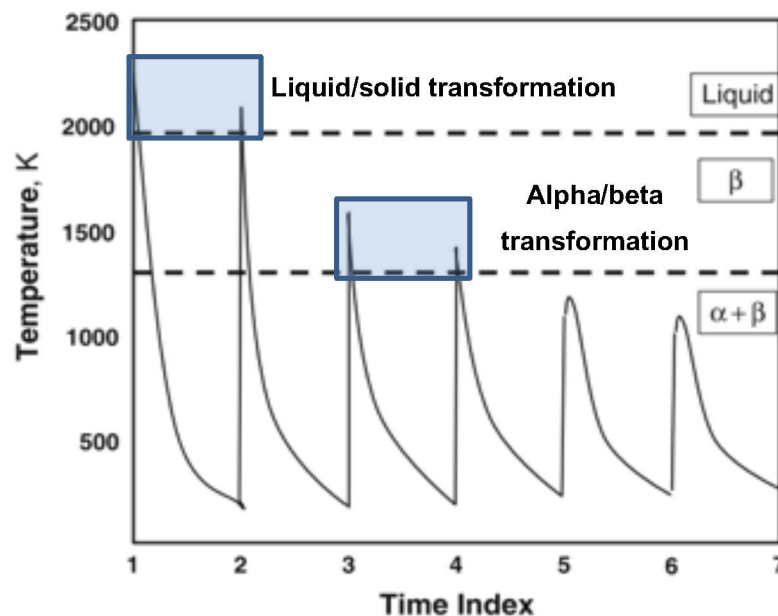
Source: adapted from FRAZIER (2014)

The path taken by the energy source can highly influence the final microstructure. Therefore, different strategies are studied in literature, referred to as scanning strategy in LPBF process and as deposition strategy in DED processing. The deposition or scanning path influences the temperature gradient imposed on the volume being processed and therefore the residual stresses and the microstructure of the component. Figure 11 shows different strategies both for DED and LPBF. In powder bed processes, the inertia for moving the laser beam is lower than for plasma arc, allowing to plan differentiated scanning strategies (SAMES *et al.*, 2016). In directed laser deposition of Inconel 625, the unidirectional deposition path has been claimed to offer greater microstructural

homogeneity to all layers because the growth direction of the dendrites is directly related to the processing direction (DINDA; DASGUPTA; MAZUMDER, 2009).

Figure 11 – Different deposition strategies (a) and different laser scanning strategies (b).
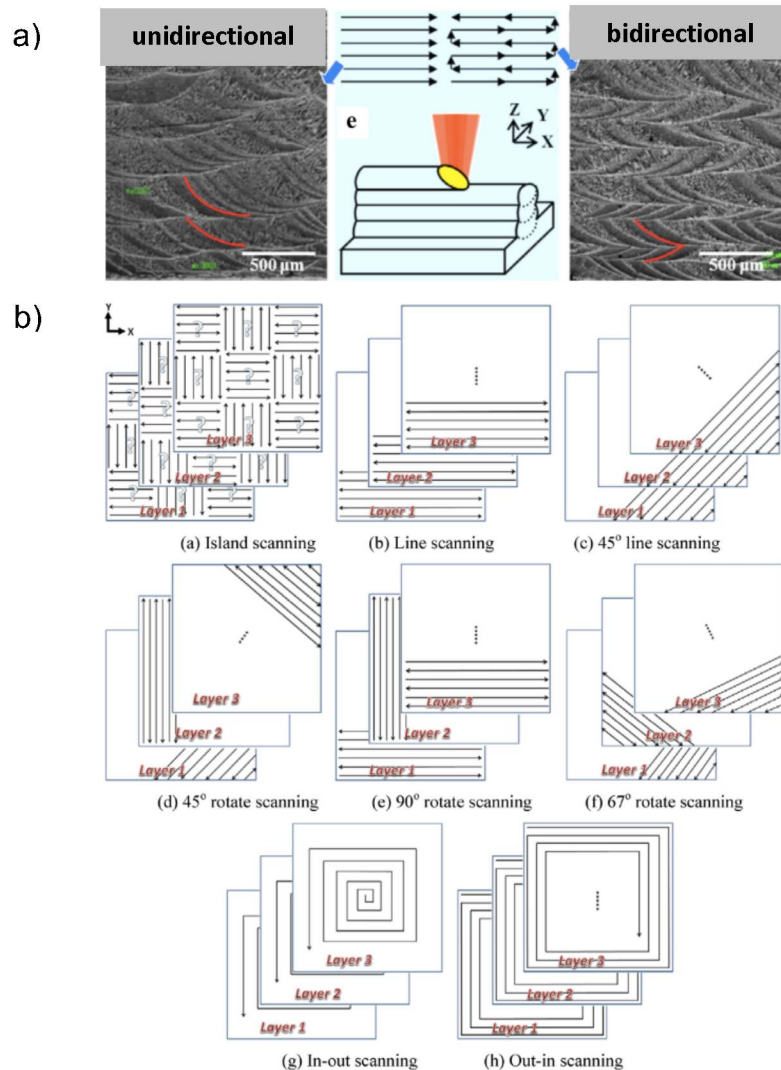
Sources: CHENG; SHRESTHA; CHOU (2016), DINDA; DASGUPTA; MAZUMDER (2009)

The quality of the feedstock material is an important feature . The quality of the powder is determined by its size, shape, surface morphology, composition, and internal porosity. The quality of the powder also determines variables such as flowability and final bulk density. The flowability refers to how well the powder can flow through the feeding system of the AM machine and can impact

considerably the processability. Figure 12 show the impact of different powder qualities on the final part processed by Laser Directed Deposition.

Figure 12 - impact of using different powder qualities on the final part processed by Laser Direct Deposition.
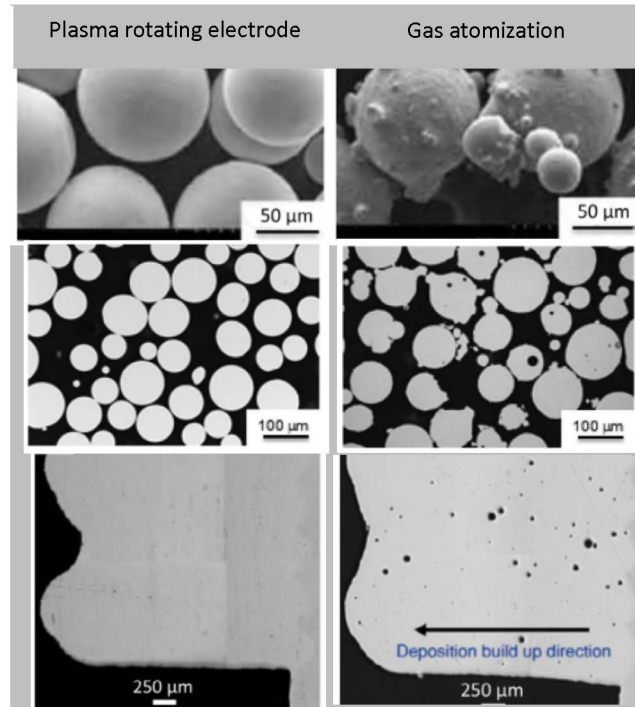
Source: QI; AZER; RITTER (2009), SAMES et al. (2016a)

The interactions between the heat source and the feeding material on the melt pool influences energy consumption. In laser processes it has been reported to occur a loss of energy due to the reflection of the laser beam on the material surface, which must be compensated (SAMES et al., 2016). In the PTA process, the particle size of powders to be deposited influences coating features because the temperature particles reach as they cross the plasma arc and arrive at melt pool determine whether the solidification structure will be more or less refined (BOND; D'OLIVEIRA, 2012).

To build thin walls, the parameters must be properly designed to avoid deviations in the vertical axis. It is important to guarantee the integrity of the lower layers so that the building can evolve properly. Depending on the final objective, it may be necessary to machine the component to remove the discontinuities

typical of each processing technique. As highlighted by SOLA and NOURI (2019), post-processing treatments are against the philosophy of AM techniques, that partly earn their reputation as net-shape manufacturing methods. However, usually post processing thermo-mechanical treatment, heat treatment and surface finishing are required. The first can result in stress relieve and close pores, whereas the last contribute removing the layering effect, satellites and oxides, Figure 13.

Figure 13 - Illustration of the layering effect, satellites and surface oxides usually present on as processed AM parts.
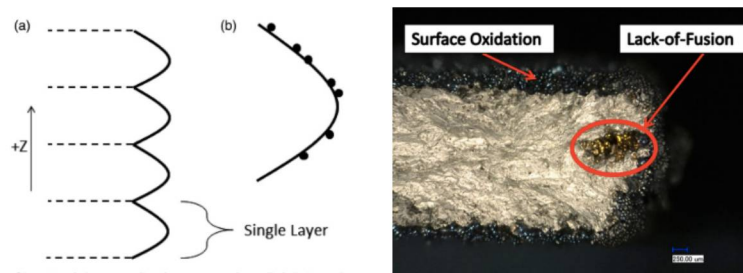
SOURCE: SAMES et al. (2016a)

For deposition-based processes, it is important to consider the effective thickness, illustrated in Figure 14, which is the largest thickness possible to achieve after machining the wall. Knowing the effective height and the effective width allows to plan a suitable deposition strategy, step increments, and layer width (MARTINA et al., 2012).

Figure 14 – Total width and effective thickness of a thin wall processed by Additive Manufacturing.
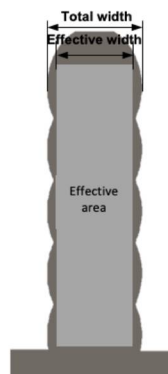
The processing atmosphere also influences the chemical composition of the processed part, processability and heat transfer. The inert atmosphere is used especially when processing reactive materials that might oxidize or absorb moisture when exposed to air (SAMES *et al.*, 2016). At high temperatures, the oxidation of these materials tends to accelerate, and the reduction of oxygen availability becomes mandatory. Niobium, for example, requires a protective atmosphere to be processed (MENEGOTTO, 2015).

Defects such as lack of fusion, cracks, and porosity are frequently found in AM parts. The literature reports two types of pores: metallurgical pores and keyhole pores. Metallurgical pores are usually small (less than 100 um) and can be created at slow scan speeds or high laser power due to gases entrapped in the melting pool. Keyhole pores are usually formed due to instabilities in the melting pool (ABOULKHAIR *et al.*, 2014). Lack of fusion defects can also be generated when the right amount of energy is not delivered for the material to properly melt. Figure 15 illustrates the defects usually seen in LPBF processed parts.

Figure 15 - Common defects seen in LPBF parts.
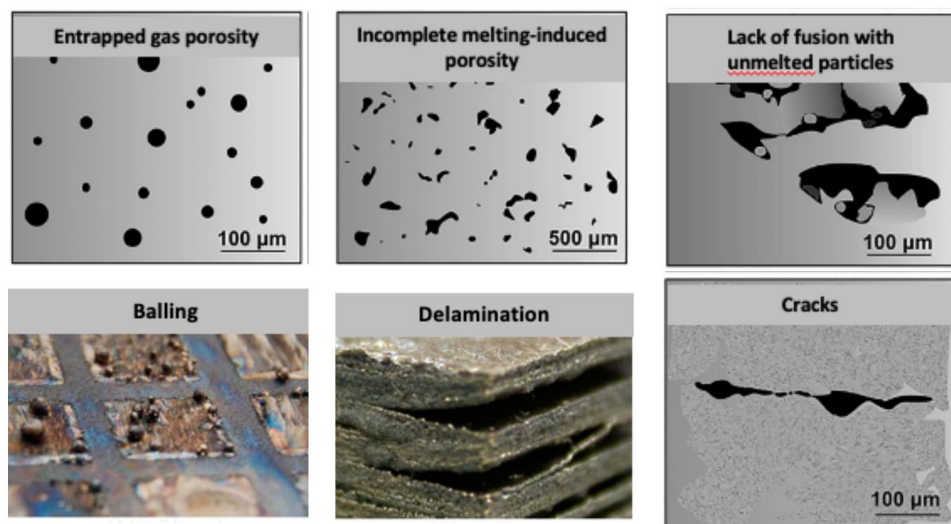
Source: SAMES et al., (2016); SOLA; NOURI, (2019)

Based on this information, this study will explore Niobium and Niobium alloys processed with powder bed fusion and directed energy deposition additive techniques, namely Laser Powder Bed Fusion (LPBF) and Powder Plasma Transferred Arc (PTA-DED). Solidification structures, stability, and oxidation resistance of multilayers processed with these two techniques will be analyzed and discussed. The fabricability of pure Niobium, Niobium-based MMCs, and Niobium-silicide based alloys will be assessed.

3. METHODS AND TECHNIQUES

To investigate the Nb and Nb based alloys processed by AM, two approaches were tested in this research. As a starting point, a more frequently used technique was explored to process Nb powders. The thin layer thickness, multiple thermal cycles and the high energy density of LPBF processing present good tool for the processing of the refractory materials. However, analysis induced the use of PTA-DED to process Nb based powder mixtures.

Processed materials were characterized regarding the impact of processing parameters on the features of pure Nb, particularly using LPBF. After that, the assessment of the solidification sequence of Nb-Si based materials processed *in-situ* by PTA-DED was carried out. Both approaches contribute to the state-of-the-art knowledge on Nb and Nb based alloys processed by AM.

LPBF processing was carried out at the Universiy of Birmingham and PTA-DED at Universidade Federal do Paraná.

3.1. LASER POWDER BED FUSION

3.1.1. Multilayers processed with Nb elemental powder

The study started with a Design of Experiments (DoE) for the processing parameters to build pure niobium samples. The pure Nb powder was provided by Elite Material Solutions. The particles show irregular morphology, as shown in Figure 16(a) and (b), with average particle size of ~33μm, and particle size distribution shown in Figure 16(c). Niobium powder with irregular morphology

have lower cost than atomized powder and have also the potential to guarantee better cost-effectiveness to the process.

The Laser PBF machine used was a commercial Concept M2 Laser Cusing system, Figure 17, located in the School of Metallurgy and Materials at the University of Birmingham. The Concept Laser M2 was fitted with a maximum output of 400 W continuous-wave Nd-YAG laser fibre. The process chamber operated under an argon atmosphere, maintaining oxygen levels <0.1% to prevent oxidation. The recoater speed was adjusted during the initial layers due to the bad flowability of the powder caused by its irregular morphology. Challenges with the flowability of pure niobium were also reported when working with Additive Electron Beam Melting (EBM) (MARTINEZ *et al.*, 2013).

Figure 16 - Scanning Electron Micrograph of the pure Nb powder (a) and (b); and the Powder Particle Size Distribution (c).
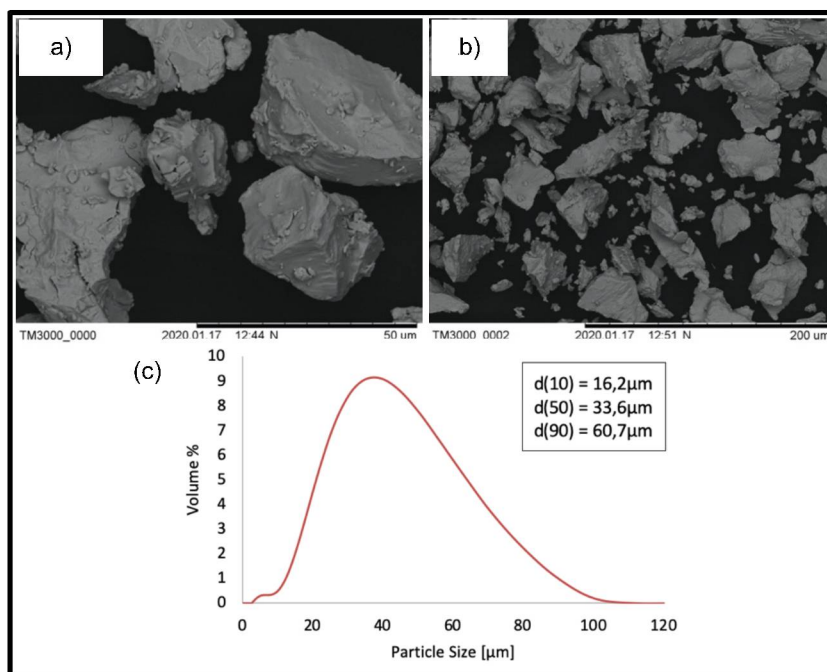
Laser-based processes are known to introduce residual stresses because of the large thermal gradients around the laser spot (ALI; GHADBEIGI; MUMTAZ, 2018; MERCELIS; KRUTH, 2006; YADROITSEV; YADROITSAVA, 2015). To attenuate such effects, the island scan strategy was used. In this strategy, the laser is imposed on different sub-areas (islands) along the layer (illustrated in

Figure 11 (b)). The islands are scanned in short scan vectors. After the selective melting of the islands, laser scans are carried out around the perimeter of the layer to improve the surface finish.

The DOE processing parameters tested are listed in Table 3. These parameters were used to build cubes with dimensions of 5mm x 5mm x 5mm, Figure 18, on a titanium plate with area 90 mm x 90 mm x 120 mm. The energy density for each set of parameters was calculated using the equation (1).

Figure 17 - Concept M2 Laser Cusing LPBF machine.

Equation 1 - Energy density formula.

$$Energy\ density = \frac{Laser\ power}{Laser\ speed\ *\ Hatch\ space\ *\ Layer\ thickness}$$

The samples were cut from the substrate using an electric discharge machine (EDM), mounted, ground, and polished with activated oxide polishing suspension. The microstructure was characterized using HITACHI TM3000 Scanning Electron Microscopy (SEM) and Optical Microscopy (OM). To assess the density, optical micrographs of polished surfaces were used to quantify the fraction of pore-free surface area using the Image J software. The density results reported in this study are an average of four tests.

Vickers hardness profile was assessed using a 100g load applied during 10s on the transverse direction and are reported as the average of three indentations.

Table 3 - Parameters used in LPBF machine to process pure Niobium

Sample ID		Laser Power (W)	Scanning Speed (mm/s)	Hatch Space (mm)	Layer Thickness (μm)
A	1	275	400	0,05	30
	2	275	400	0,11	30
	3	275	600	0,05	30
	4	275	600	0,11	30
	5	275	800	0,05	30
B	1	300	400	0,11	30
	2	300	600	0,05	30
	3	300	600	0,11	30
	4	300	800	0,05	30
	5	300	800	0,11	30
C	1	325	600	0,05	30
	2	325	600	0,11	30
	3	325	800	0,05	30
	4	325	800	0,11	30
	5	325	1000	0,05	30
D	1	350	600	0,05	30
	2	350	600	0,11	30
	3	350	800	0,05	30
	4	350	800	0,11	30
	5	350	1000	0,05	30
E	1	375	600	0,11	30
	2	375	800	0,05	30
	3	375	800	0,11	30
	4	375	1000	0,05	30
	5	375	1000	0,11	30
F	1	275	400	0,05	60
	2	300	600	0,05	60
	3	325	800	0,05	60
	4	350	1000	0,05	60
	5	375	1000	0,05	60

To identify texture developed during processing, XRD analysis (Cu-Kα radiation, λ = 0,154 nm) was performed on the top surface. The interplanar distance was calculated using Bragg`s law, Equation (2), where is the wavelength of the X-Ray, d is the interplanar distance and is the angle between the incident rays and the surface of the crystal.

Equation 2 – Bragg´s law

$$n\lambda = 2dsin\theta$$

Figure 18 - Builds fabricated with Nb powder.
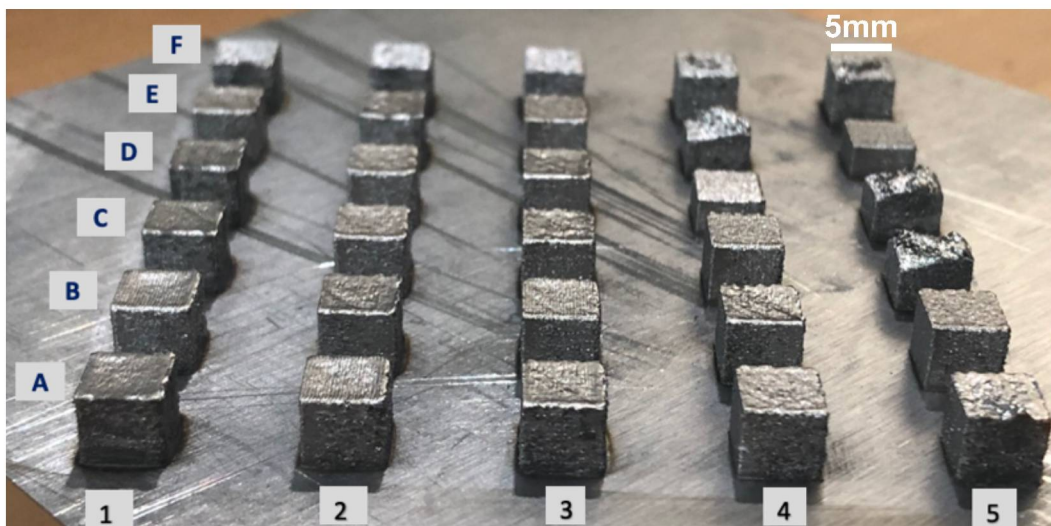
Electron Backscatter Diffraction (EBSD) was performed in the longitudinal and transverse direction of the sample D1, Figure 19, revealing grain boundaries and showing microstructure texture.

Figure 19 – Top surface, or transverse direction (a); surface parallel to the building direction, or longitudinal direction (b).
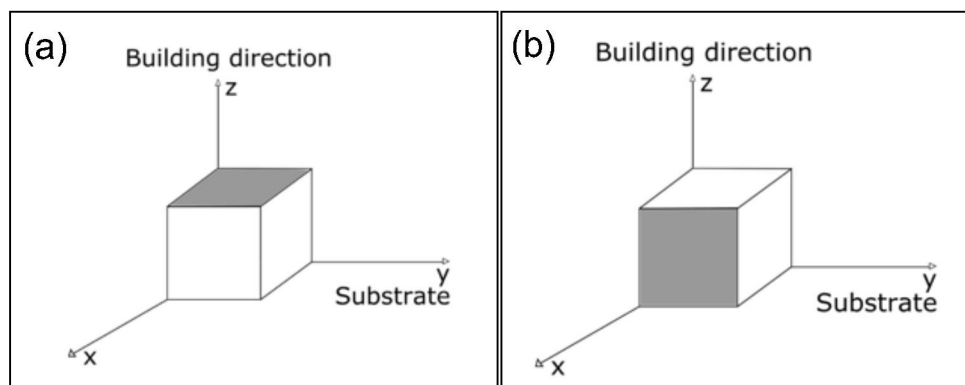
3.1.2. Multilayers processed with the Nb+WC powder mixture

A mixture of pure Niobium powder with 2,5wt%WC, D50 of 0,6um, was also processed. The mixture was performed in rolling bottles for 8h. The final mixture shows a Nb powder that preserved its previous morphology and size when mixed with smaller WC particles, Figure 20(b). The final mixture Nb+WC, Figure 20(a), shows a lower D50 and the particles seem to better adhere to the surface. The adesion of the small carbide particles might be associated to a two fold effect. At the same time that the rough surface of the Nb grains can trap smaller particles, the electrostatic charging contribute to the powder adhesion due to the triboelectrification of powders generated by contact and friction of these two surfaces (ASM HANDBOOK COMMITTEE, 1998; PEART, 2001). The parameters used to build the MMC cubes were the same previously described to pure Nb in Table 3, except for the high layer thickness (group F). A total of twenty-five cubes were processed with the Nb+WC powder mixture, Figure 21.

Figure 20 – SEM of Nb+WC (a) and the Particle Size Distribution of the Nb+WC (b) powder mixture.
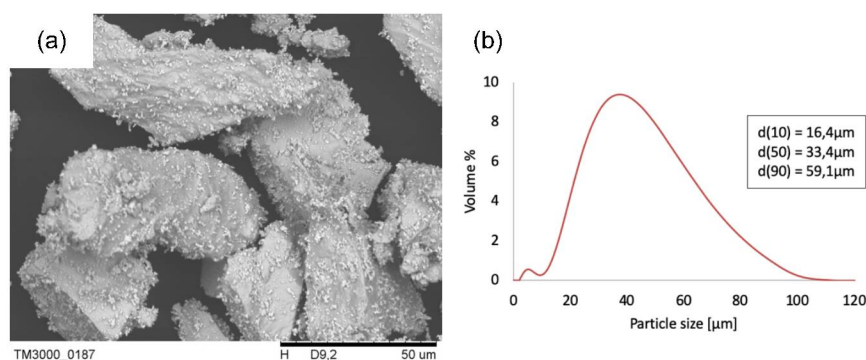
The cubes were cut out from the substrate using Electrical Discharge Machining (EDM) and were characterized following the same steps previously reported to Nb samples.

3.1.3. Multilayers processed with Nb+WC and NbSiAl powder mixture

To assess Niobium-silicide based alloys by LPBF, the mixture Nb47Si20Al (at%) was processed aiming to obtain the alloy by *in-situ* synthesis. Three runs of Design of Experiments (DoE) were required to achieve parameters that resulted in cubes with fewer defects detected with visual analisys. The parameters in Table 4 provided the best cubes, shown in Figure 21. Figure 22 show the samples processed with the Nb47Si20Al powder mixture. The parameters related to all DoE runs can be found in the appendix section, Table 15 and Table 16 in the Appendix I. Sample preparation and characterization were also performed as previously mentioned.

Table 4 - Parameters used in LPBF machine to process Nb-Si-Al alloy

Sample ID		Laser Power [W]	Scanning Speed [mm/s]	Hatch Space [mm]	Layer Thickness [μm]
A	1	200	2000	0,09	30
	2	225	2250	0,05	30
	3	200	2000	0,05	30
	4	200	2000	0,05	30
	5	200	2000	0,05	30
B	1	200	1900	0,05	30
	2	200	2200	0,05	30
	3	200	2100	0,05	30
	4	200	2200	0,05	30
	5	200	2250	0,09	30
C	1	210	1900	0,05	30
	2	210	2200	0,05	30
	3	210	2100	0,05	30
	4	210	2200	0,05	30
	5	210	2250	0,05	30
D	1	220	1900	0,05	30
	2	220	2200	0,05	30
	3	220	2100	0,05	30
	4	220	2200	0,05	30
	5	220	2250	0,09	30
E	1	230	1900	0,05	30
	2	230	2200	0,05	30
	3	230	2100	0,05	30
	4	230	2200	0,05	30
	5	230	2250	0,05	30

Figure 21 - Cubes processed with powder mixtures of pure Niobium + WC.
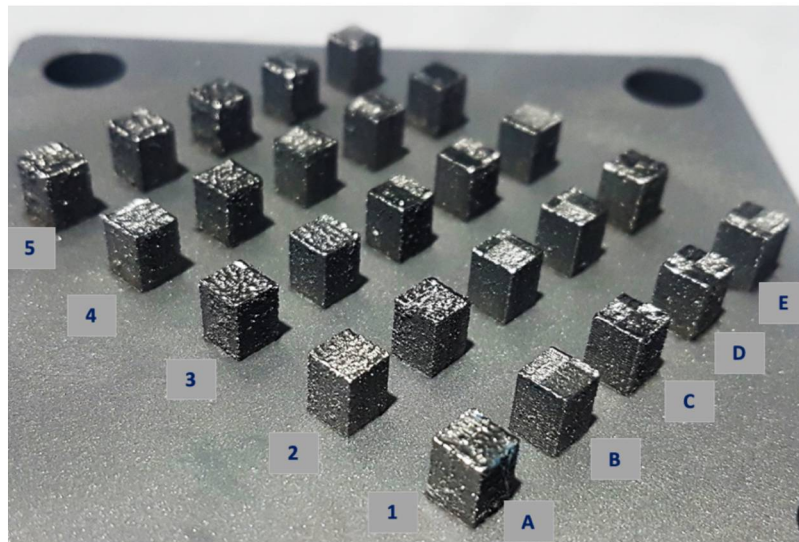
Figure 22 - Cubes processed with the Nb-Si-Al powder mixture.
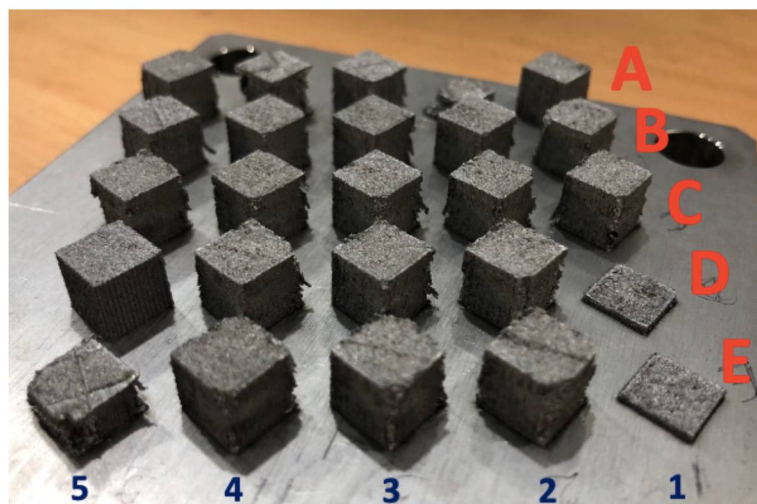
3.2.   POWDER PLASMA TRANSFERRED ARC

Niobium-based alloys were processed at LAMSE - Universidade Federal do Paraná. Nb solid solution and Niobium complex alloys were explored aiming

to investigate the processability of these alloys from elemental powder mixtures and to understand the role of alloying elements on the solidification sequence, crack density and propagation, and oxidation resistance.

Commercially pure niobium, silicon, titanium, aluminum, chromium, molybdenum and zirconium elemental powders, Figure 23, were used to prepare the powder mixtures described on Table 5. The powder mixtures were prepared using rolling bottles during 6h. Before deposition, the mixtures were kept protected against humidity to prevent the influence of ambient humidity on the flowability in the PTA-DED feeding system, Figure 24.

The initial composition tested, Nb24Ti+1Zr, was selected in order to understand the processability using a powder mixture of low complexity and also to assess the *in-situ* synthesis of a Nb solid solution multilayers by PTA-DED. The effect of silicon addition was investigated using Nb47Si11Al (Appendix II) Nb24Ti18Si+1Zr mixtures to obtain the synthesis of the silicides and the Nb solid solution. The synergistic effect of Ti and Al powder additions was studied with the powder mixture Nb24Ti18Si5Al+1Zr. The *in-situ* synthesis of the C14 silicide Laves phase during the solidification was assessed with the powder mixture Nb24Ti18Si5Al5Cr+1Zr. Finally, the Nb24Ti18Si5Al5Cr2Mo+Zr powder mixture was processed to assess the processability of a highly complex powder mixture.

Figure 23 - Elemental powders used to produce the mixtures for PTA-DED process.
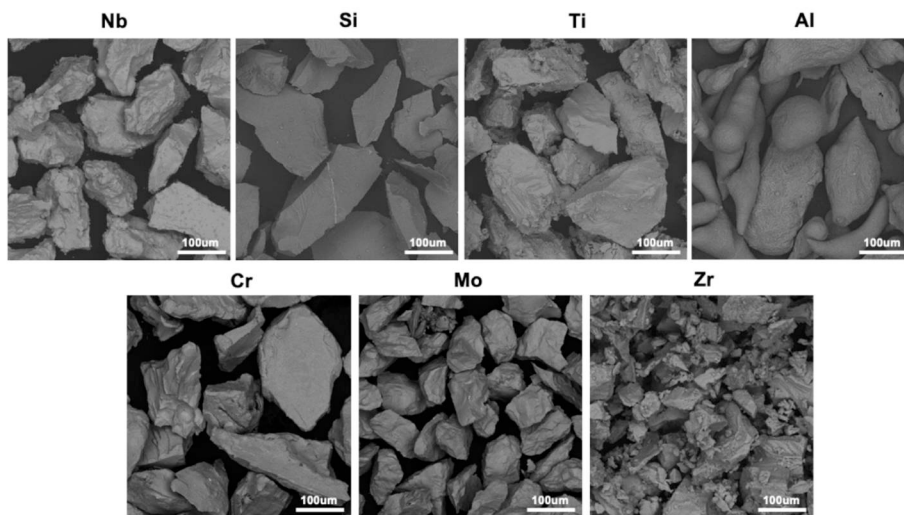
Table 5 - Composition of Nb-based alloys mixtures

Alloy Composition [at%]	Alloy composition [wt%]						
	Nb	Ti	Si	Al	Cr	Mo	Zr
Nb24Ti + 1Zr	73,1	26,9	-	-	-	-	1,7
Nb24Ti18Si + 1Zr	61,3	26,9	11,8	-	-	-	1,5
Nb24Ti18Si5Al + 1Zr	58,1	26,9	11,8	3,2	-	-	1,5
Nb24Ti18Si5Al5Cr + 1Zr	52,0	26,9	11,8	3,2	6,1	-	1,4
Nb24Ti18Si5Al5Cr2Mo + 1Zr	47,6	26,9	11,8	3,2	6,1	4,5	1,4

With the parameters stated on Table 6, 100mm four layers of each composition were deposited, one over the other, on commercially pure niobium substrates with dimension 120 x 12,5 x 12,5 mm.

The process was carried out only with PTA gas protection and also inside an inert chamber (oxygen content below 100ppm) in order to understand the effectiveness of the arc gas shield on mitigating the oxygen solubility into the molten pool. A time interval of 60 s was set between the deposition of each layer.

Figure 24 - PTA Starweld machine.

Table 6 - Processing parameters used in PTA-DED for Nb based alloys.

	Nb-based alloys
Average current	100A
Speed	0,5mm/s
Feeding rate	0,7g/min
Feeding gas flow	0,8l/min
Plasma gas flow	1,8l/min
Shield gas flow	15l/min
Nozzle size	3,2mm
Stand of distance	10mm
Electrode setback	4mm

Samples were cut from the multilayer cross section using the Isomet 4000 Linear Precision Saw, with feed rate of 1,2mm/min and cutting speed of 4000rpm. The multilayers cross-section was ground using silicon carbide paper with mesh ranging from 200-1200. Samples surface finishing was carried out with alumina in sizes 1μm, 0,5μm and 0,03μm. Final polishing was performed with 0,05μm colloidal silica.

X-ray Diffraction scan was performed on the top layer, after grinding and polishing, with a Cu Kα X-ray tube in the Bragg–Brentano configuration, with a scan speed of 1°/min. The microstructure was characterized using Scanning Electron Microscopy (SEM) with Energy Dispersive Spectroscopy (EDS) mapping. Vickers hardness profile was determined using 100g load during 10s on the multilayers cross section. The values presented in this study are an average of ten indentations along the multilayers cross section. Dynamic Thermogravimetry Analysis (TGA) and Differential Scanning Calorimetry (DSC) tests were performed in synthetic air, with temperature scan from 60°C to 1350°C, with a heating rate of 20K/min in air atmosphere.

4. RESULTS AND DISCUSSION

To approach additive processing of Nb and its alloys, the most common AM technique was elected: laser powder bed fusion (LPBF). Metallic Nb, powder mixtures of metallic Nb and tungsten carbide, and elemental powders mixtures of Nb, Si and Al were processed by LPBF. The very thin layers and multiple thermal cycles are a few of the attractive features to process the high melting temperature refractory metal and Nb based MMC. Furthermore, these same features appeared attractive to guarantee the *in-situ* synthesis of Nb silicide-based alloys.

Data showed LPBF is not adequate to process Nb silicide alloys by *in-situ* synthesis, inducing the selection of a DED technique that allow the use of powder mixtures, PTA-DED, to assess additive processing of Nb silicide alloys. This procedure allowed for a better understanding of the impact of alloying elements and of the processing environment on the processability of Nb silicide-based alloys.

4.1. Niobium

Metallic Nb multilayers were successfully fabricated starting from the elemental metal powder using LBPF process. High scanning speeds are reported to compromise melted layers because of the limited time for liquid metal to wet and spread, impairing the flowability of the molten material (TAN *et al.*, 2018). Visual inspection of the as-built coupons, Figure 25, reveals a considerable contribution of higher scanning speeds to the presence of macro defects, confirming predictions from literature. It is important to keep in mind that all processing parameters can impact the presence of macro defects as shown for the laser powder, in Figure 25. However, the adequate selection of the set of processing parameters is required to mitigate the macro defects. This is the case with high scan speeds that have also been reported to provide satisfactory densities when compensated by other parameters. GRIEMSMANN et al. (2021) reported good densification of specimens at speeds as high as 1250mm/s, P =

170W, h = 65um, t = 20um, using spherical Niobium powder and different scanning strategy.

Figure 25 - Set of coupons built with pure Niobium powder. The red arrows show coupons with visual defects.
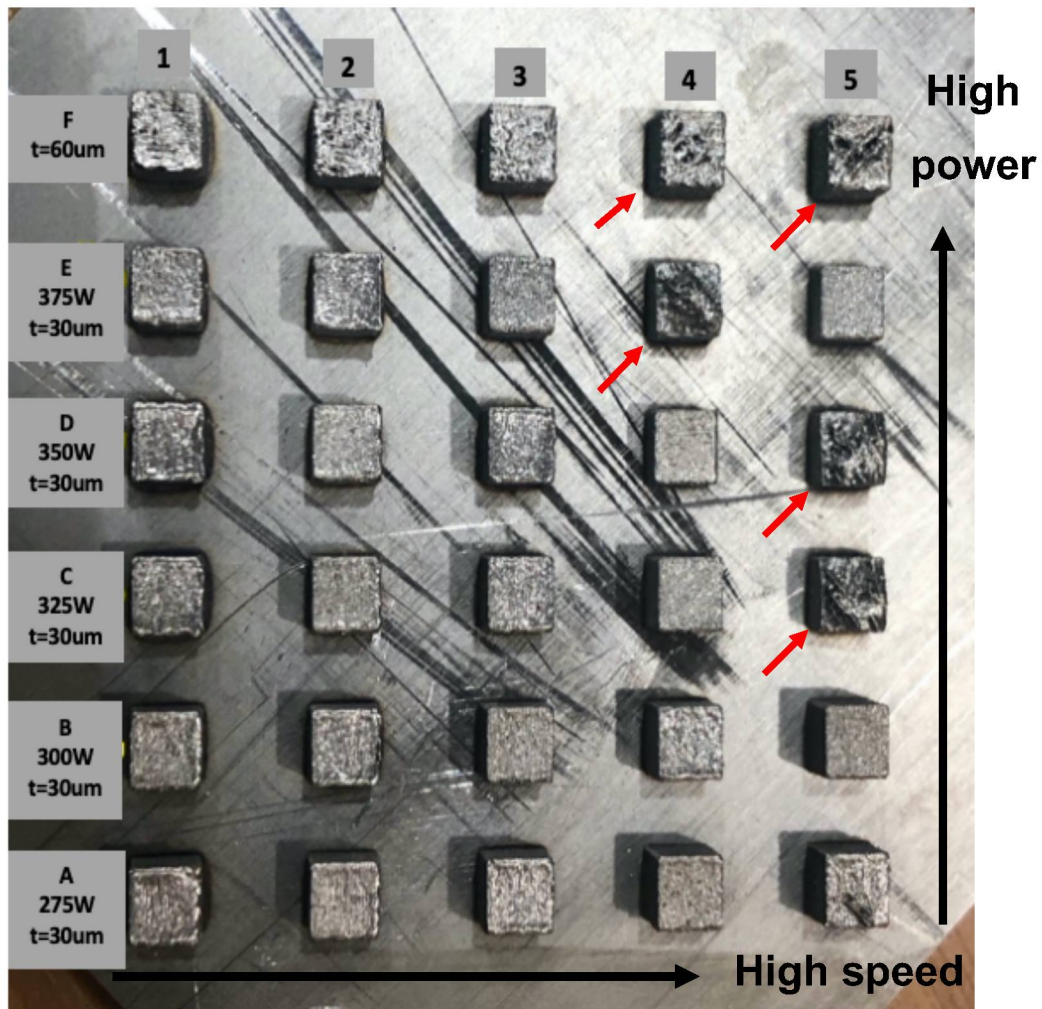
Grain structure analysis at the top surface reveals a blocky grain structure, typical of pure metals, following the island scanning strategy, Figure 26 (a). Grain growth along the building direction follows the heat flow direction accounting for the columnar grains at the transverse cross section, Figure 26 (b). This is expected due to the high temperature gradient of LPBF process and because in pure metals no significant undercooling occurs and columnar grains can grow closely aligned to the normal of the melt pool boundary. The epitaxial grain growth throughout the layers is observed by the long columnar grains at the longitudinal

section. Also, the absence of solidification cracks along the grain boundaries can be related to the low ductile-to-brittle transition temperature (DBTT) of Niobium (~ -200°C) accounting for a relatively good plasticity at room temperature (SAVITSKII; BURKHANOV, 1995). The lower Niobium DBTT is an interesting advantage compared to other refractory metals additive manufactured, such as tungsten, that showed cracks along the grain boundaries when processed by LPBF that authors associated with the high DBTT (TAN *et al.*, 2018).

Figure 26 - SEM and EBSD analysis carried out: (a) on the top surface and (b) on the building direction of the sample D1.
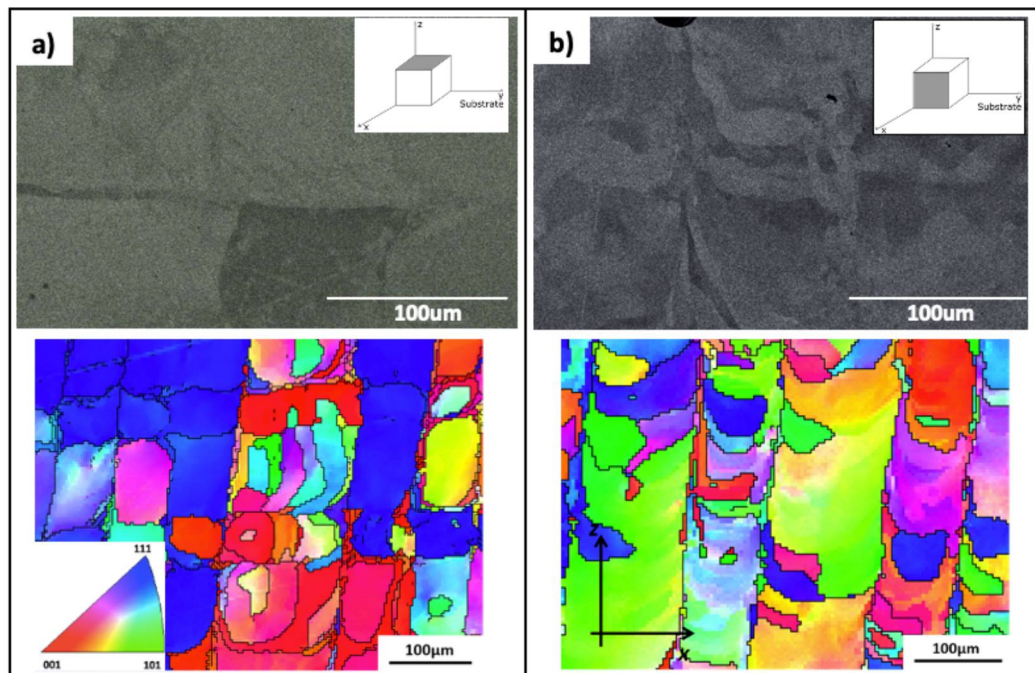
Processing parameters are better correlated with the hardness considering the energy density calculated following Equation 1. Data allows to identify that higher hardness is obtained at intermediate energy densities, Figure 27, where it reaches a plateau and decrease for higher energy densities. This behavior contrasts with the hardness increase with the energy density reported by VANDENBROUCKE; KRUTH (2007) for LPBF of atomized Ti-6Al-4V powder associated to the better densification of the material. Thus, it can be extrapolated that the measured decrease in hardness for higher energy densities might be accounted for by the increase in porosity due to keyhole pores.

It is relevant to point out that the average hardness measured on coupons ($291\pm11HV_{0,1}$) is ~2,3x higher than that reported in literature for cast Niobium billets (CHAUDHARY *et al.*, 2018). The higher hardness values can be partially associated with the fine columnar microstructure formed because of the high cooling rates typical of LPBF. This observation agrees with the study on LPBF/Nb using atomized powder and a lower laser power range that also reported hardness values higher than cold rolled niobium sheets: $149\pm8HV_{0,1}$ and $50HV_{0,1}$ respectively (GRIEMSMANN *et al.*, 2021).
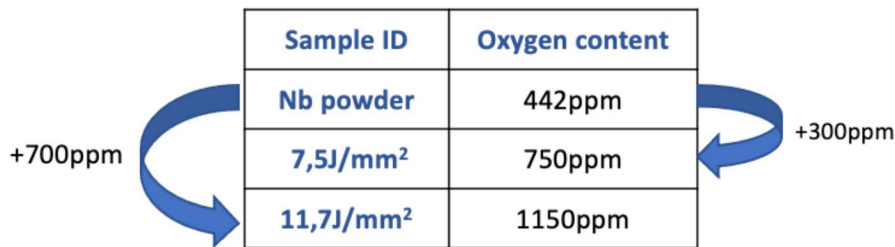
Figure 27 - Relation between hardness and energy density highlighting the different hatch spaces.
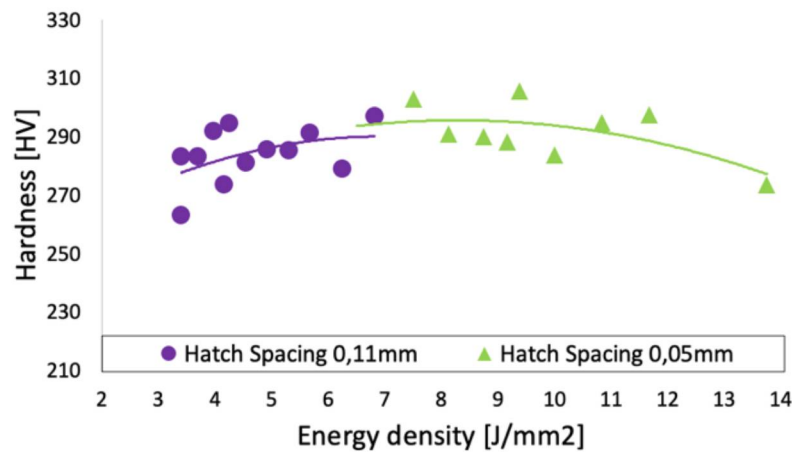
The measured higher hardness of LPBF Niobium has already been associated to the oxygen pick-up in microstructure (SANKAR; BALIGIDAD; GOKHALE, 2013), and further information on the influence of different energy densities on the final microstructure may be accessed by analysing the oxygen pick-up during the processing. Analyses of the oxygen content in the as-received Nb powders and as-processed LPBF coupons, Table 7, reveal that the higher the energy density, the higher is the oxygen pick-up in final microstructure. The increase in oxygen solubility with the energy density agrees with the Nb-O phase diagram shows higher oxygen solubility in Nb for higher temperatures. Furthermore, a hardness increase following oxygen levels was also reported by SERGI et al. (2022) when processing different Nb powder particle sizes by HIP. YANG et al. (2019) relates this phenomenon to the asymmetric lattice distortions

caused by the oxygen compressed in the octahedral interstitial site in BCC Nb crystal lattice. This large shear and dilatational distortions interact with both edge and screw dislocations resulting in a hardening effect.

Table 7 - Effect of different energy densities on oxygen pick-up.

Sample ID	Oxygen content
Nb powder	442ppm
7,5J/mm²	750ppm
11,7J/mm²	1150ppm

+700ppm   +300ppm

The presence of oxygen in solid solution with Nb can also be accounted for by X-ray diffraction analysis. Regardless of the energy density used, results confirm that the processed Nb has a single phase with BCC structure in (110), (200), and (211) planes, Figure 28. Furthermore, the observed peak shift shows a crystal lattice distortion proportional to the energy density. Peaks are shifted towards higher angles when energy density increases.

According to Bragg`s law, Equation 2, if the diffraction angle increases, the interplanar distance decreases, and literature report an increase in the lattice parameter when increasing the oxygen concentration (SANKAR; BALIGIDAD; GOKHALE, 2013). This data disagrees with the present analysis, and the measured displacement as the energy density increases, Figure 28, might be associated with other phenomena, such as crystalline defects and residual stresses (JENKINS; SNYDER, 2012). Furthermore, the impact of alloying elements on the lattice spacing depends on each chemical elements, as claimed by FITZPATRICK et al. (2005) that highlight that lattice spacing changes because of compositional variation. Assessing the impact of Ti and C alloying in Tungsten parts processed by LPBF also showed that alloying elements decrease the interplanar distance (GU et al., 2016b).

Further analysis of the LPBF/Nb coupons correlates the density of builds with energy density, Figure 29. Although it was not possible to observe a trend between energy density and densification of coupons, a densification threshold

occurred at 11,67 J/mm^2. For comparison purposes, a study reported that tungsten-based alloy required 32 J/mm^2 to achieve fully dense parts, which is expected considering the higher melting point (T_{mW} = 3422°C; T_{mNb} = 2468°C), and higher thermal conductivity (λ_W = 173W/mK; λ_{Nb}= 54W/mK) of tungsten (GU *et al.*, 2016).

Figure 28 - Effect on crystal lattice due to different energy densities: high energy density (11,7J/m^2), intermediate energy density (7,5J/m^2), and Nb billet.
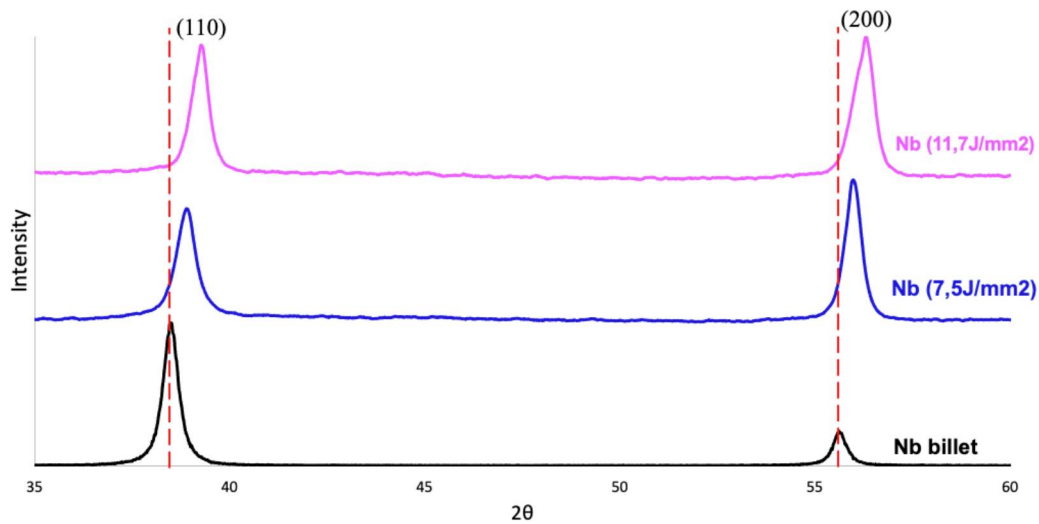
Coupons built with a higher layer thickness, 60μm, are not reported in Figure 29 but the thicker layer builds showed densities lower than 90%. The density of coupons built with 30μm layer thickness exhibit density in the range from 94,3% (P = 300 W, v = 600mm/s, h = 0,05mm) to 99,9% (P = 350 W, v = 600mm/s, h = 0,05mm) (red triangle on Figure 29). However, data shows that for the processing conditions used, the Nb coupons density is independent from energy density.

The build-up rates, represented by the quotient of laser speed, hatch space and thickness, varied from 0,9 to 3,3mm^3/s for the coupons with densities higher than 99%. These build up rates are in a wider range than those reported by GRIEMSMANN et al. (2021) who processed atomized pure Nb by LPBF using lower laser powers and achieved densification higher than 99% for build-up rates

from 0,33 to 1,63 mm³/s and highlighted the need to improve the build-up rates to enhance the overall process efficiency.

Figure 29 – Effect of energy density on the densification of coupons built with pure Nb powder.
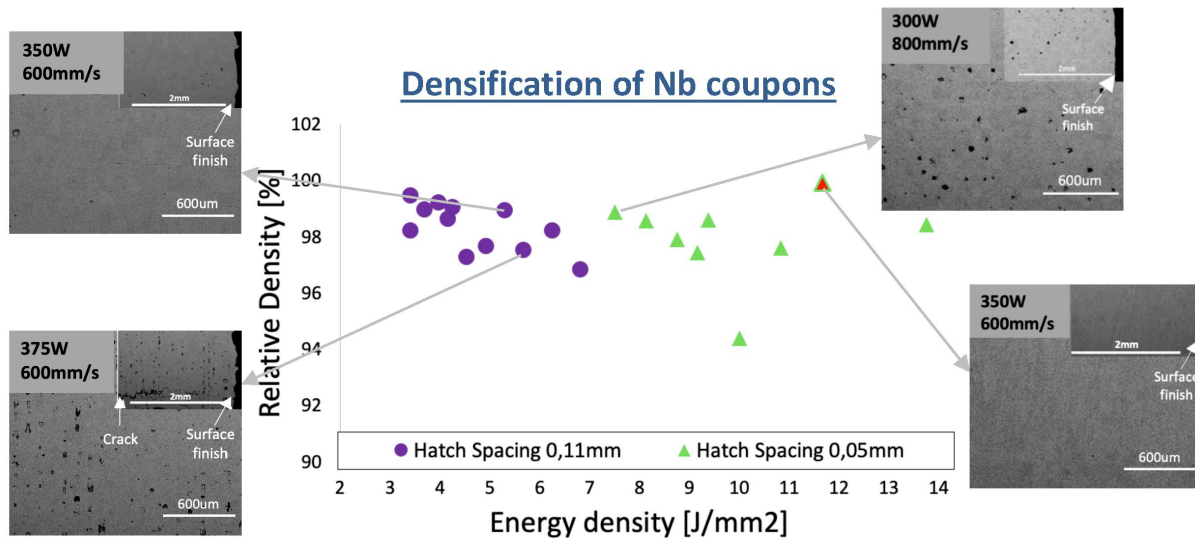
For the larger hatch space tested (macrographs on the left), increasing laser power has a considerable influence on the formation of macrocracks (in detail) due to thermal stresses of multiple cycles and porosities associated with instabilities in melt pool. A high amount of porosity is also observed following a combination of lower laser power and increasing speed (images on the right), accounted for by the lower heat input that was not effective in melting the refractory material. The hatch spacing affects not only the build-up rate but can also influence the interconnection of neighbouring tracks (GUO et al., 2018b). From the insert in macrographs, it is also possible to observe that smaller hatch spaces (green symbols) result in better surface finish (in detail).

Although no specific trend between the cupouns density and energy density was observed for the processing parameters used, like the findings of LI et al. (2016) for LPBF of TiNi alloys, some authors have described a relationship between these parameters (DILIP *et al.*, 2017; MOHAMED *et al.*, 2020; READ *et al.*, 2015). Low energy densities are reported to induce high porosity levels due

to lack of metallurgic consolidation and high energy densities can also result in high porosity levels due to keyhole pores.

In short, despite the laser imposing an extremely high cooling rate, the LPBF proved to successfully fabricate pure Nb parts with densification higher than 99%. However, although processing was carried out in an argon chamber, the oxygen pick-up impacted the final microstructure. High energy led to higher oxygen pick-up, accounting for the increase in hardness.

The success in obtaining Nb parts by LPBF allowed to go further in the understanding of AM for Niobium alloys. To continue this study, the processability of Nb + WC powder mixtures will be assessed as a preliminary study to obtain Nb-MMCs by Additive Manufacturing-LPBF.

4.2. Nb+2,5wt%WC

Further assessment of the processability of Nb based materials used Nb+WC powder mixtures. For the processing conditions used, the impact of WC in the Nb based builds is observed from the initial visual analysis. No apparent macro defects such as delamination and lack of fusion, even at high scanning speeds, are observed (Figure 30) suggesting better processability than pure Niobium powder. This behavior can be accounted for by slightly increases the conductivity of the Nb+WC mixture (k_{Nb}= 54W/mK; k_{WC}= 63W/mK) that might induce a more evenly melt of the powders.

It is interesting to observe that, for both materials, the higher densification was achieved for the set of parameters that offer an energy density 11,7 J/mm^2, Figure 31. Also, Nb+WC builds show less porosity but porous are larger.

The average hardness of Nb+WC coupons is 250±16 $HV_{0,1}$, representing a 15% decrease compared to the 291±11$HV_{0,1}$ of pure Nb coupons. Although the presence of WC in the powder mixture might create an expectation regarding an increase in hardness, that would require a distribution of unmelted WC particles, allowing for second phase hardening. However, melting of the carbides can account for the larger porous in Nb+WC builds because the WC dissociation offers the opportunity of the C to react with the interstitial oxygen retained in the

material, and so reducing the oxygen strengthening measured in pure Nb coupons.

Figure 30 - Set of coupons built with the Nb + WC powder mixture.
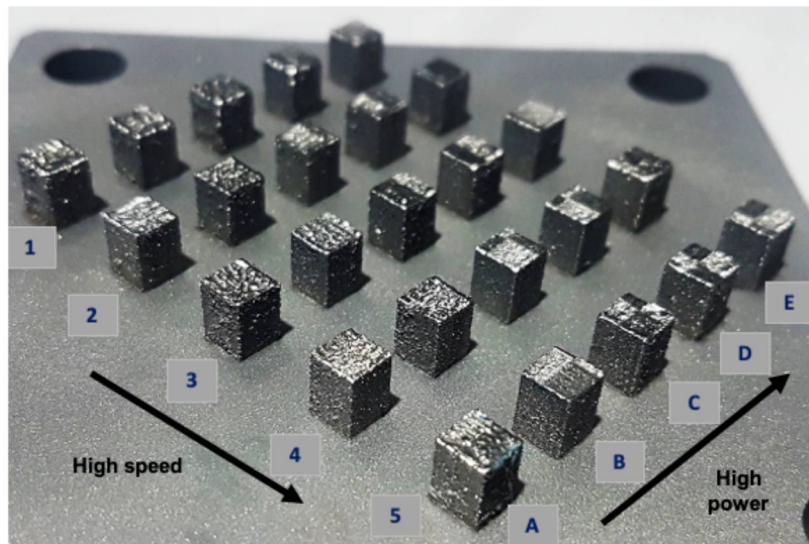
Figure 31 - Densification of coupons related to the energy density.
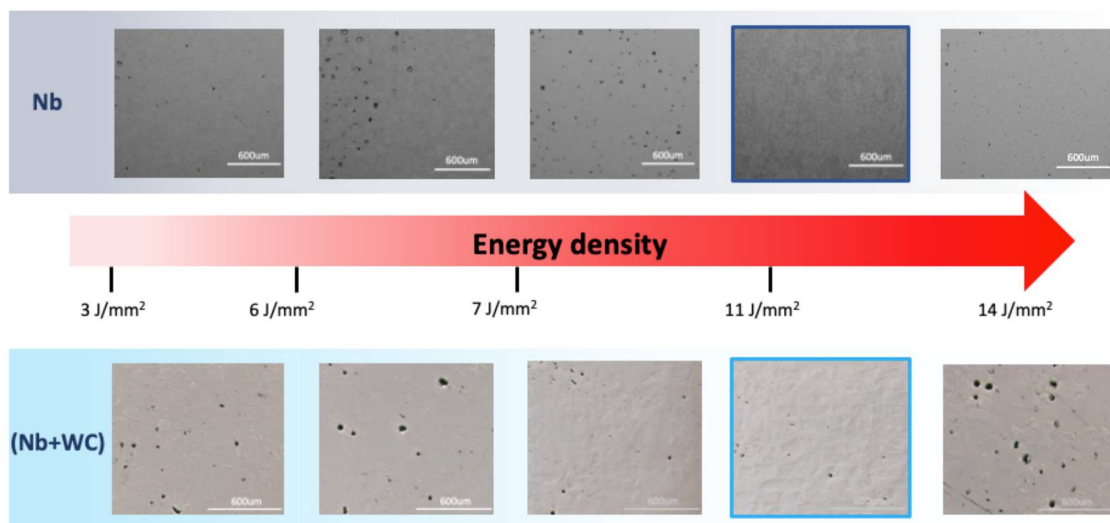
Furthermore, although a hardness increase might also be expected from solid solution strengthening of substitutional tungsten on niobium matrix as reported by CHAUDHARY et al. (2018), this is not as effective as the interstitial solid solution strengthening gained from oxygen retained in the microstructure of pure Nb, as previously mentioned. Unlike pure Nb, the correlation between hardness and the energy density for the Nb+WC coupons, Figure 32, shows that intermediate energy densities result in lower hardness suggesting that the removal of oxygen due to the WC dissolution was more significant, reducing the amount of interstitial oxygen in Nb.

Figure 32 - Relation between hardness and energy density of coupons built with Nb+WC powder mixture.
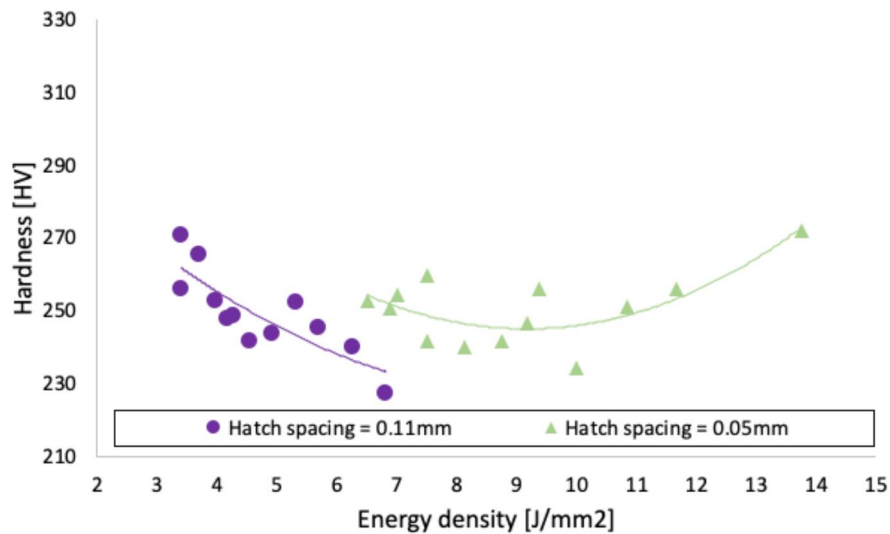
Corrobating the hypothesis that oxygen was removed from solid solution and reacted with C from the dissociated carbides, X-ray diffraction results show a reduction in the distortion of the crystal lattice when processing the Nb+WC mixture, Figure 33.

Further correlation between builds processed with the pure Nb powder and Nb+WC powder mixtures used high temperature exposure of trials in air and argon. Analysis in argon, Figure 34 (a) showed that both materials have very small variation in mass. The measured mass loss for the Nb+WC build can be associated with further release of CO_2 trapped in samples. The small increase for pure Nb builds might be related with the purity of the argon gas used. Further

differences were measured for tests carried out in air. The less significant mass gain of Nb+WC builds further confirm that a lower interstitial oxygen content is present in this material accounting for the lower oxidation rate Figure 34 (b).

Figure 33 - Effect of WC on crystal lattice comparing the XRD of coupons built with pure Nb, Nb+WC powder mixture and Nb billet.
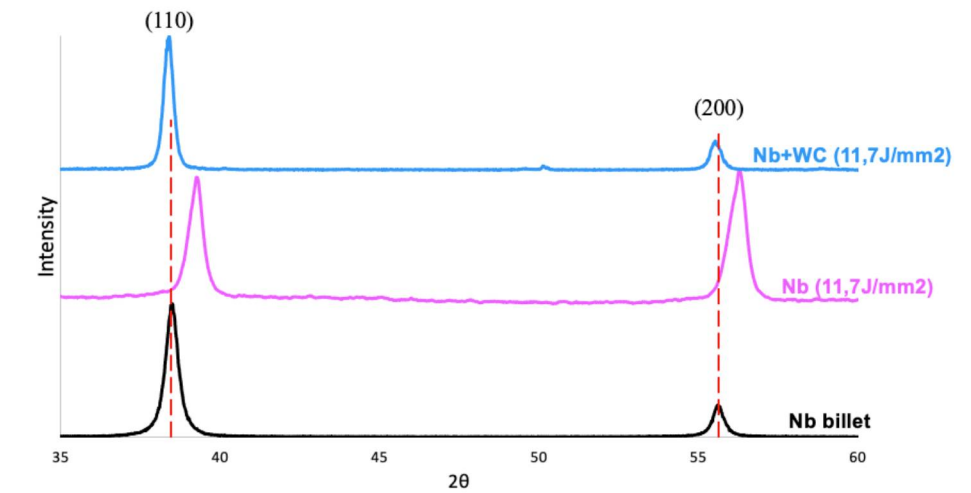
Figure 34 - Thermogravimetric analysis (TGA) of coupons exposed to 1350°C in argon (a) and air (b).
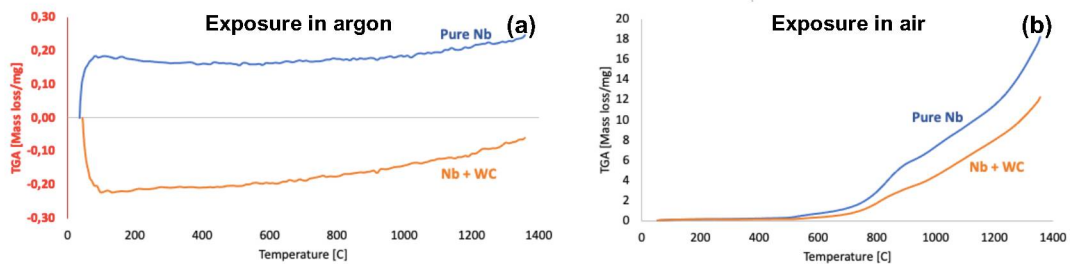
In short, *in-situ* Nb+WC multilayers were also successfully processed by LPBF starting from a powder mixture. However, larger porosity in builds processed with Nb+WC powder mixture is a consequence of the trapped CO_2 gas formed due to carbide dissociation. The hardness of the final builds decreased with the addition of WC, a consequence of the less significant strengthening of substitutional tungsten as opposed to interstitial oxygen in solid

solution. The addition WC also reduces oxygen trapped in builds and, consequently, slows down the oxidation rate of the material.

The success in process Nb+WC multilayers *in-situ* starting from a powder mixture opens the possibility to explore powder mixtures with higher complexity, such as the Nb silicide-based alloys.

So, taking a step further on the processing of Nb based alloys, powder mixtures of Nb-Si-Al were processed by LPBF to assess the processability of the alloy. The approach of obtaining Nb silicides by *in-situ* synthesis aim at mitigating the fabricability challenges caused by the low toughness of these compounds.

4.3. Nb47Si20Al

Processing Nb47Si20Al elemental powder mixtures with LPBF provided challenges associated with the *in-situ* synthesis of compounds together with the already mentioned irregular morphology of powders. Final DoE used to process cube samples, Figure 35, is presented in Table 4. Compared to pure Nb, Niobium-silicide-based cubes show poor surface finishing, with accentuated roughness. It suggests that the melting of the powder mixture may have been compromised.

Figure 35 - Cubes fabricated with the Nb47Si10Al powder mixture.
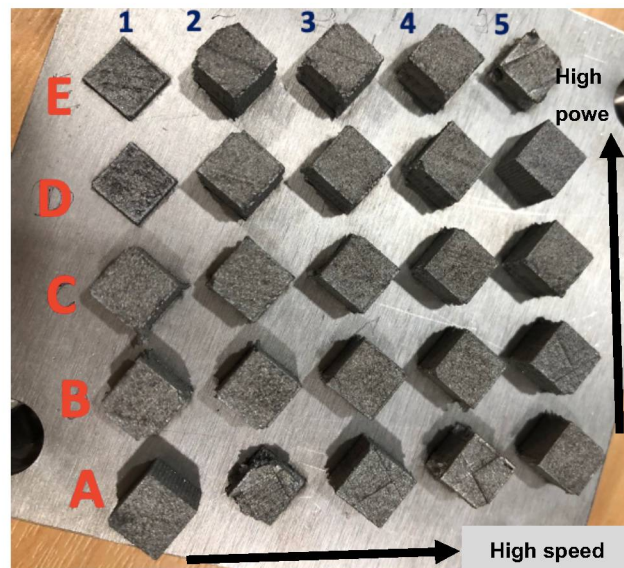
Pores and unmelted particles, Figure 36 (a), are present in the build suggesting that a higher energy density would be required to properly homogenize the microstructure. Cracks are also present, Figure 36 (b), a consequence of low toughness of Nb silicides that cannot accommodate the stresses due to the fast solidification.

The high hardness of builds, 647± 309 HV, suggest that the synthesis of silicide compounds occurs but the large dispersion is accounted for by the heterogeneity of builds. The elements distributed heterogeneously over the melting pool, spreading in swirl-like patterns potentially caused by convection inside the melt pool, Figure 36 (b).

Figure 36 - Microstructures of the cubes fabricated with the Nb47Si10Al powder mixture.
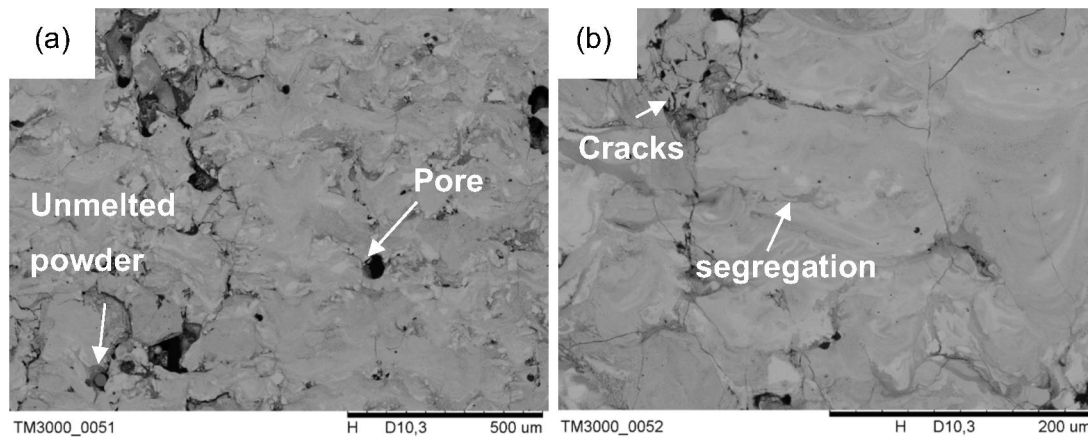
Results allow to raise the hypothesis that the synthesis of silicides require a large energy input and also that to achieve a homogeneous microstructure a pre-alloyed Nb47Si20Al spherical powder might be required. However, literature shows that, even using pre-alloyed spherical powders and higher energy densities, the synthesis of a Nb-based alloy by LPBF is still a challenge. (GUO et al., 2018a) reported similar behavior processing single layers with pre-alloyed powders of Nb37Ti13Cr2Al1Si by LPBF, using higher energy densities (v=200mm/s, P= 380W, t=80um, h=0,05mm).

Furthermore, inspite of the larger number of heating cycles that remelt and reheated previous layers, the fast-scanning speeds of LPBF processing

67

contribute to the observed incomplete synthesis of silicide compounds. This might be achieved by a Direct Energy Deposition technique, that gives a better control thermal gradient.

Considering these results, in particular the impact of fast solidification rates, PTA-DED appears as an advantageous technique for processing these materials. Multilayers of Nb-Si binary alloys have already been assessed by PTA to evaluate *in-situ* synthesis of silicides, which was successfully achieved. Besides given a good control of solidification rates, this technique allows manipulating the composition of the alloy layer by layer.

To assess the hypothesis that lower thermal gradient allow for the successful processing Nb silicides, PTA-DED was selected. The investigation of processing parameters was carried out in previous study (CARDOZO; D'OLIVEIRA, 2022). In preliminary studies, the processability and oxidation resistance of the Nb47Si20Al alloy by PTA-DED was successful using *in-situ* synthesis of the alloy during the elemental powder mixture multilayer deposition. Results are shown in Appendix II.

However, Nb based alloys are usually multi-alloyed to simultaneous act on enhancing toughness, oxidation resistant and other specific demands. Hence, the solidification process is very complex due to the interaction among many elements. The selected approach in this study, starts from a powder mixture with low complexity (NbTiZr), that results in a solid solution alloy.

The investigation evolves to more complex powder mixtures to understand how the powder mixture complexity interferes in the *in-situ* synthesis of the alloys. The increasing complexity of the powder mixture also allows to understand the synergistic effects of elements on the solidification sequence and on the oxidation resistance. The metallurgical stability was also assessed by the effect of the multiple thermal cycles on the microstructure.

4.4. Nb24Ti+1Zr

The onset of multilayers processed by PTA-DED used powder mixture to obtain multilayers of a NbTiZr solid solution alloy. The macro analysis, Figure 37, reveals that the solid solution multilayer has a marked transition between layers,

where Nb rich particles concentrate, as shown by EDS composition mapping on Figure 37 (a), and confirmed by the phase composition analysis assessed by EDS, Table 8. Further analysis of these particles reveals them to be constitute of Nb, most probably Nb droplets trapped in a thin oxide case during deposition. The formation of these Nb oxide encased particles is associated with the high affinity of Nb with oxygen at high temperatures. Although the melt pool was protected with argon, the industrial purity of the argon gas used might allow for oxygen to react with Nb, impairing the final microstructure.

Figure 37 - Microstructure at the cross section of the NbTiZr multilayer and the EDS composition map of the particles segregated between layers (a).
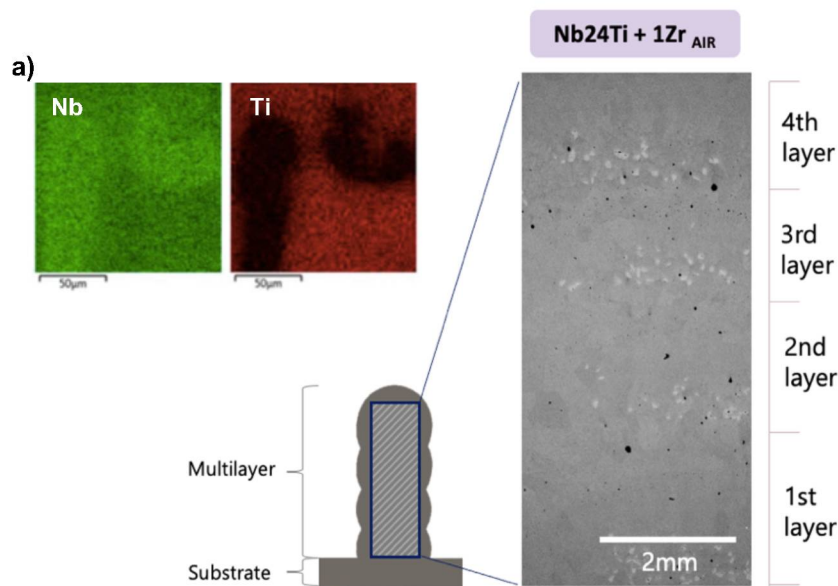
Table 8 - Average composition of phases observed in the multilayer NbTiZr.

Alloy	Phase	Composition (at%)	
		Nb	Ti
Nb24Ti + 1Zr	Nb_{ss}	60,7	38,6
	$Nb_{particles}$	99,4	0,2

The mechanisms by which the Nb particles concentrate between layers is summarised in Figure 38. As powders are feed and cross the Plasma Arc, Figure 38 (a), the occasional interaction between Nb particles and oxygen from air outside the shielded region, or from impurities in argon gas used in the PTA-DED system, allows for an oxide film to form and entrap semi molten or molten Nb particles, Figure 38 (b). When these particles reach the melt pool, the oxide case acts as a barrier that does not allow mixing with the molten material. The melt pool convection dynamic results in the accumulation of these particles at the bottom of the melt pool, Figure 38 (c), creating the marked transition between layers.

Figure 38 - Schematic of the interaction between niobium particles and oxygen.
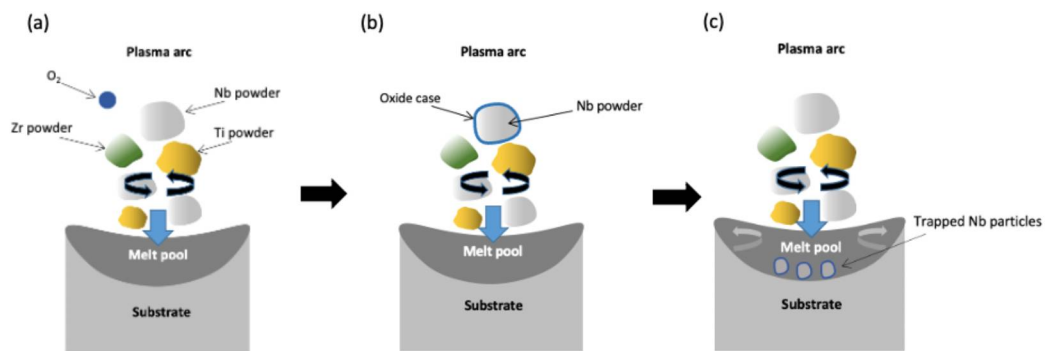
ADAPTED FROM: ABREU; BUENO; D'OLIVEIRA (2022).

Niobium and Titanium have almost full solubility in each other, so that the expected result of the *in-situ* synthesis is a solid solution of Nb containing Ti and Zr. X-ray diffraction at the top layer, which was not exposed to remelting, is shown in Figure 39 and confirms the presence of a single solid solution $Nb(Ti,Zr)_{ss}$ in multilayers processed with the powder mixture NbTiZr.

Figure 39 - XRD at the top of the NbTiZr multilayer.
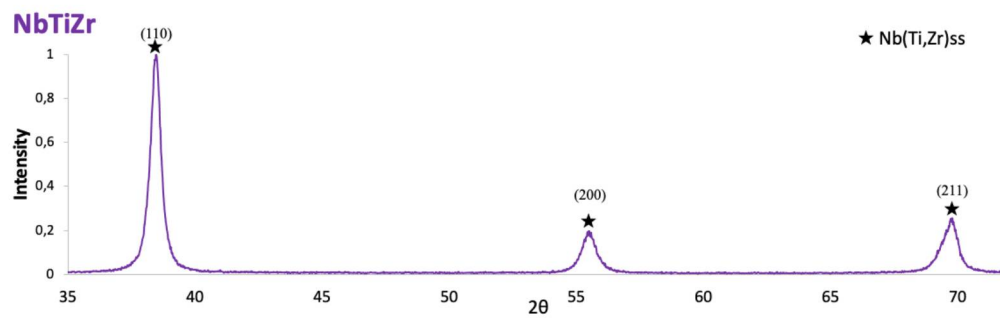
A better understanding of the processed multilayer can be achieved by analysing the solidification sequence. The transformations occurring during the solidification of each deposited layer depend mainly on the composition of the powder mixtures, processing parameters and thermal history. The hypothesis for the solidification occurring during the deposition of the NbTiZr powder mixture is put forward on Figure 40 based on observations made at the top layer of coatings, that did not suffer further thermal cycles. It is of relevance to point out that the interaction between powders can start in the plasma arc as droplets of each element come together.

Figure 40 - Processing sequence and phase transformation occurring during processing of the NbTiZr powder mixture.
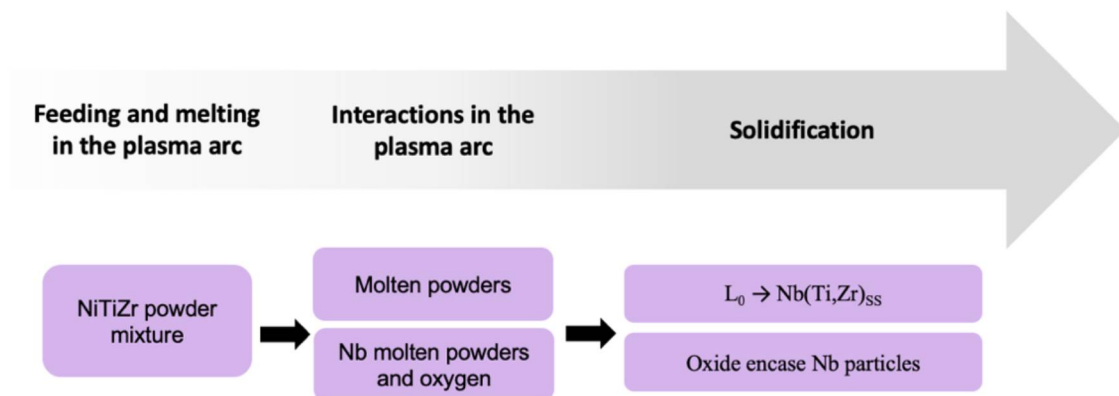
In this section, a Nb_{ss} multilayer was analyzed. The Nb_{ss} is the key phase for improving the fracture toughness of the next generation ultra-high temperature alloys (TSAKIROPOULOS, Panos, 2018). However, when in high-volume

fraction, it can compromise the oxidation resistance to meet the property goals for those next generation alloys.

The addition of Si to the alloy can improve the oxidation resistance and mechanical properties at high temperatures. However, manufacturing the hard Nb-Si based alloys by conventional processes is challenging, as previously mentioned, and the *in-situ* synthesis of Nb-Si based alloys by PTA-DED can open new opportunities to enable the large-scale application of these materials.

4.5. Nb24Ti18Si+1Zr

The addition of Si to the powder mixture resulted on deposits exhibiting an increase of 120% in hardness (864 $\pm$ 54 HV), which was expected due to the formation of niobium silicides. Typically, the addition of Si results in formation of Nb-silicides due to the low solubility of Si in Nb_{ss}.

Furthermore, macroanalysis reveal that the addition of Si in the powder mixture eliminated the segregation of Nb particles between layers, Figure 41. Silicon is more reactive with Nb than oxygen, and reacts with Nb firstly when the NbTiSiZr powder mixture melts in the plasma arc, eliminating the event of Nb droplets interaction with oxygen. The synthesis of Nb silicides is confirmed by XRD analysis, Figure 42.

The addition of Si can also improve the oxidation resistance of the multilayer. Nbss have high solubility of oxygen at high temperatures and, because of it, the reduction in Nbss volume fraction in microstructure can considerably increase the oxidation resistance of Nb alloys (ZELENITSAS, 2005). Mass change analysis up to 1350°C, Figure 43, confirms that the presence of Si in Nb based multilayers increases the oxidation resistance, postponing significant mass gain for temperatures higher than 700°C.

Previous study report that Nb_{ss} starts to oxidize with the formation of αNb_2O_5 at temperatures higher than 250°C (LEONT'EV *et al.*, 2016). Above 800°C, the αNb_2O_5 transforms into βNb_2O_5 and form a compound with Ti. The oxidation of silicides starts near to 990°C and is less intense than the oxidation of Nb_{ss} due to the lower oxygen diffusion in silicides.

Figure 41 - Microstructure at the cross section of the NbTiZr and NbTiSiZr multilayers.
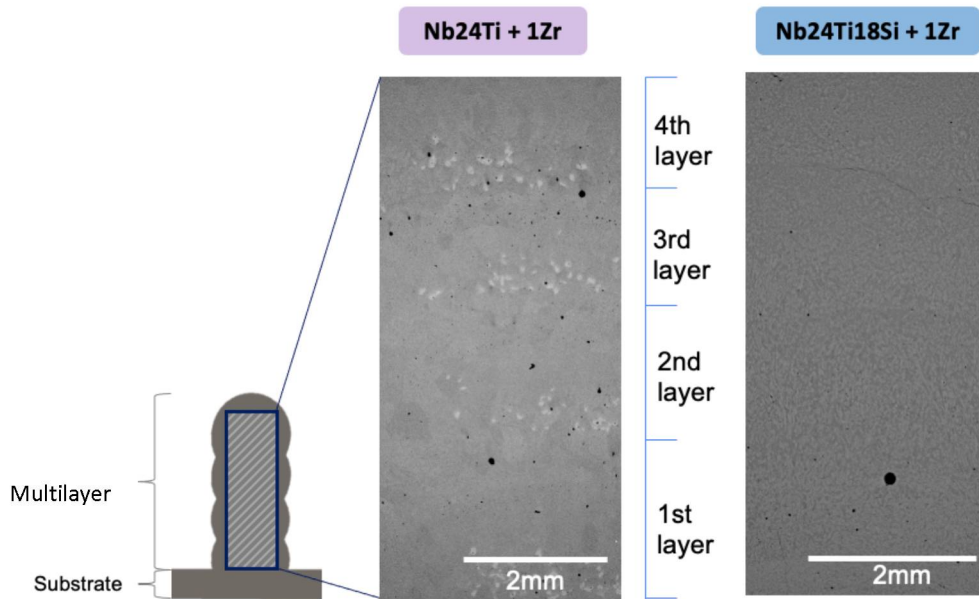
Figure 42 - XRD of the top of the NbTiSiZr multilayer.
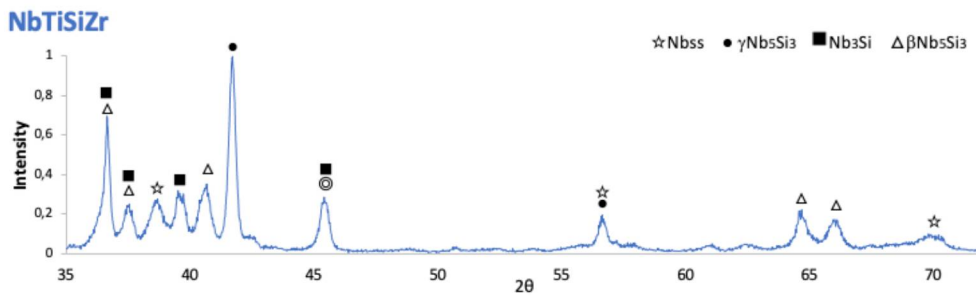
The primary Nb_5Si_3 phase is also known to provide creep and oxidation resistance at high temperatures (YUAN *et al.*, 2014). However, literature highlights that the ideal balance between size, morphology, and volume of the intermetallic phase, together with the formation of a network of a tough matrix, can play an important role in optimizing the mechanical properties of Nb-silicide based alloys (WANG, Fuxin *et al.*, 2018; YUAN *et al.*, 2014). Hence, it is important to have enough process control so that the microstructure features, such as silicides size, their composition and morphology, can be predicted.

Figure 43 – Impact of Si addition in oxidation resistance of NbTiSiZr multilayer.
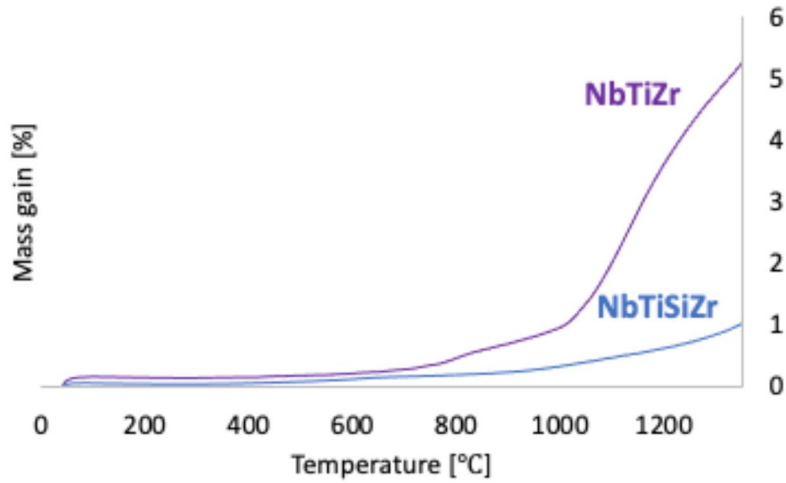
The *in-situ* synthesis of these alloys by PTA-DED using powder mixtures as feedstock might offer flexibility in controlling these features. A study regarding the as-deposited solidification structure and the effect of multiple thermal cycles on microstructure evolution can start to pave the way for a wide application of PTA-DED using *in-situ* synthesis for the fabrication of Nb-silicide based components.

Understanding the as-processed microstructure and solidification paths will allow to gain a better knowledge on the interaction between elements in the powder mixture and on the *in-situ* synthesis occurring for each alloy composition. Furthermore, it is the base to assess the effect of the multiple thermal cycles along the multilayer.

In this study, the top layer is the reference for the as deposited condition since it was not exposed to thermal cycles. It better reveals primary segregations, phase distribution and phase morphology. Hence, revealing the as deposited microstructure, the top layer is analyzed to explain the solidification paths for each composition.

For the Nb24Ti18Si+1Zr powder mixture, the as-deposited microstructure mainly consists of Nb_{ss}, the βNb_5Si_3 silicide, the Nb_3Si silicide, and the $Nb_{ss}/\gamma Nb_5Si_3$ eutectic, Figure 44. The phase composition was assessed by EDS, Table 9.

Figure 44 - Micrography of the top layer (a) general view and (b) details of the microstructure.
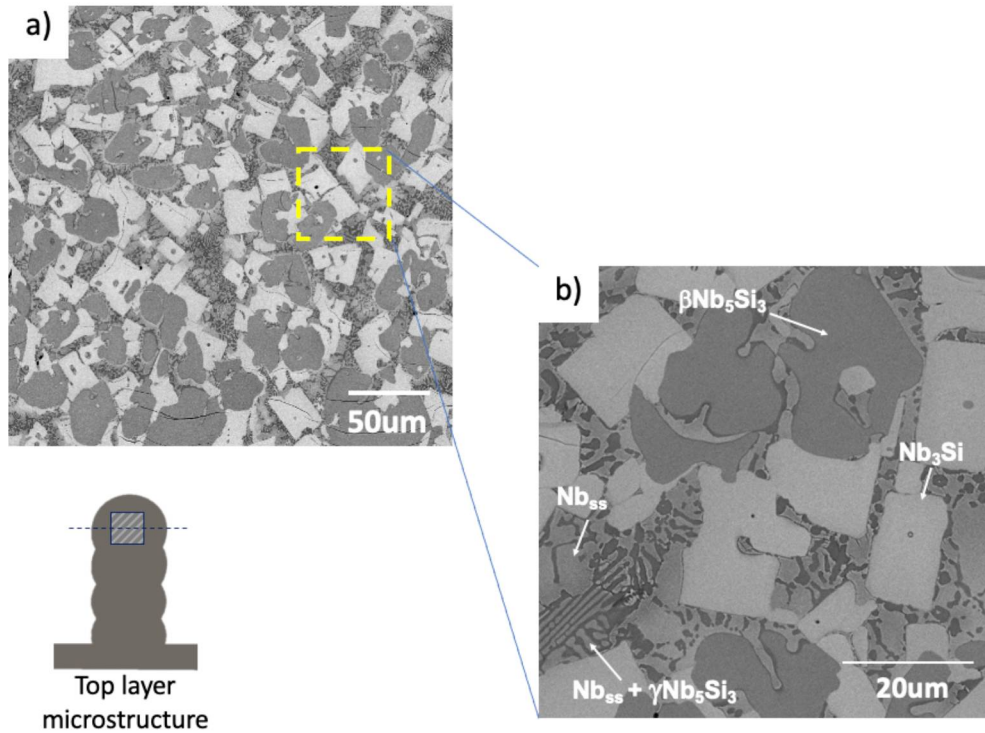
Table 9 - Average composition of phases observed in the multilayer NbTiSiZr.

Alloy	Phase	Composition (at%)		
		Nb	Si	Ti
	Nb$_{ss}$	42,4	1,5	56,2
	Nb$_3$Si	50,1	23,9	26,0
Nb24Ti18Si + 1Zr	βNb$_5$Si$_3$	36,0	36,3	27,7
	Nb$_{ss}$	40,1	1,5	58,3
eutectic	γNb$_5$Si$_3$	25,4	33,5	40,3

Figure 44 shows the as deposited microstructure (top layer), revealing higher metallurgical complexity compared to that of the NbTiZr multilayer. The complex microstructure was expected due to the low solubility of Si and Nb in each other that account for the different solidification transformations in the Nb-Si system. Furthermore, the use of elemental powder mixtures, as opposed to atomized alloys, makes it easier for different atomic arrangements in the melt pool to occur, which might induce the onset of different and simultaneous solidification sequences inducing compositional segregations.

Based on the experimental results, melting temperatures and typical solubility of elements in each phase, solidification paths for the as-deposited microstructure are proposed. During the onset of solidification, the formation of the primary βNb_5Si_3 competes with the primary $Nb(Ti,Zr,Si)_{ss}$. Both primary phases have the highest melting points of the Nb-Si system. Furthermore, because of composition fluctuations on melting pool, small variations in the composition of the primary silicide might occur. Those primary phases segregate different elements into the solidification front, changing the melting temperature in this region, and leading to different solidification paths into the melt pool. Solidification paths occurring in the melt pool are put forward and schematically represented in Figures 45, 46 and 47. The proposed solidification events and sequences are as follows:

1) The primary βNb_5Si_3 is the first to solidify at higher temperatures: $L_0 \rightarrow \beta Nb_5Si_3 + L_1$. Due to segregations into the melting pool, the remaining liquid at the solidification front, with lower Si content, induces the peritectic reaction: $\beta Nb_5Si_3 + L_1 \rightarrow Nb_3Si + L_2$. The fast solidification rate imposed by the PTA-DED process accounts for the incomplete peritectic transformation, observed as Nb_3Si surrounding the βNb_5Si_3 compound, Figure 45. The remaining liquid solidifies as the eutectic $Nb(Ti,Zr,Si)_{ss}/\gamma Nb_5Si_3$. The final microstructure formed once this solidification path is completed is represented in Figure 45, that includes a cutout from Figure 44 (b).

Figure 45 - Solidification path put forward following the formation of the primary βNb_5Si_3 on the layer processed with the NbTiSiZr powder mixture.
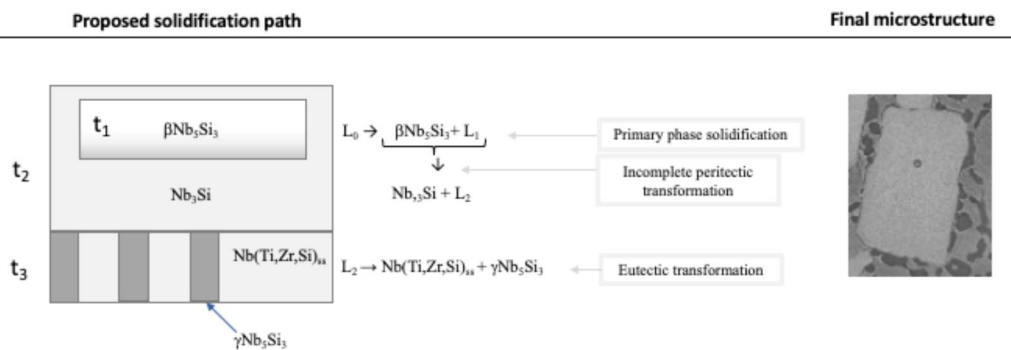
2) Compositional fluctuations in the melt pool also allows for the βNb_5Si_3 to solidify from regions where the liquid is richer in Si and Ti. As the silicide solidifies, titanium is rejected to the solidification front and the silicide ends up solidifying with titanium segregated near the phase boundary, as shown in the microstructure on Figure 46. When the remaining liquid reaches the eutectic temperature, the solidification of the eutectic $Nb(Ti,Zr,Si)_{ss}/\gamma Nb_5Si_3$ occurs. The final microstructure resulting in regions exposed to this solidification path is represented in Figure 46 that also shows a cutout from the top layer microstructure, Figure 44 (b).

Figure 46 – Alternative solidification path put forward following the formation of the primary βNb_5Si_3 on the layer processed with the NbTiSiZr powder mixture.
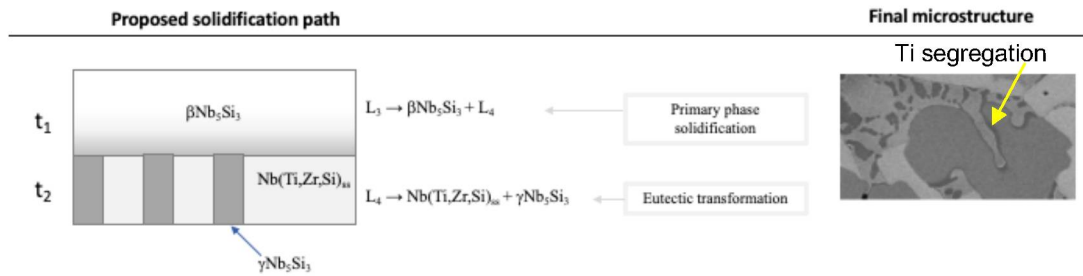
3) Also found in the microstructure is the primary $Nb(Ti,Zr,Si)_{ss}$. Its solidification in the melt pool starts from a liquid depleted in Si content and follows the solidification reaction $L_{5\ (poor\ in\ Si)} \rightarrow Nb(Ti,Zr,Si)_{ss} + L_6$, Figure 47. As the solid solution solidifies, the excess of Ti and Si is segregated in the remaining liquid that solidifies as a lamellar eutectic according to $L_6 \rightarrow Nb(Ti,Zr,Si)_{ss} + \gamma Nb_5Si_3$. The final microstructure resulted from this solidification path is represented in Figure 47 by a cutout from the top layer microstructure, Figure 44 (b).

Figure 47 - Solidification path put forward following the formation of the primary Nb(Ti,Zr,Si)$_{ss}$ on the layer processed with the NbTiSiZr powder mixture.
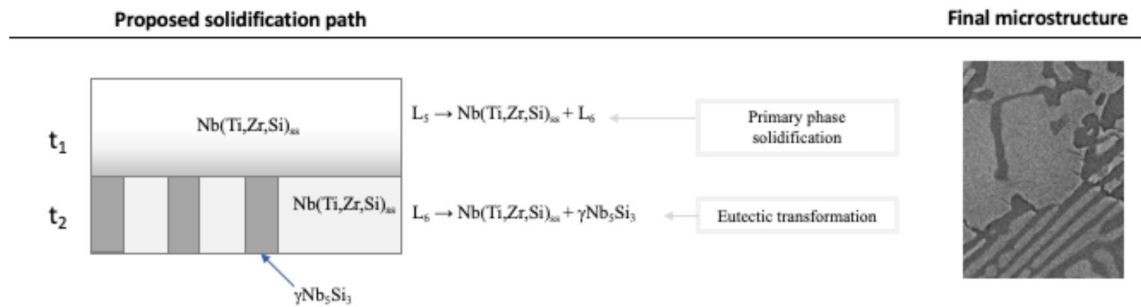
Although Titanium is present in all phases substituting Nb in crystal lattice, the preference for the Nb(Ti,Zr,Si)$_{ss}$ /γNb$_5$Si$_3$ microconstituent is confirmed by the EDS composition map, Figure 48.

Figure 48 - EDS composition map of the NbTiSiZr multilayer.
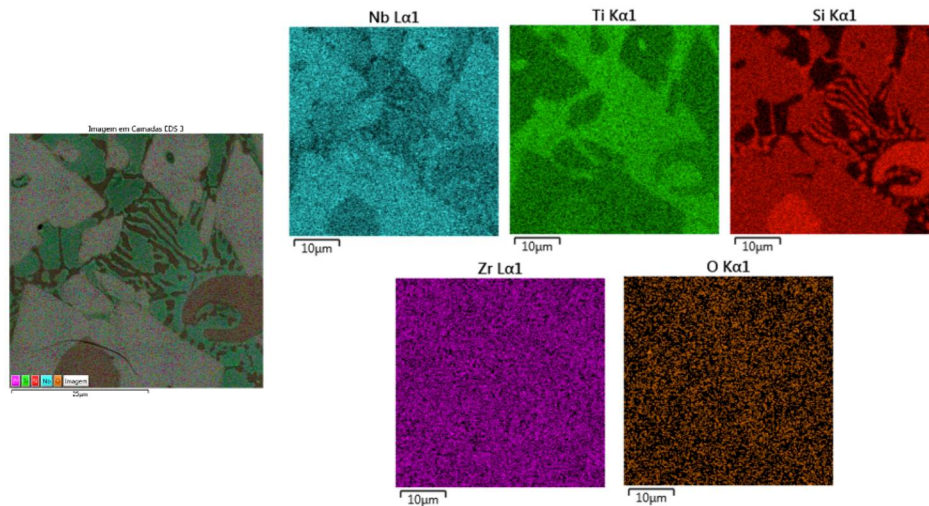
The stabilization of the Nb$_3$Si phase by Ti was reported by ZELENITSAS, (2005) when processing the Nb24Ti18Si+1Zr alloy. Also agreeing with the present study, GUO et al., (2019b) described that, because of the peritectic reaction, βNb$_5$Si$_3$ tends to be at the core of the Nb$_3$Si phase in the Nb20Si arc casted alloy.

However, the formation of the βNb$_5$Si$_3$ primary phase depends on the processing conditions as shown by TIAN et al., (2008). He processed the same alloy by arc-melting, remelting five times the buttons to achieve a homogeneous

specimen. The author did not obtain the βNb_5Si_3 primary phase in the as-cast homogenized condition.

As mentioned previously, the top layer reveals the as-deposited microstructure. However, to guarantee the quality control of an additive component it is necessary to understand how the thermal cycles affect the previously deposited layers.

When the powder mixture starts melting in the plasma arc, the elemental powders interact with each other and with the plasma gas. As the melt pool moves forward, different forces interact with the molten liquid inducing its convection such as the Buoyancy force, Lorentz force, surface tension force, and the arc shear stress, Figure 7 (KOU, 2002). This convective flow of liquid metal facilitates the heat transfer within the molten pool (MANVATKAR; DE; DEBROY, 2014). Finally, the in-situ synthesis, that starts in the plasma arc, ends up with the solidification in the molten pool when the plasma arc moves forward. After the melt pool solidifies, the solidified material undergoes multiple heating and cooling cycles as new layers are deposited on the previously deposited ones. These thermal cycles affect the microstructure evolution and the mechanical properties of the deposited layers. Understanding these effects is important to control the microstructure and properties of the final component.

The thermal cycles usually let the layers to go through three main moments: the deposition, the remelting, and the reheating. Figure 49 illustrates the thermal profile of three layers deposited one over the other, with a time interval of 60 s. It means that, after the deposition ($T_{deposition}$), the deposited layer undergoes remelting ($T_{remelting}$) and multiple reheating cycles as the process goes on ($T_{reheating}$).

The initial layer can effectively dissipate heat to the substrate due to the substrate's lower temperature and proximity to the layer. As a result, the substrate act as an efficient heat sink. However, as subsequent layers are deposited further away from the substrate, the maximum temperature gradually increases, as illustrated in Figure 49, so that the $T_{deposition\ 1} < T_{deposition\ 2} < T_{deposition\ 3}$. As the layers are deposited, the substrate gets increasingly hot, and reduce the heat extraction from the building. It results in the decrease of the temperature gradient over the build (MANVATKAR; DE; DEBROY, 2014).

Figure 49 - Thermal profile of layers deposited in an additive process..
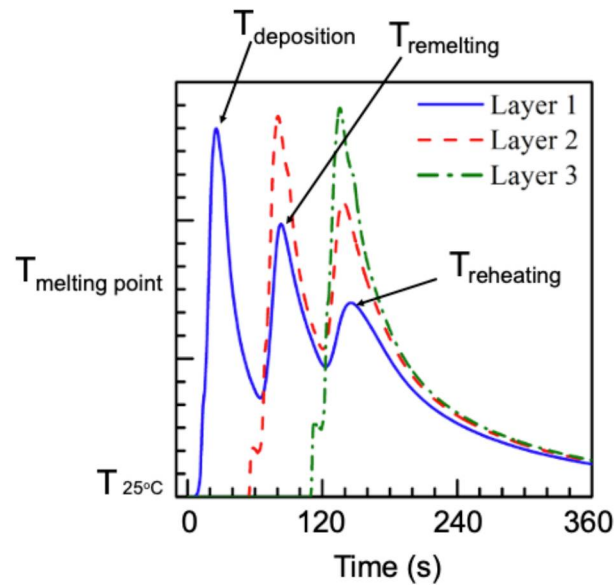
ADAPTED FROM: MANVATKAR; DE; DEBROY (2014)

The as-deposited microstructure (top layer) was previously analyzed in this study. Now, the effect of the remelting and reheating on microstructure will be assessed.

Figure 50 compares the microstructure of both top layer (as deposited) and the bottom layer (exposed to remelting and reheating). At the top layer, Figure 50 (a), equiaxed microstructure is observed but, at the bottom layer, larger silicides are identified, suggesting that the reduction in thermal gradient due to the multiple cycles allowed more time for the silicide to grow during remelting. MANVATKAR; DE; DEBROY (2014) highlight that in an additive process the remelting step is necessary to fabricate high quality AM components because it removes surface contaminants, breaks down oxide films and provides clean solid-liquid interface at the atomic level for the microstructure to grow.

Figure 50 - Microstructure from the top layer (as-deposited) (a) and the
second deposited/bottom layer (two thermal cycles) (b) of the NbTiSiZr
multilayer.
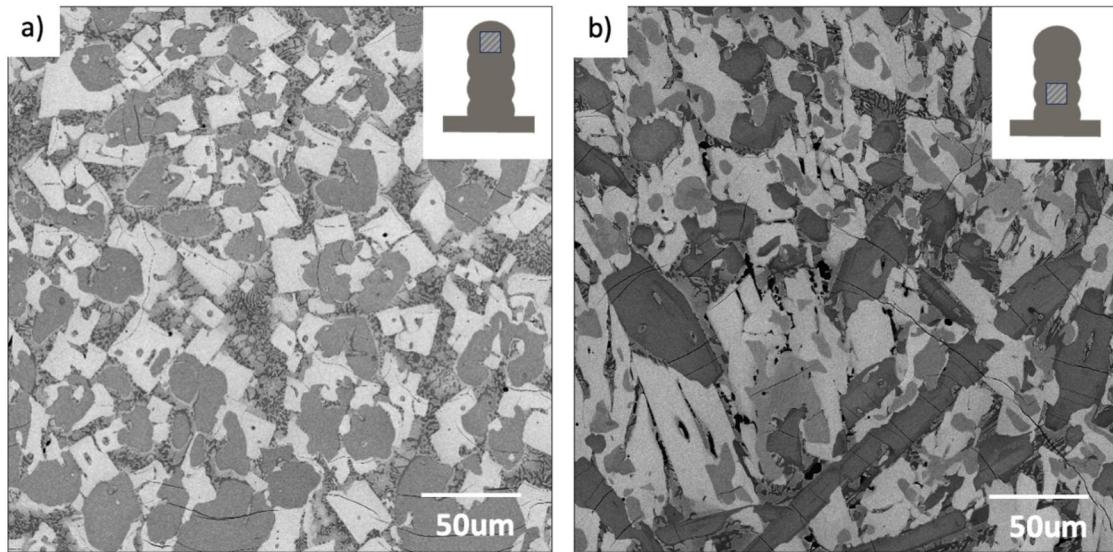
The growth of the Nb_5Si_3 silicides during the remelting is followed by a change in composition from 49,2Nb-26,6Ti-24,3Si (as-deposited layer) to 46,2Nb-29,3Ti-24,5Si (bottom layer). It represents an increase of ~3at% in Ti content, suggesting the γNb_5Si_3 was stabilized by remelting. TSAKIROPOULOS. (2018) reported the existence of a rich Ti metastable hexagonal γ-type phase. FEITOSA, (2018) also reveals that this phase is present in the as-formed microstructure due to addition of alloying elements that deviate the solidification sequence from the equilibrium condition. The formation of this Ti-rich γNb_5Si_3 silicides, Figure 50 (b), occurred in expense of the Ti-rich binary eutectic, present in higher volume fraction in the as deposited microstructure. The γNb_5Si_3 is reported to form as both primary and eutectic phase in many studies regarding Nb-Ti-Si alloys with and without Zr addition (ALLEN, A. *et al.*, 2019; FANG; GUO; QIAO, 2020; GUO, Yueling *et al.*, 2020; QIAO; GUO; ZENG, 2017; WANG, Na *et al.*, 2018). Also, WANG et al., (2018b) reported that higher Ti content contributed to the formation of the γ-type silicide, which is isomorphous with Ti_5Si_3 phases.

Because γNb_5Si_3 phase has a strong thermal expansion anisotropy, and together with differences in thermal expansion coefficient between the phases in microstructure, the thermal stresses are considerably large (WANG, Na *et al.*, 2018). It contributed for the nucleation and propagation of cracks inside this silicide. The cracks growth perpendicular to the silicide growth direction during remelting, which was parallel to the higher heat flow.

The reduced number of slip systems of γ-type hexagonal silicide compared to the αNb_5Si_3, are among the key reasons for the formation of cracks (WANG, Na *et al.*, 2018). However, regardless the silicide that solidifies, it will always show a brittle behavior. When the silicide is in a large size, the stress in this overgrown phase tends to be higher and, together with the low toughness, account for the formation of cracks. That is why WANG et al., (2018a) and YUAN et al.,(2014) highlighted that the ideal balance between the size, morphology, and volume of the intermetallic phase, together with the formation of a tough matrix network that might absorb stresses, can play an important role in optimizing the mechanical properties of the compounds in Nb/Si system.

In Figure 50 (b) it is shown that most cracks are confined into the overgrown γNb_5Si_3 silicide. It happens because the other phases in microstructure, including the Nb_3Si silicide, have higher toughness and smaller size, contributing to an efficient absorption of stresses, effectively stopping crack propagation.

A consequence of the remelting step is also the growth of the Nb_3Si phase, Figure 50 (b), that also increased its Ti content after remelting in ~6at%. The as-deposited Nb_3Si shows composition 51,3Nb;24,9Ti;23,8Si, whereas the bottom layer shows an increase in Ti content, 44,9Nb;30,8Ti;24,2Si. It suggests that the lower thermal gradient during remelting cycle helps both the growth of silicides, and the reduction in the segregation of Ti during the solidification so that its concentration at the final stage of solidification is lower, reducing the formation of the eutectic phase.

Further changes due to the remelting cycle are observed at the interlayer region, highlighted in Figure 51, where large and blocky γNb_5Si_3 phase is observed. The remelting of the previously deposited layer favoured the epitaxial growth during the solidification of the silicide compound at the interface between

layers. The epitaxial growth from the existing silicides happens since both have the same crystal structure, eliminating the need for nucleation.

Figure 51 - Transverse cross section microstructure at the interlayer region (in red) in the NbTiSiZr multilayer.

Interface between layers
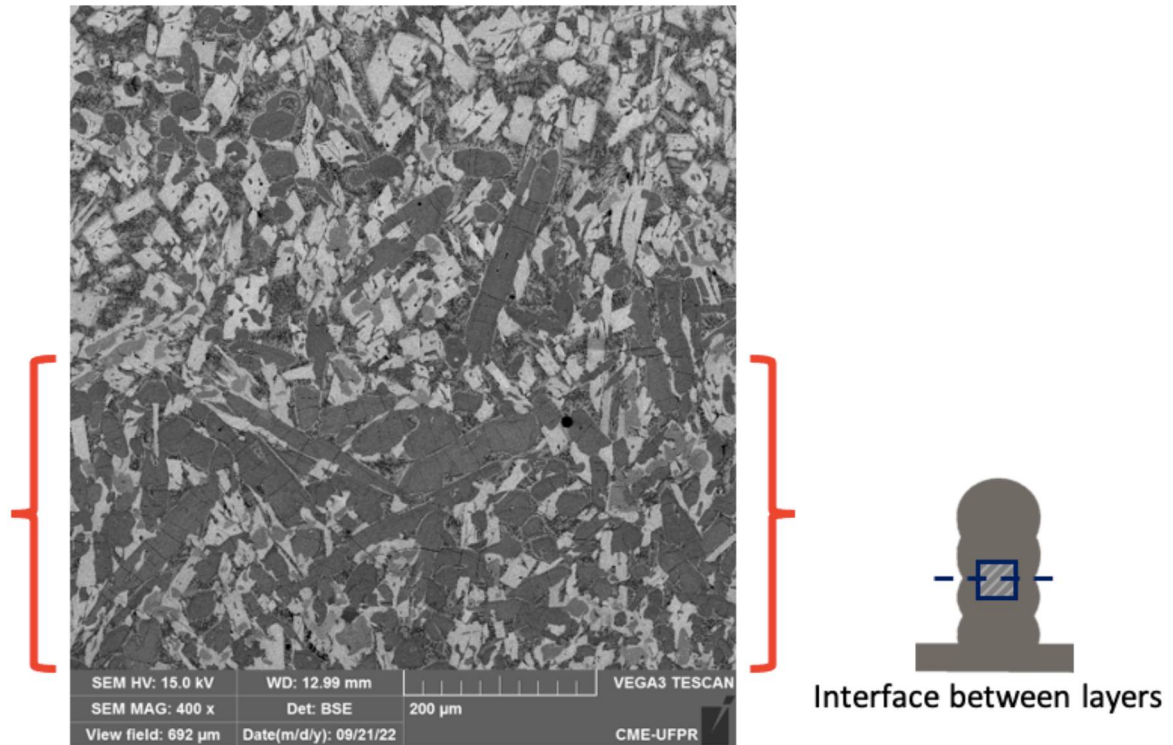
DEBROY et al., (2018) highlight that at this stage, near the fusion line (melt pool boundary), the growth is dominated by the base metal. However, moving away from the melt pool boundary, the competitive growth between the crystals with different crystallographic orientations dominates the formation of the solidification microstructure. That is why in Figure 51 it is possible to observe that, moving away from the interface region, the microstructure is closer to the as deposited and the solidification transformations previously described account for the observed phase distribution.

Just like with the overgrown silicides at the bottom layer Figure 50 (b), at the interface between layers perpendicular cracks are also confined inside silicides, Figure 52. Again, this is a consequence of the surrounding higher ductility and tough phases, such as the eutectic $Nb(Ti,Zr,Si)_{ss}$ (in detail) that act as an obstacle to crack propagation in the microstructure.

Figure 52 - Cracks within the low toughness γNb_5Si_3 phase at the interface between layers in the NbTiSiZr multilayer.
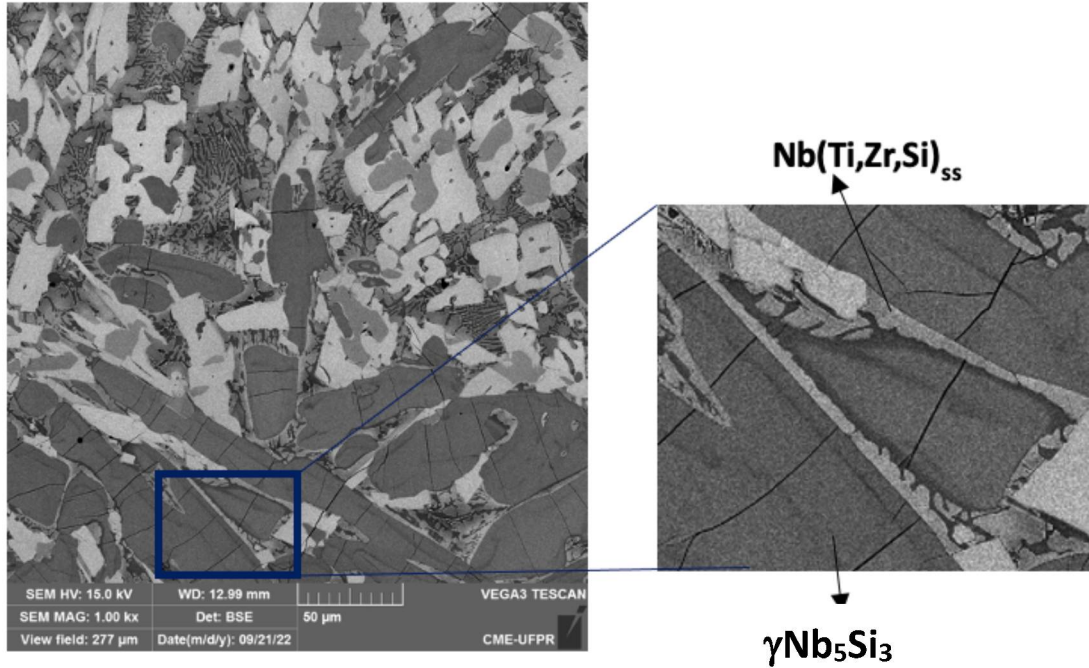
Regarding the reheating thermal cycle, no solid-state transformation was identified at the bottom layer of the multilayer processed with the mixture NbTiSiZr.

4.6. Nb24Ti18Si5Al+1Zr

In previous studies (Appendix II) it was shown that the addition of Al in Ti-free Nb-Si powder mixtures leads to the solidification of the eutectic Nb_{ss}/Nb_5Si_3, as revealed also by (MENON; PARTHASARATHY; MENDIRATTA, 2006). The Nb_{ss} in the eutectic works as a tough network around the Nb_5Si_3 silicides accommodating thermal stresses. The presence of Al in the Nb-Si-Al ternary powder mixture also mitigated pesting oxidation at ~800°C compared to the binary Nb-Si alloy previously analysed by (CARDOZO; D'OLIVEIRA, 2022). The addition of Al in Ti-rich Nb silicide powder mixtures will now be investigated.

The addition of aluminum to the NbTiSiZr powder mixture changed the solidification path in the deposited layers, but did not compromise the *in-situ*

84

synthesis of silicides. For layers processed with the Nb24Ti18Si5Al + 1Zr powder mixture, the as-deposited microstructure mainly consists of $Nb(Ti,Si,Al,Zr)_{ss}$, γNb_5Si_3 silicide, and the βNb_5Si_3 silicide. These phases are revealed by X-ray diffraction analysis, Figure 53, and the composition assessed by EDS, Table 10.

Figure 53 - XRD of the top of the NbTiSiAlZr multilayer.
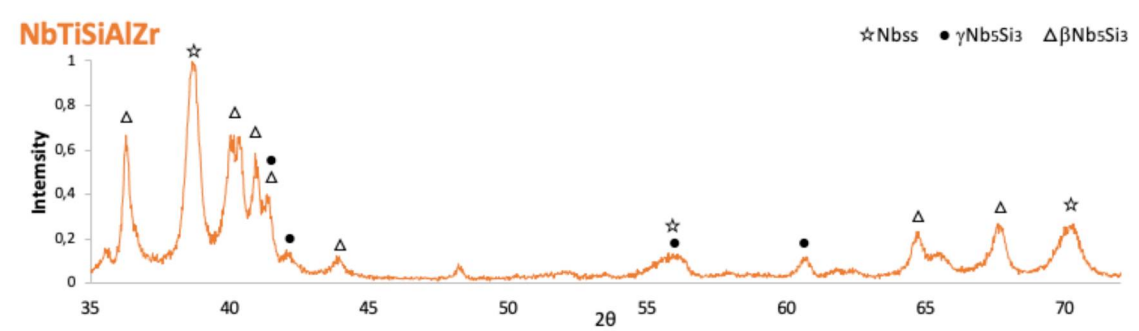
Table 10 -Average composition of phases observed in the NbTiSiAlZr multilayer.

Alloy		Phase	Composition (at%)			
			Nb	Si	Ti	Al
		γNb_5Si_3	36,8	33,3	27,0	2,8
		βNb_5Si_3	41,2	31,2	22,9	4,7
		Nb_{ss}	41,1	2,4	46,5	9,9
	Eutectic`	γNb_5Si_3	30,6	20,7	42,3	5,9
Nb24Ti18Si5Al + 1Zr		Ti_{ss}	34,1	5,7	52,4	7,4
		Nb_{ss}	38	1,9	35,8	10,8
	Eutectic``	γNb_5Si_3	28,1	30,5	33,2	5
		Nb_{ss}	40,8	1,5	47,5	10,2
	Eutectic```	βNb_5Si_3	40,7	26	27	6,2

Figure 54 shows the microstructure at the top layer of the multilayer processed with the NbTiSiAlZr powder mixture and confirm the synthesis of the silicides, as well as the suppression of the Nb_3Si silicide, present in the NbTiSiZr layers.

Figure 54 – Microstructure at the top layer of the multilayer NbTiSiAlZr (a) general view (b) details of the microstructure.
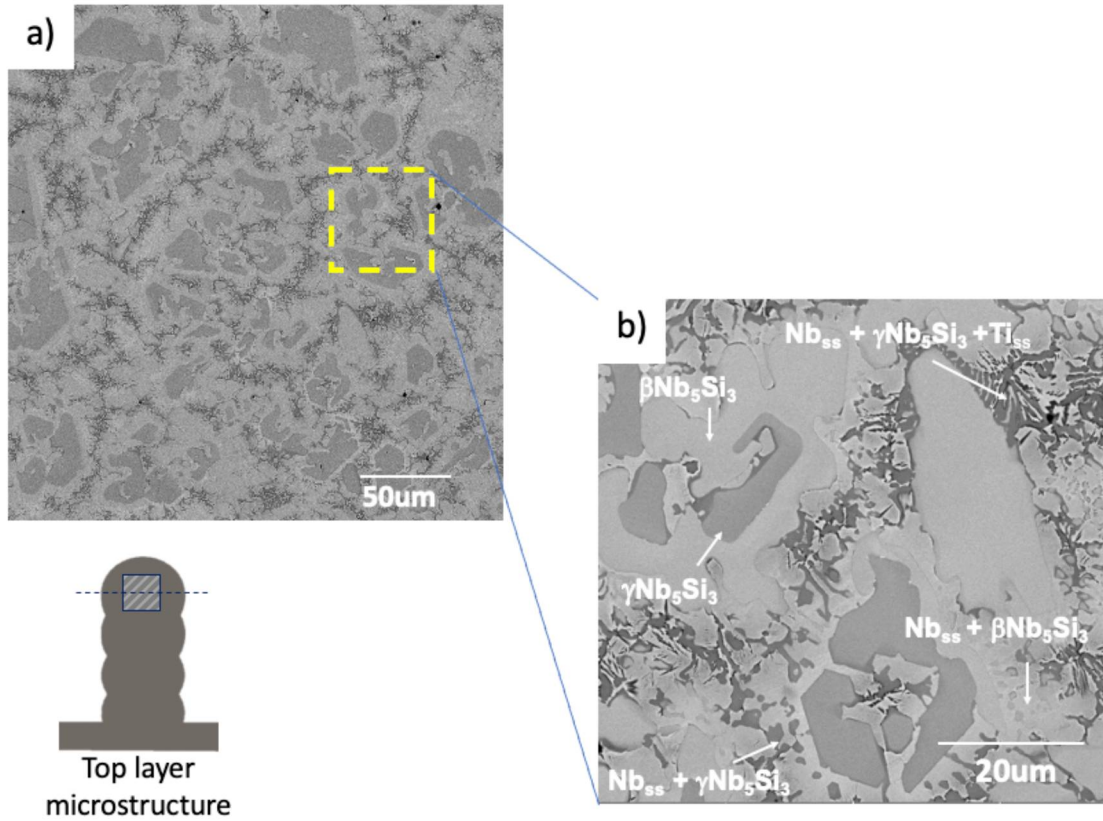
The microstructure, together with EDS analysis, reveals the synthesis of the βNb$_5$Si$_3$ phase, rich in Al. LI et al., (2020) reported that Al additions stabilize the βNb$_5$Si$_3$, with Al substituting Si sites, supporting the observations in the as deposited layer, Figure 54. Detailed analysis on the as deposited microstructure reveals that the addition of Al also resulted in three eutectics: a three-phase eutectic containing Nb(Ti,Al,Si)$_{ss}$/γNb$_5$Si$_3$/Ti$_{ss}$, an anomalous eutectic containing Nb(Ti,Al,Si)$_{ss}$/γNb$_5$Si$_3$, and a second anomalous eutectic containing Nb(Ti,Al,Si)$_{ss}$/βNb$_5$Si$_3$. The composition of eutectic phases was also assessed by EDS, Table 10. The EDS composition map, Figure 55, confirm the formation of the three-phase eutectic in the terminal stage of solidification.
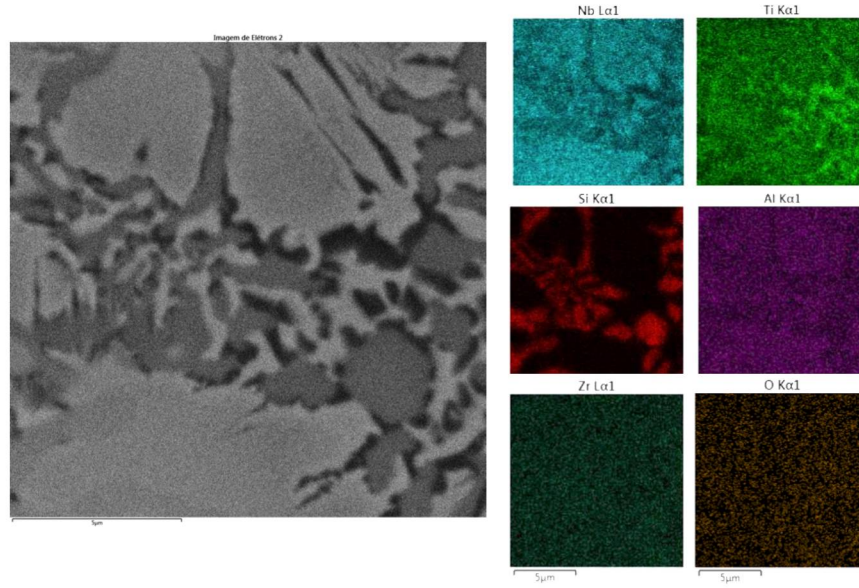
Considering the experimental results, the melting point, and the typical solubility of elements in each phase, solidification paths for the as deposited microstructure are put forward.

During the initial period of solidification, the primary γNb_5Si_3, stabilized by Ti and Zr, is solidified together with the βNb_5Si_3 silicide. These phases form as a consequence of chemical composition fluctuations in the molten liquid and the interaction between alloying elements that might have started in the plasma arc. These phenomena induce segregation in the melt pool as the two solidification sequences occur simultaneously. Furthermore, as with the NbTiSiZr multilayer, because of composition fluctuations in melting pool, the remaining liquid surrounding the primary γNb_5Si_3 can be rich or poor in Si and Al, resulting in different solidification paths in the molten pool. The proposed solidification paths are schematically represented in Figures 56, 57 and 58, and are described as follows:

1) The primary γNb_5Si_3 solidifies at high temperature from the Ti and Zr rich liquid following the solidification reaction $L_4 \rightarrow \gamma Nb_5Si_3 + L_5$. The remaining liquid is enriched in Al and Ti and solidifies as an anomalous binary eutectic $L_5 \rightarrow Nb(Ti,Al,Si)_{ss} + \gamma Nb_5Si_3 + L_6$. Further cooling of the remaining liquid leads to the formation of a ternary eutectic: $L_6 \rightarrow Nb(Ti,Al,Si)_{ss} +$

$\gamma Nb_5Si_3 + Ti_{ss}$. The final microstructure resulted from this solidification path is represented in Figure 56 that includes a cutout from the top layer microstructure, Figure 54 (b).

Figure 56 –Solidification path put forward following the formation of the primary γNb_5Si_3 on as processed layer processed with the NbTiSiAlZr powder mixture.
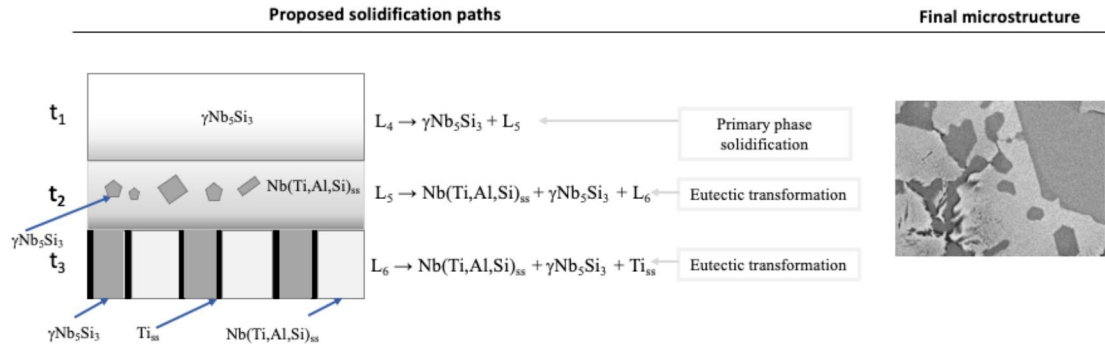
2) The γNb_5Si_3 compound might also solidify from a region of the liquid slightly richer in Al. This compound forms following the initial solidification ($L_0 \rightarrow \gamma Nb_5Si_3 + L_1$) that favored the segregation of Al. The richer Al liquid accounts for the solidification of the βNb_5Si_3 silicide. The cooling rate induces the liquid to go through a sequence of eutectic reactions. First, the formation of a binary eutectic occurs, $L_2 \rightarrow Nb(Ti,Al,Si)_{ss} + \beta Nb_5Si_3 + L_3$, which is the anomalous eutectic containing $Nb(Ti,Al,Si)_{ss}/\beta Nb_5Si_3$. At lower temperatures, the ternary eutectic forms $L_3 \rightarrow Nb(Ti,Al,Si)_{ss} + \gamma Nb_5Si_3 + Ti_{ss}$. The final microstructure resulted from this solidification path is represented in Figure 57 by a cutout from the as deposited microstructure, Figure 54 (b).

Figure 57 – Alternative solidification path put forward following the formation of the γNb_5Si_3 on as processed layer processed with the NbTiSiAlZr powder mixture.
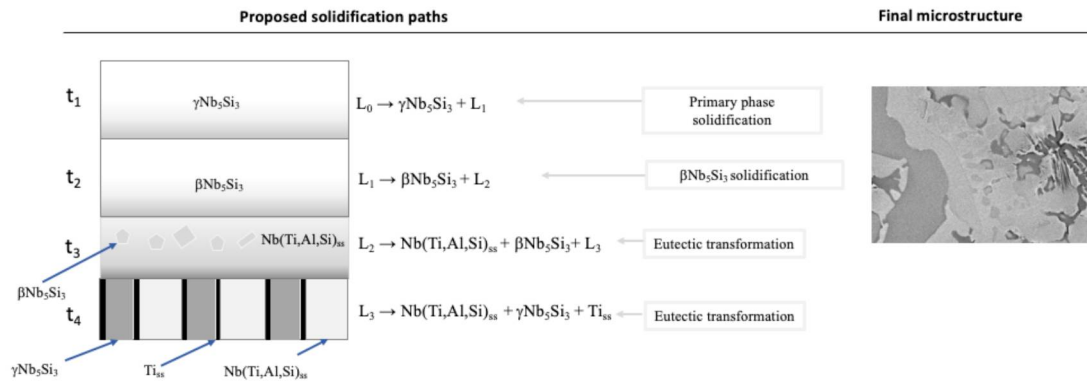
3) The βNb_5Si_3 silicide solidifies from the liquid depleted in Ti, but rich in Al, following the solidification reaction $L_7 \rightarrow \beta Nb_5Si_3 + L_8$, segregating Ti and Al into the remain liquid. The formation of the anomalous binary eutectic is suppressed, and the remaining Ti-rich liquid solidifies following the eutectic reaction $L_8 \rightarrow Nb(Ti,Al,Si)_{ss} + \gamma Nb_5Si_3 + Ti_{ss}$, resulting in the lamellar three-phase eutectic $Nb(Ti,Al,Si)_{ss}/\gamma Nb_5Si_3/Ti_{ss}$. The final microstructure resulted from this solidification path is represented in Figure 58 by a cutout from the as deposited microstructure, Figure 54 (b).

Figure 58 - Solidification path put forward following the formation of βNb_5Si_3 on the as processed layer processed with the NbTiSiAlZr powder mixture.
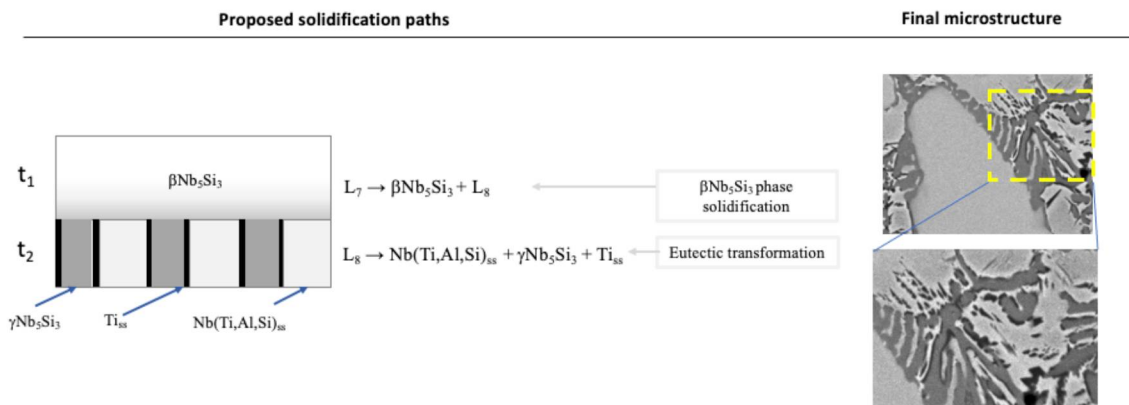
The EDS composition map on Figure 59 confirms the growth of the Al-rich β Nb_5Si_3 adjacent to the primary Ti-rich silicide γNb_5Si_3, the anomalous eutectic containing $Nb(Ti,Al,Si)_{ss}$ / βNb_5Si_3 and the terminal solidification with the three-phase eutectic $Nb(Ti,Al,Si)_{ss}$ + γNb_5Si_3 + Ti_{ss}.

Figure 59 – EDS composition map at top layer processed with the NbTiSiAlZr powder mixture.
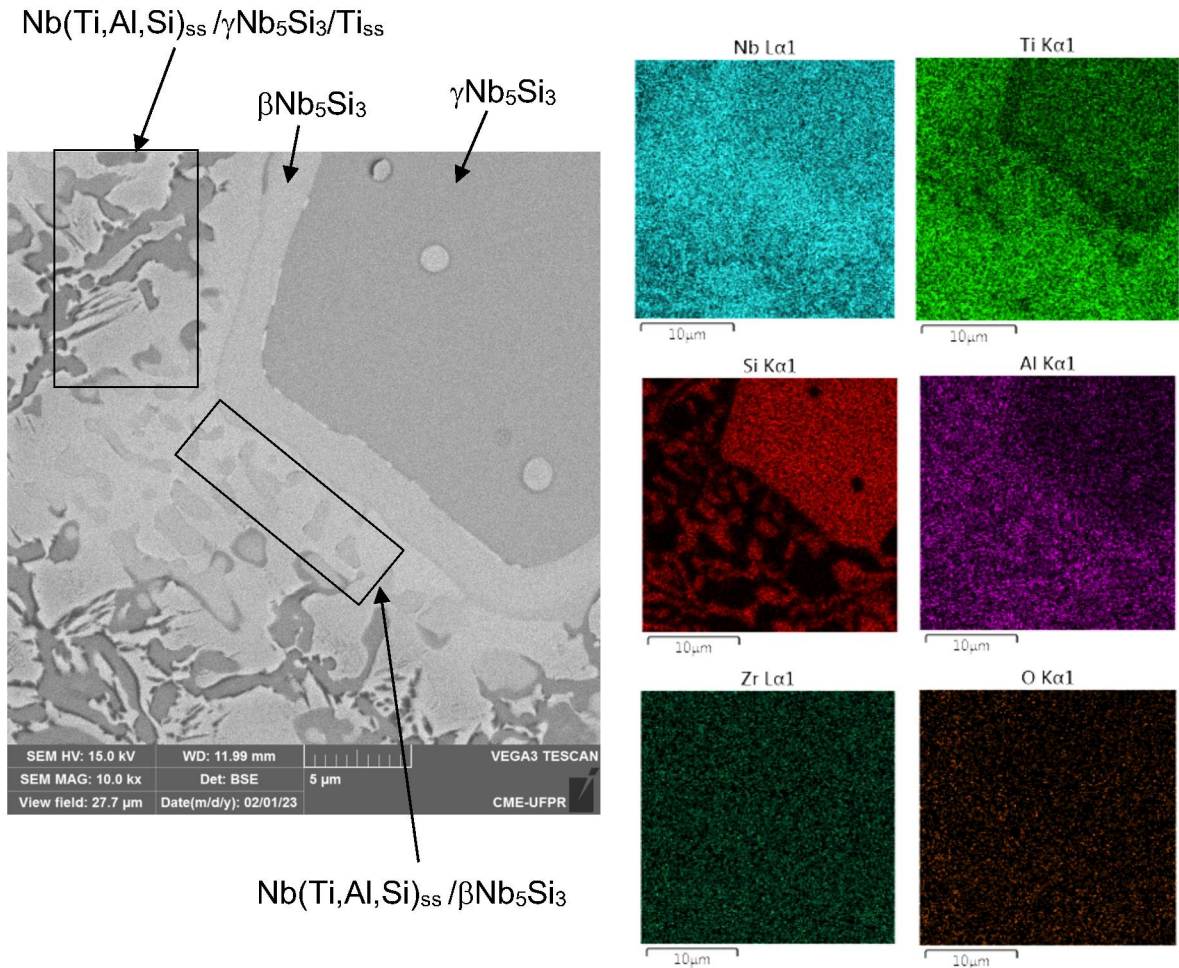
Hardness along the multilayer transverse cross section is uniform from the top to the bottom and has an average of 840 ± 36HV. The average shows a slight decrease comparing to the NbTiSiZr multilayer (-2,8%). PAPADIMITRIOU et al. (2014) reveal that, contrary to the α and γ 5-3 silicide, the alloying with Ti makes the βNb_5Si_3 more ductile.

As with the multilayers processed with the powder mixture NbTiSiZr, the remelting caused by multiple thermal cycles did not result in different phases, Figure 60 (b), but changed their morphology. As explained in detail on previous section, the hot substrate during remelting reduced the temperature gradient during solidification, given more time for silicides to grow and allowing the overgrowth of γNb$_5$Si$_3$ silicides at the expense of the Ti-rich three-phase eutectic.

Figure 60 - Microstructure from the top layer (as deposited) (a) and the second deposited/bottom layer (two thermal cycles) (b) of the NbTiSiAlZr multilayer.
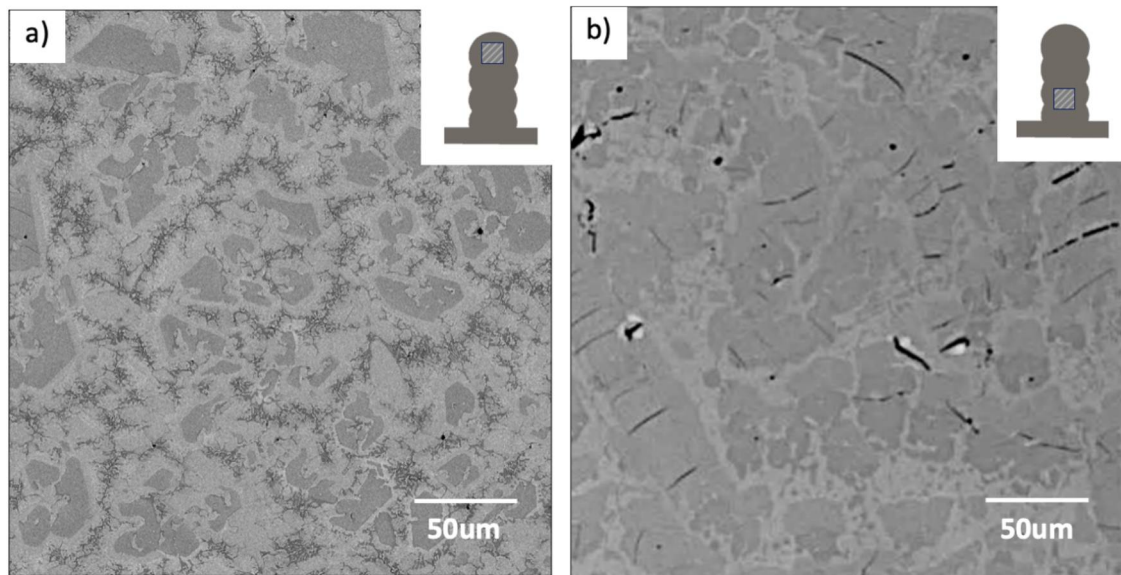
Differently from the NbTiSiZr multilayer, the addition of Al to the powder mixture seems to contribute to a higher stability of phase compositions the remelting and reheating thermal cycles. The γNb$_5$Si$_3$ silicides, despite overgrowing at the expense of the other phases, kept its composition almost stable after these thermal cycles, changing from 36,2Nb – 33,3Si – 27,3Ti – 2,8Al – 0,2Zr (as-deposited) to 35,3Nb – 33,5Si – 28,3Ti – 2,5Al – 0,5Zr (after remelting and reheating). The βNb$_5$Si$_3$ silicide composition showed a slightly decrease in Ti content (~2,7at%), changing from 42,1Nb – 31,2Si – 22Ti – 4,7Al (as deposited) to 40,6Nb – 29,3Si – 24,7Ti – 5,1Al – 0,4Zr (after remelting and reheating thermal cycles).

Although Al is expected to increase the toughness of Nb-Si alloys (TSAKIROPOULOS, P., 2022), the overgrown γNb$_5$Si$_3$ silicides are still vulnerable to thermal stresses generated by the different coefficients of thermal expansion of phases during the heating and cooling of additive thermal cycles. Figure 60 (b) show cracks in γ-silicide perpendicular to its growth direction, that followed the maximum heat flow direction at the solid-liquid interface.

Figure 61 shows the bottom layer microstructure in higher magnification. It can be observed that the cracks only form in the large rod-like γNb$_5$Si$_3$ silicide. It suggests that the γNb$_5$Si$_3$ is the phase with lower toughness in the microstructure. Both βNb$_5$Si$_3$ and the eutectics have higher toughness and stop crack propagation.

Figure 61 - Detail of the bottom layer microstructure (exposed to remelting and reheating) of the multilayer processed with the NbTiSiAlZr powder mixture.
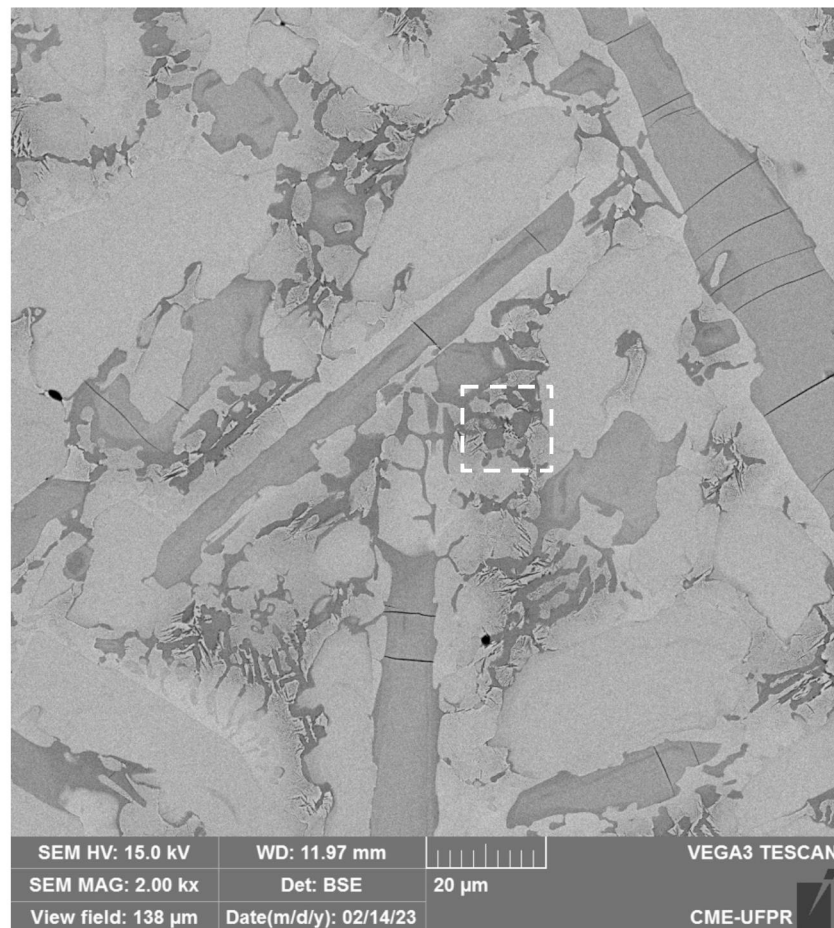
Additive processes are usually expected to form an out of equilibrium microstructure due to the high cooling rates. This phenomenon can lead to changes in microstructure when exposed to multiple heating and cooling cycles.

In the Nb-Ti phase diagram, for example, the solubility of the bcc βTi in bcc βNb is total above ~880°C. However, at room temperature, the α-hexagonal and the β-cubic Ti phases can coexist. During the reheating of previously deposited layer, the hexagonal αTi phase can segregate from the bcc βNb$_{ss}$.

Furthermore, ALLEN, (2019) also explain that the excess of Ti in Nb$_{ss}$ can be expelled and trapped at the grain boundary if no adjacent phase can incorporate this element. It follows that, Ti can also diffuse along the grain boundaries and segregate as αTi$_{ss}$. This segregation of the αTi phase at the grain boundaries is revealed in Figure 62, that shows in high magnification the microstructure from the region inside the rectangle with dashed edges on Figure 61.

Figure 62 - Higher magnification of the microstructure from the region highlighted by the rectangle with dashed edges on Figure 61.
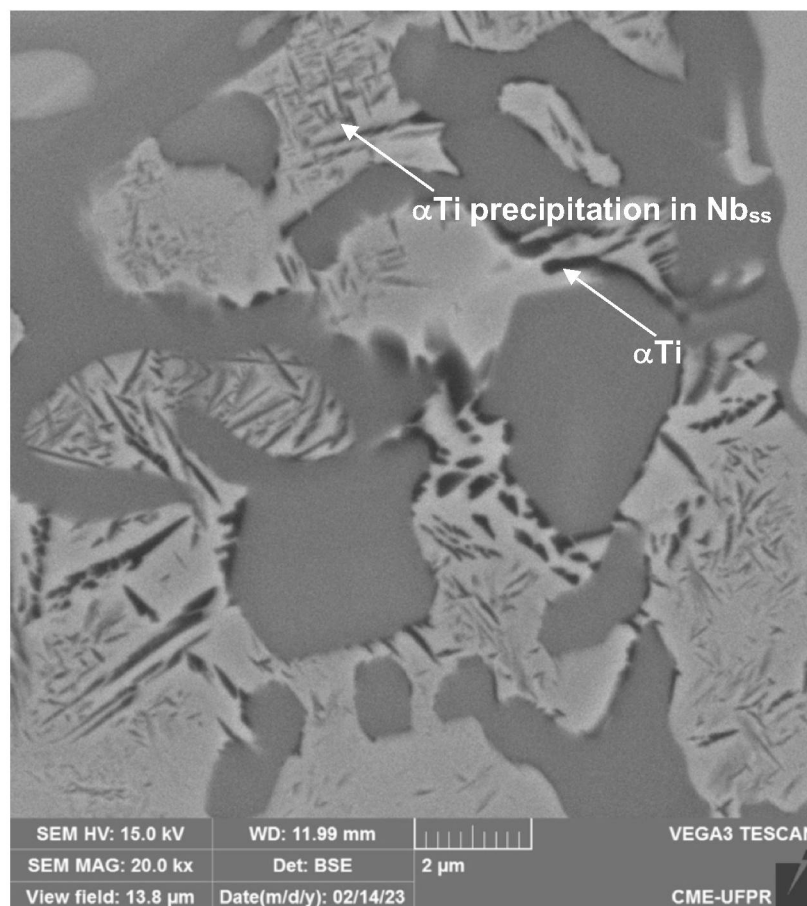
Despite of the grain boundary segregation, some fine precipitates can be identified inside the Nb_{ss}, Figure 62. For additive manufacturing of Ti6Al4V alloy, SALSI; CHIUMENTI; CERVERA (2018) reported that during the cooling down, mainly in case of fast cooling rates, the αTi martensite can form with acicular shape, like small needles. Together with the fast-cooling rate effect, some alloying elements can stabilize the αTi phase. This is the case of Al, O, N and C. The Nb_{ss} phase contains Al in solid solution and can also have O, N and C in interstitial sites.

Also associated with the reheating, nano scale silicides might precipitate in Nb_{ss} (REYES et al., 2022). Taking the binary Nb-Si phase diagram, under equilibrium conditions the solubility of Si in Nb reaches the maximum value of 3,5at% at ~1900°C. However, at room temperature, Si is practically insoluble in Nb_{ss}. Extrapolating to the as deposited microstructure in this present study (top layer), the Si content in Nb_{ss} ranges from 3at% to 8at%. In other words, at room temperature, the Nb_{ss} of the as deposited layer is supersaturated in Si so that further reheating of the microstructure might lead to precipitation of silicides. REYES et al., (2022b) reported precipitation of nano size $\delta Nb_{11}Si_4$ when heating the Nb-20Si-25Ti-6Al-3Cr-3Mo samples processed by spark plasma sintering using pre-alloyed powder. KASHYAP; TIWARY; CHATTOPADHYAY, (2013) also mentioned that Al additions can help the formation of the δ fine precipitates and relate it to a multifold improvement in the hardness of Nb_{ss}, hence mechanical properties.

Considering the experimental results, the addition of Al to the NbTiSiZr powder mixture increased the microstructure complexity mainly after the remelting and reheating of the microstructure due to the formation of new phases by precipitation and segregation at grain boundaries.

Aluminum is one of the major alloying additions that contributes to the oxidation resistance of Nb-silicide multi component alloys. Dynamic temperature exposure in air up to 1350°C confirm that the addition of Al lead to oxidation improvement of multilayers at temperatures higher than ~600°C, Figure 63.

LEONT'EV et al., (2016) reported, for multi alloyed Nb-Si alloys with 1,8at%Al, that the oxidation of Nb_{ss} components starts from 563,6°C to 776°C

and the oxidation of Nb silicides start at ~987°C. A similar behavior is observed for the NbTiSiZr multilayer, Figure 63. However, the addition of a higher amount of Al (5at% in this present study) resulted in an improve in oxidation resistance from ~590°C on. It suggests that the selective oxidation of Al improved the oxidation resistance of Nb$_{ss}$. This result agrees with (LI, Yunlong *et al.*, 2020). He comments that it is expected for Al to improve the oxidation resistance of the Nb$_{ss}$ due to preferential oxidation in this first oxidation stage

Figure 63 – TGA analysis of multilayers processed with the NbTiSiZr and the NbTiSiAlZr powder mixture.
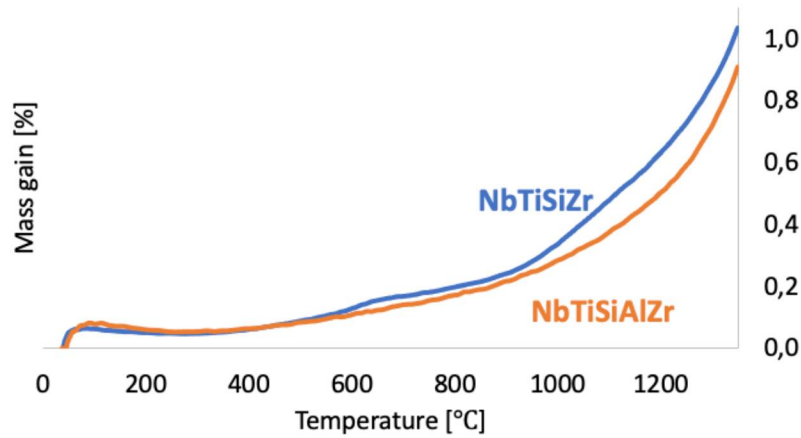
4.7.   Nb24Ti18Si5Al5Cr+1Zr

The addition of Cr to the powder mixture did not change the uniform hardness across deposited multilayers, (869 ± 34HV). XRD analysis, Figure 64, shows that the as deposited microstructure processed with the Nb24Ti18Si5Al5Cr+1Zr powder mixture (top layer), consists of Nb(Ti,Si,Al,Zr,Cr)$_{ss}$, the γNb$_5$Si$_3$ silicide, and the Cr$_2$Nb Laves phase. Element distribution in each phase was assessed by EDS analysis, Table 11.

Figure 64 - XRD of the top of the NbTiSiAlCrZr multilayer.
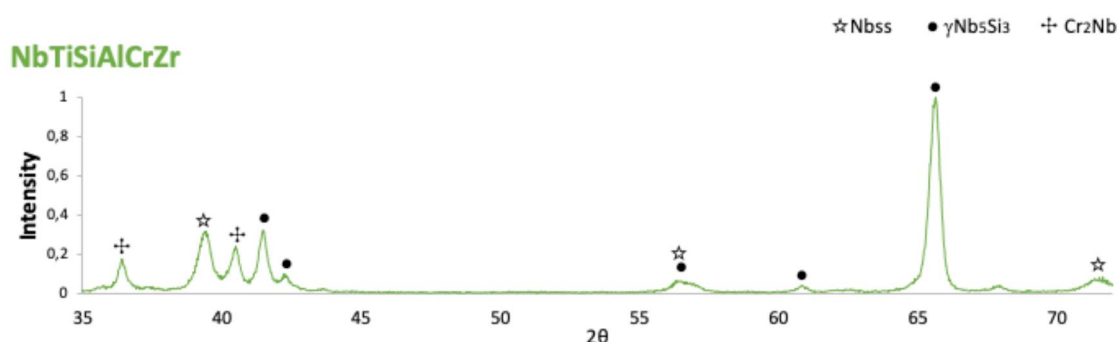
Table 11 -Average composition of phases observed in the multilayer NbTiSiAlZr.

Alloy		Phase	Composition (at%)				
			Nb	Si	Ti	Al	Cr
		Nb$_{ss}$	38,0	3,1	35,1	10,7	12,9
		γ Nb$_5$Si$_3$	32,4	33,2	29,9	2,9	1,4
Nb24Ti18Si5Al5Cr + 1Zr		γ Nb$_5$Si$_3$	27,4	30,0	34,2	5,1	2,8
	Eutectic′	Cr$_2$Nb	28,2	4,3	38,4	8,7	20,3
		Ti$_{ss}$	36,4	1,9	36,5	11,1	14,2
	Eutectic ″	γ Nb$_5$Si$_3$	26,6	29,4	35,2	5,1	3
		Nb$_{ss}$	38	1,9	35,8	10,8	13,5

The as deposited microstructure of the NbTiSiAlCrZr multilayer (top-layer) confirms the synthesis of the silicides, Figure 65. The as-processed microstructure exhibits a better homogeneity than the multilayers processed without Cr addition in powder mixture.

The microstructure from the top layer reveals that the βNb$_5$Si$_3$ Al-rich silicide is suppressed by Cr addition in the as deposited condition. Furthermore, the Cr$_2$Nb Laves phase is stabilized in a three-phase eutectic that now contain the γNb$_5$Si$_3$/Cr$_2$Nb/Ti$_{ss}$ phases distributed more evenly in the microstructure but apparently with lower volume fraction. The anomalous eutectic Nb(Ti,Si,Al,Zr,Cr)$_{ss}$/γNb$_5$Si3 and the primary γNb$_5$Si$_3$ remain, but with different morphologies. The latter exhibits hexagonal or ′H` like morphology and is

96

distributed more evenly in the Nb_{ss} matrix. A similar microstructure is described by QIAO; GUO; ZENG (2017) for Nb-22Ti-15Si-5Cr-3Hf-3Al-2Zr ingots processed by vacuum non-consumable arc melting under ultra-high-purity argon atmosphere. The EDS composition maps, Figure 66, confirm the segregation of Ti and Cr to the three-phase eutectic.

Figure 65 - Microstructure at the top layer (a) general view (b) details of the microstructure.
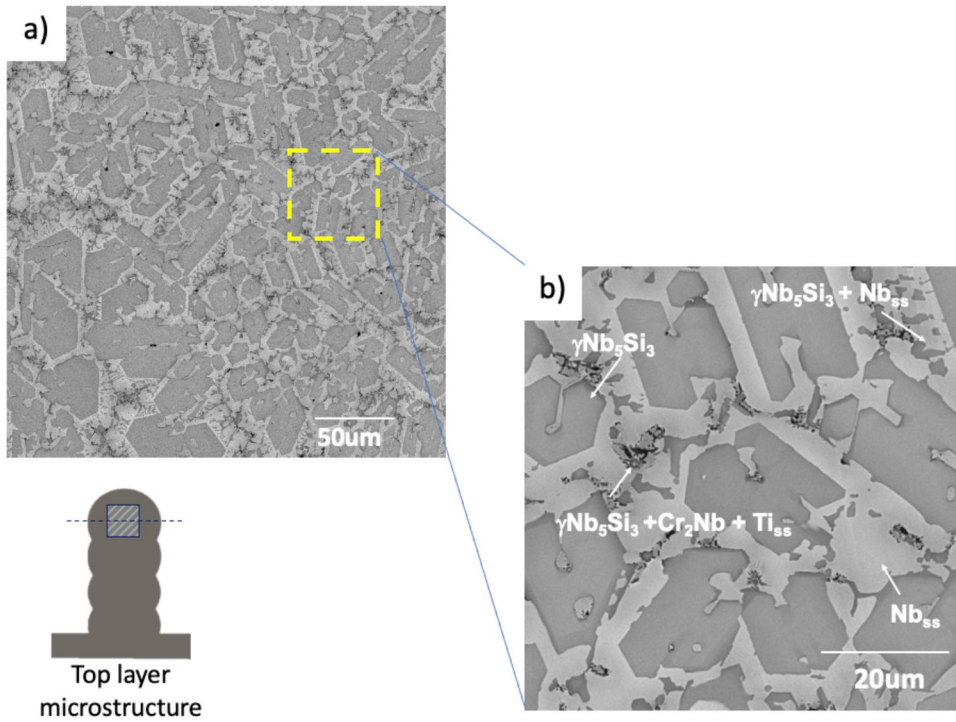
Considering the experimental results, the melting point, and the typical solubility of elements in each phase, solidification paths for the as-deposited microstructure are put forward. The primary γNb_5Si_3 is the first to solidify, stabilized by Ti and Zr. Considering the fluctuations on chemical composition in the melt pool, different solidification paths might occur. The proposed solidification paths are schematically represented in Figures 67, 68 and 69, and are described as follows:

Figure 66 - EDS composition map of the ternary eutectic in the microstructure of the top layer of the multilayer NbTiSiAlCrZr
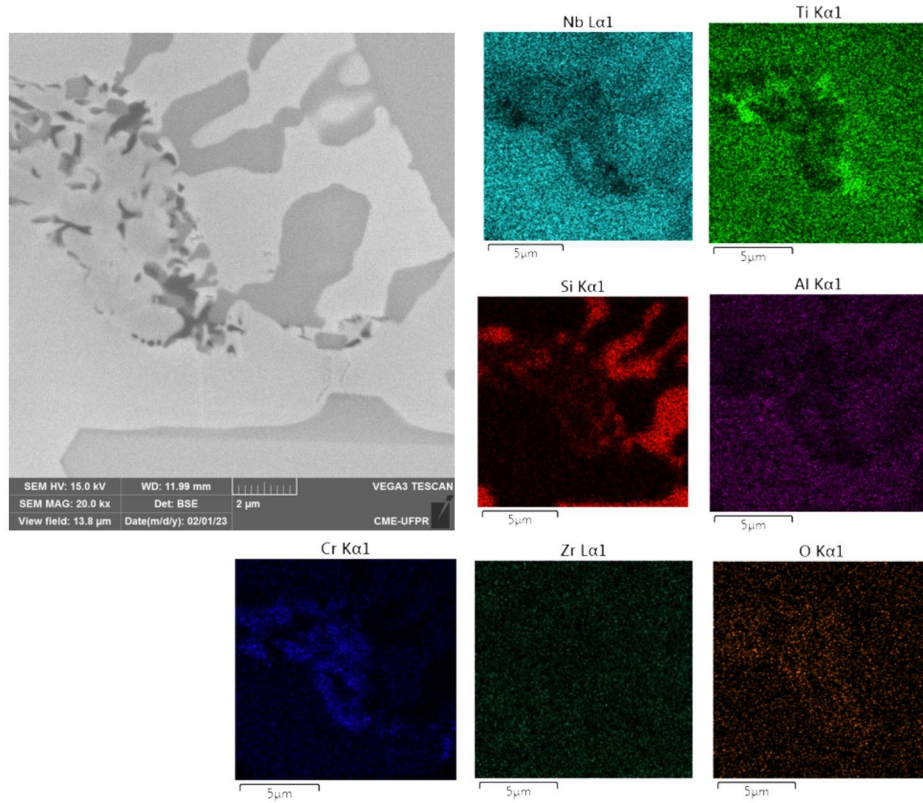
1) The high temperature γNb_5Si_3 silicide grows from the liquid rich in Ti and Zr. During the solidification, the liquid is enriched with lower melting point elements Ti, Cr and Al. Aluminum plays an important role in stabilizing the eutectic containing Nb_{ss}, inducing during cooling the transformation $L_1 \rightarrow Nb(Ti,Si,Al,Cr)_{ss} + \gamma Nb_5Si_3 + L_2$ that forms the eutectic containing $Nb(Ti,Si,Al,Cr)_{ss}/\gamma Nb_5Si_3$. This binary eutectic is observed in the microstructure both in lamellar, Figure 67, and anomalous type, Figure 68. The remaining liquid solidifies when it reaches the ternary eutectic temperature, solidifying as the ternary eutectic containing γNb_5Si_3 /Cr_2Nb/Ti_{ss}.

Figure 67 - Solidification path put forward following the formation of the primary γNb_5Si_3 and the lamellar binary eutectic on the top layer processed with the NbTiSiAlCrZr powder mixture.
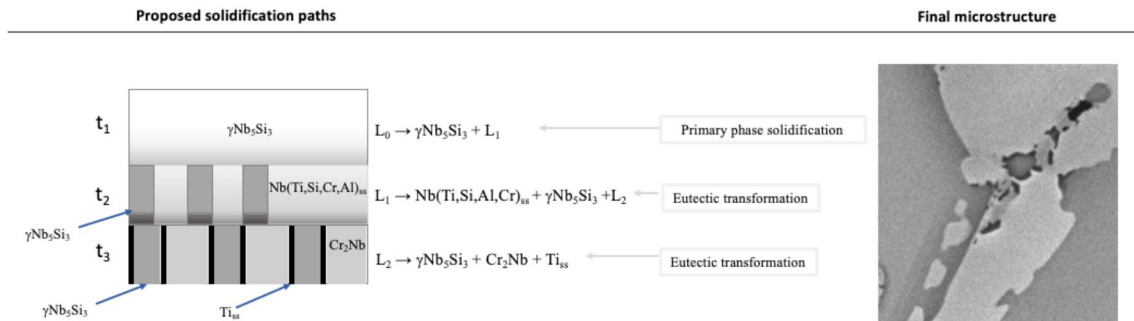
Figure 68 - Solidification path put forward following the formation of the primary γNb_5Si_3 and the anomalous binary eutectic on the top layer processed with the NbTiSiAlCrZr powder mixture.
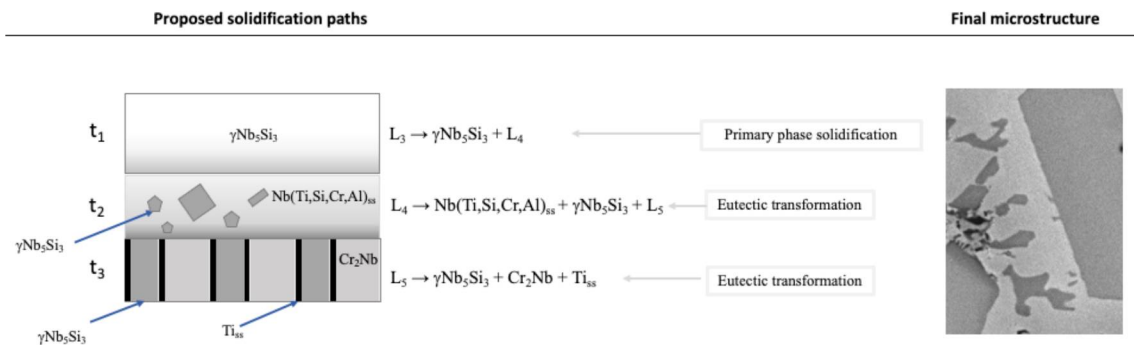
2) The primary γNb_5Si_3 might also solidify in regions with low Al content. Under these conditions, the solidification of the binary $Nb(Ti,Si,Al,Cr)_{ss}/\gamma Nb_5Si_3$ eutectic is suppressed. The $Nb(Ti,Si,Al,Cr)_{ss}$ is solidified from the remaining liquid, segregating Si to the solidification front. Finally, the ternary eutectic $\gamma Nb_5Si_3 /Cr_2Nb/Ti_{ss}$ is solidified from the remaining liquid rich in Si, Ti and Cr. The final microstructure resulted from this solidification path is represented in Figure 69 that includes a cutout from the top layer microstructure, Figure 65 (b).

Figure 69 – Alternative solidification path put forward following the formation of the primary γNb_5Si_3 on the layer processed with the NbTiSiAlCrZr powder mixture.
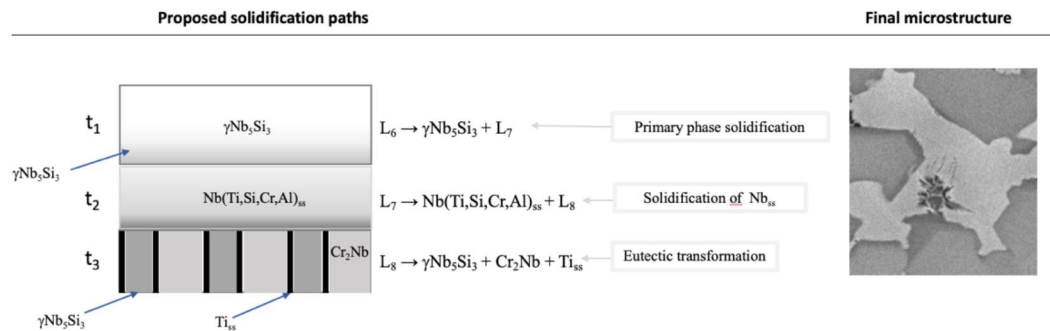
Analysis from the microstructure of the bottom layer, exposed to the remelting and reheating thermal cycles, shows that thermal cycles modified both the phase distribution and phase composition, Figure 70 (b). As mentioned for the multilayer processed with the NbTiSiAlZr powder mixture, the lower thermal gradient during the remelting thermal cycle allowed the overgrowth of the γNb_5Si_3 silicides at the expense of eutectic phases. The solidification of the Al-rich βNb_5Si_3 silicide can also be observed in higher magnification, Figure 71.

Figure 70 - Microstructure from the top layer (as-deposited) (a) and the second deposited layer (two thermal cycles) (b) of the NbTiSiAlCrZr multilayer.
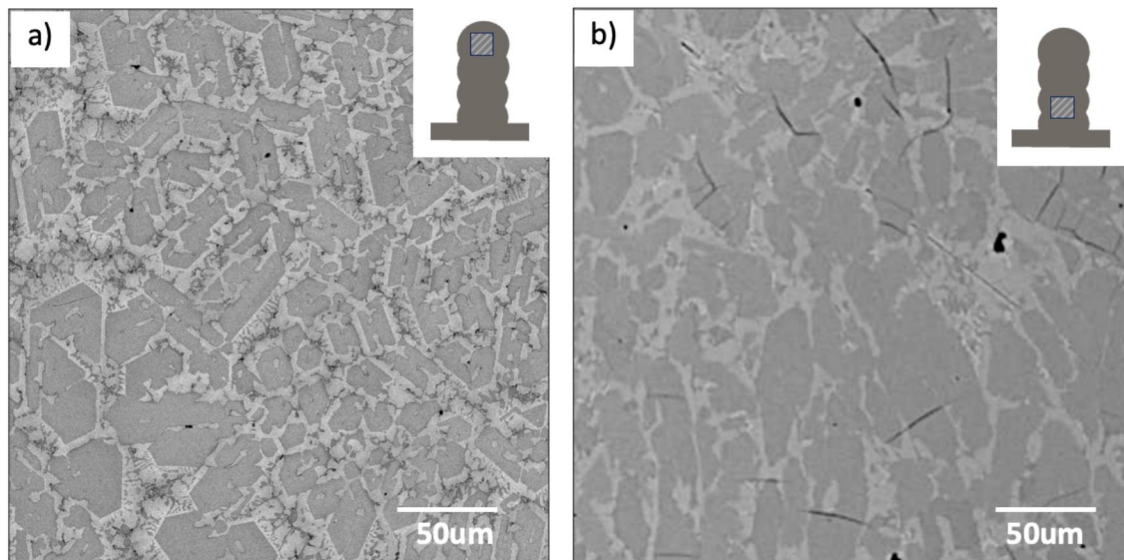
Figure 71 - Microstructure at the bottom in higher magnification.
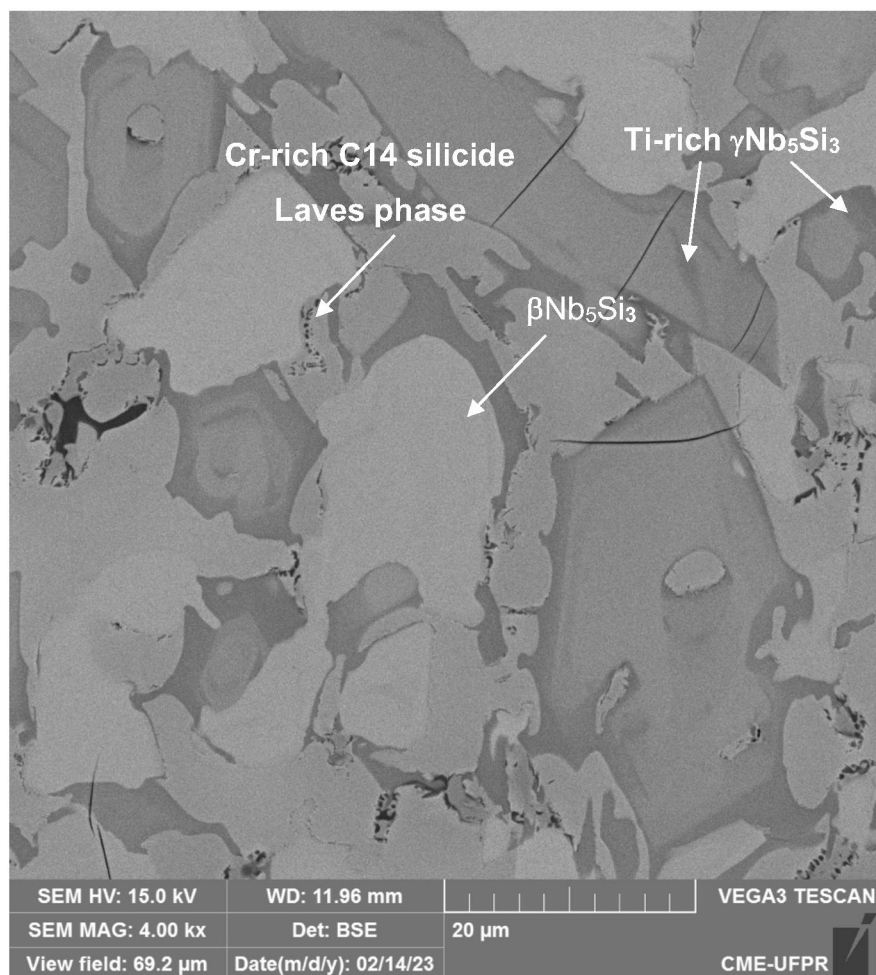
Segregations suggest that the reheating cycle drove the diffusion of Ti to the γNb_5Si_3 silicide boundaries and also lead to the precipitation of the Cr-rich silicide Laves phase in the grain boundaries of the $Nb(Ti,Al,Cr)_{ss}$. EDS composition maps confirm the precipitation of the Cr/Si rich phase at the $Nb(Ti,Al,Cr)_{ss}$ boundaries, Figure 72.

Figure 72 – EDS composition map showing the precipitation of the Cr/Si rich phase at the $Nb(Ti,Al,Cr)_{ss}$ boundaries.
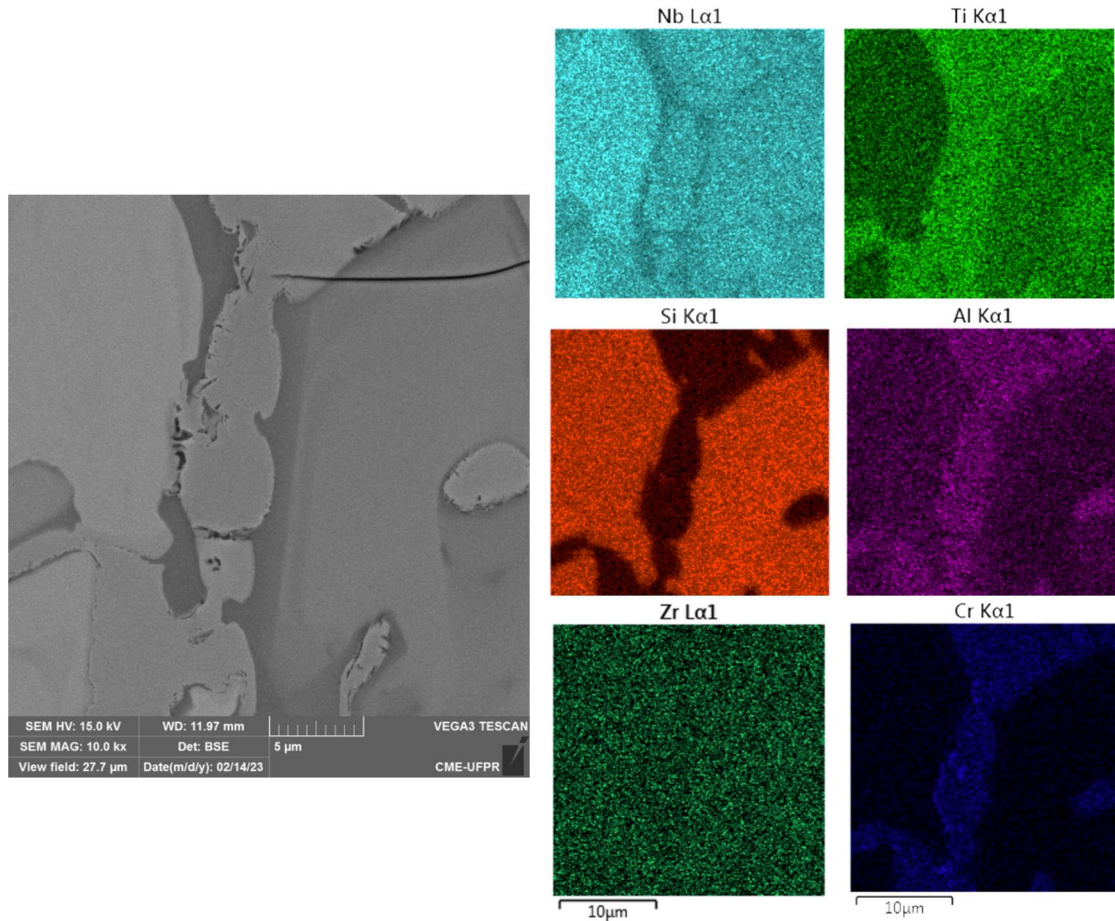
Together with Al, Cr is reported to considerably improve the oxidation resistance without severe embrittlement of the Nb_{ss} when their concentration is 2~8at%Cr and 2~6at%Al (ZELENITSAS, 2005). Furthermore, the formation of the Cr_2Nb phase is reported to form the protective $CrNbO_4$ oxide layer at high temperatures. However, the addition of Cr to the powder mixture resulted in a multilayer with lower oxidation resistance compared to the NbTiSiAlZr multilayer, Figure 73. Although the addition of Cr suppressed the solidification of eutectics containing Nb_{ss} , it stabilized a continuous and homogeneous Nb_{ss} matrix around the γNb_5Si_3 silicides. The oxygen diffusion in Nb_{ss} is higher than in silicides and the increase in its volume fraction compromise the oxidation resistance .

Figure 73 - TGA analysis of multilayers processed with the NbTiSiAlZr and the NbTiSiAlCrZr powder mixture.
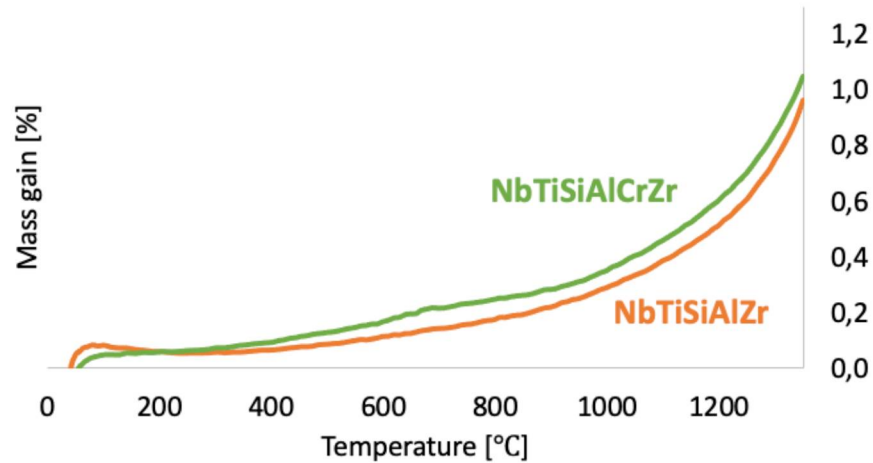
4.8.   Nb24Ti18Si5Al5Cr2Mo+1Zr

The addition of Mo did not change the hardness of multilayers (887 $\pm$ 90 HV), but induced some dispersion that are followed by main differences in the microstructure. XRD annalysis reveal the synthesis of the Nb_{ss} phase, the γNb_5Si_3 silicide, and the Cr_2Nb Laves phase, Figure 74. The microstructure from the top layer, Figure 75, confirm the solidification of the γNb_5Si_3 silicide, the $Nb(Ti,Al,Cr,Mo)_{ss}$ and a three-phase eutectic containing $Cr_2Nb/\gamma Nb_5Si_3/Ti_{ss}$. The phase composition was assessed by EDS, Table 12.

Figure 74 - XRD from the top of the NbTiSiAlCrMoZr multilayer.
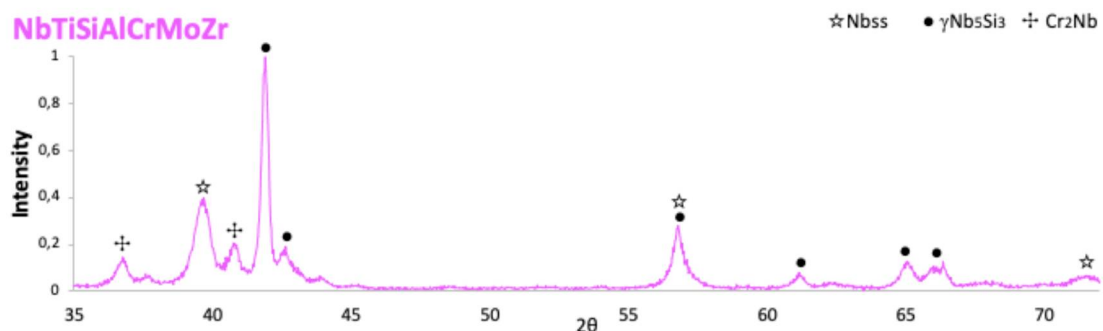
Figure 75 - Microstructure at the top layer (a) general view (b) details of the microstructure.
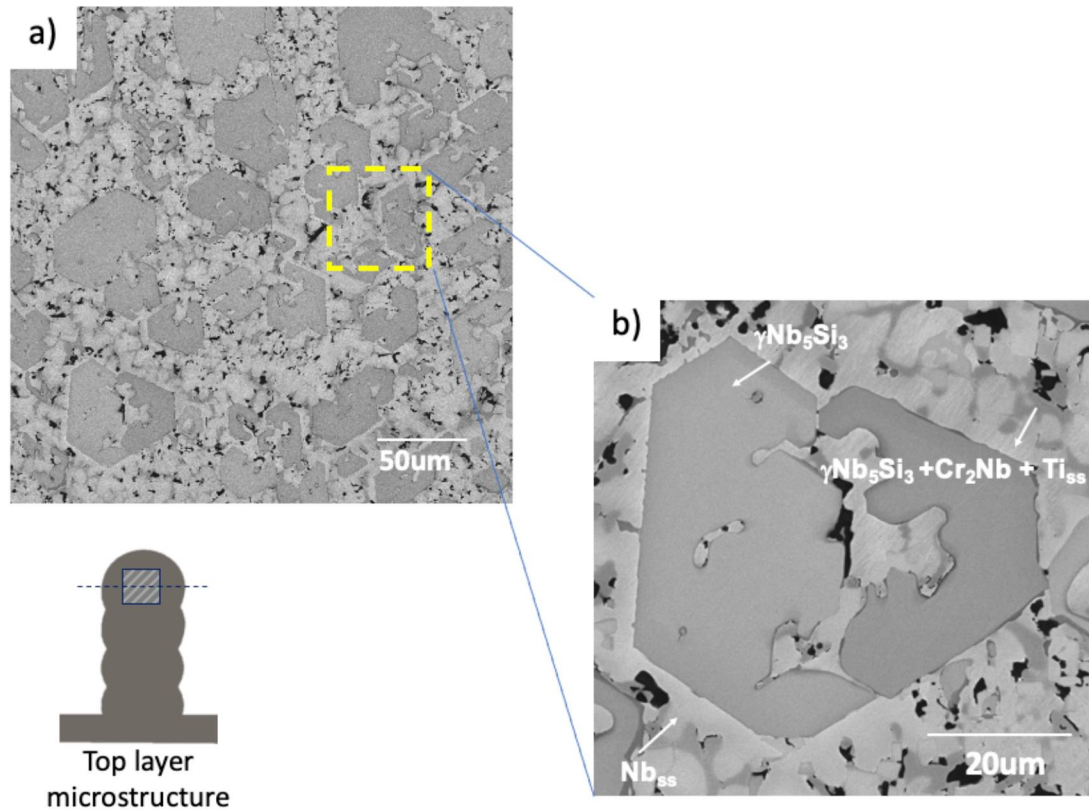
Table 12 -Average phase composition observed in the top layer processed with the NbTiSiAlCrMoZr powder mixture.

Alloy		Phase	Composition (at%)				
			Nb	Si	Ti	Al	Cr
		γNb_5Si_3	37,4	33,2	24,8	2,9	1,3
		Nb_{ss}	44,1	1,4	34,3	10,3	9,8
Nb24Ti18Si5Al5Cr2Mo + 1Zr		Cr_2Nb	29,6	7,9	20,8	6,4	35,3
	eutectic	γNb_5Si_3	24,4	30,6	36,2	5,8	2,1
		Ti_{ss}	6,8	0,6	89,4	1,3	1,8

EDS composition maps, Figure 76, confirm the segregation of Ti and Cr to the terminal three phase eutectic. Molybdenum is substituting Nb both in the solid

solution and in the silicides, together with Ti, stabilizing the high temperature phases.

Figure 76 - EDS composition maps of the ternary eutectic in the as-deposited microstructure of NbTiSiAlCrMoZr multilayers.
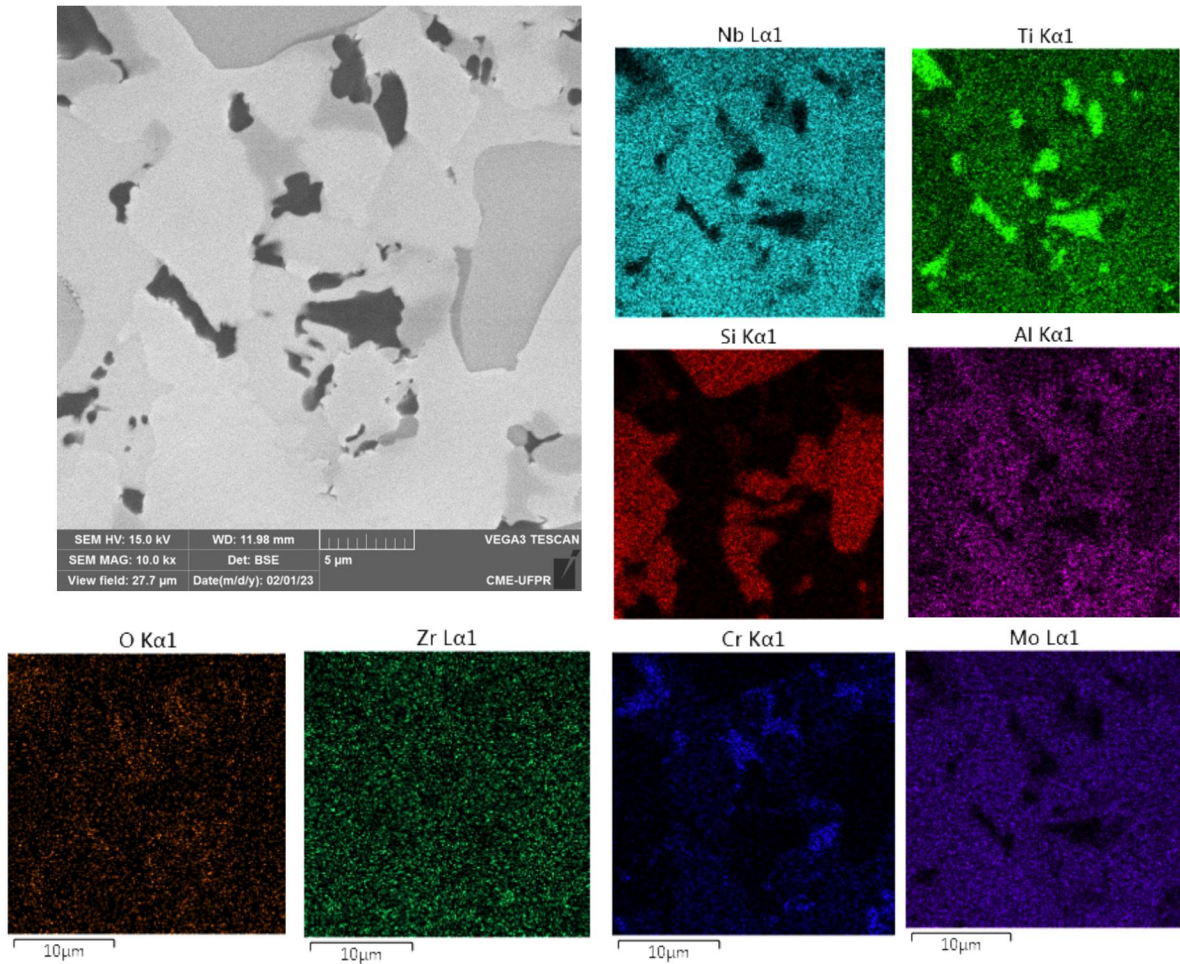
Considering the experimental results, the melting point, and the typical solubility of elements in each phase, as with the other powder mixtures solidification paths for the as-deposited microstructure are put forward. The primary γNb_5Si_3 is stabilized by Ti and Zr and solidifies at higher temperatures. The proposed solidification path is schematically represented in Figure 77 and is described as follows:

1) The high temperature γNb_5Si_3 silicide grows from the liquid rich in Zr and Ti following the solidification reaction $L_0 \rightarrow \gamma Nb_5Si_3 + L_1$. During the

solidification, the remain liquid is enriched in Ti, Cr, Al and Mo inducing the formation of a Nb_{ss} surrounding the silicide following the transformation $L_1 \rightarrow Nb(Ti,Cr,Al,Mo)_{ss} + L_2$. Solidification ends with the three-phase eutectic containing $\gamma Nb_5Si_3/Cr_2Nb/Ti_{ss}$. The final microstructure resulting from this solidification path is represented in Figure 77 that includes a cutout from the top layer microstructure, Figure 75 (b).

Figure 77 - Solidification path put forward following the formation of the primary γNB_5SI_3 on the top layer processed with the NbTiSiAlCrMoZr powder mixture.
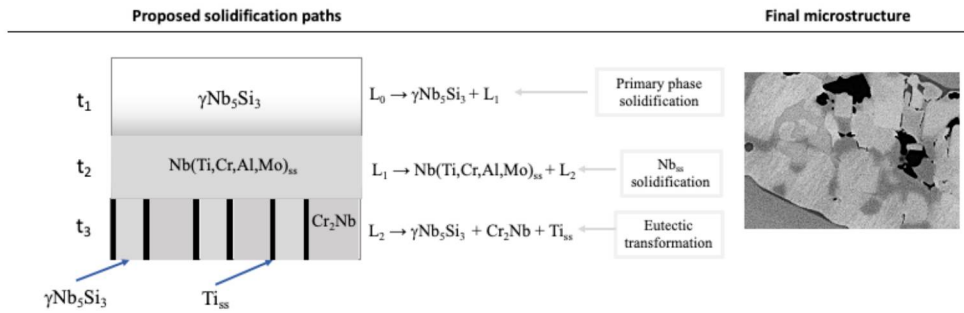
The multiple thermal cycles again impacted phase distribution of the bottom layer, Figure 78 (b). As with the multilayers processed with previous powder mixtures, remelting resulted in overgrown faceted silicides developed due to the lower thermal gradients. It happens at the expense of the fine distributed three-phase eutectic once present in the as-deposited condition, Figure 78 (a).

Furthermore, a detailed analysis at the microstructure reveals the formation of a new phase after remelting, Figure 79. This is a consequence of the off-equilibrium solidification that under further heating can minimize the energy of the system forming other phases. EDS analysis shows the composition of this phase to be 43Nb − 30,6Si − 19,8Ti − 4,8Al − 1,8Cr. Similar composition is reported by LI, Yunlong et al. (2020) and is associated to the βNb_5Si_3 silicide. Formation of new phases after the remelting cycle suggest that the solidification paths were changed driven mainly by the different heat flow condition of that layer at that time.

Figure 78 - Microstructure from the top layer (as-deposited) (a) and the second
deposited layer (two thermal cycles) (b) of the NbTiSiAlCrMoZr multilayer.
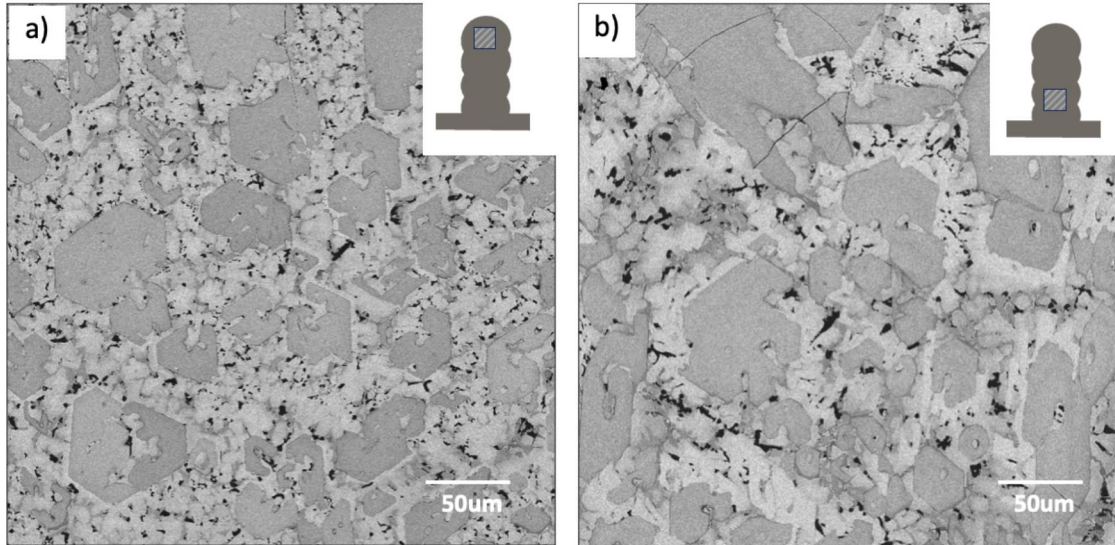
Although both remelting and reheating thermal cycles, contribute to the decrease of cooling rate in these first deposited layers, the remelting cycle was determinant to allow the solidification of the overgrowth silicides. After remelting, the further reheating thermal cycles might account for solid state transformations such as the precipitation of different phases and segregations, which can be observed at the bottom layer in higher magnifications, Figure 79.

Dark gray regions can be observed close to the γNb_5Si_3 and Nb_{ss} boundaries, as indicate Figure 8079. It suggests that the reheating thermal cycle lead to Ti diffusion and segregation close to the grain boundaries of the saturated phases.

Despite the changes in phase distribution and the formation of the β- type silicide, the composition of the primary γNb_5Si_3 remains almost stable even after two thermal cycles. EDS analysis shows the composition 37,8Nb – 33,4Si – 24,3Ti – 2,6Al – 1,4Cr – 0,4Zr in the as-deposited layer and the composition 36,7Nb – 34,2Si – 25Ti – 2,4Al – 1,3Cr – 0,4Zr in the layer exposed to two thermal cycles.

Alloying with Mo is reported to decrease the oxygen solubility in the Nb_{ss}, because of its high electron/atom ratio (>5.8) (SALA; KASHYAP; MITRA, 2021). However, temperature exposure up to 1350°C reveal the addition of Mo lead to a

further decrease in oxidation resistance at temperatures higher than ~500°C, Figure 80. This oxidation behavior might also be related to the solidification of the continuous Nb_{ss} distributed around the silicides and eutectic phase.

Figure 79 - Microstructure at the second deposited layer in higher magnification.
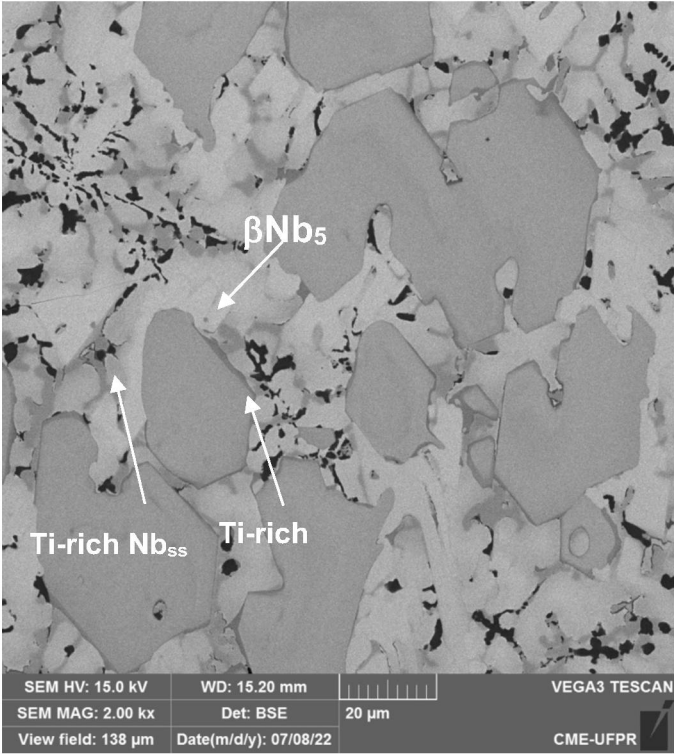
Figure 80 – TGA analysis of multilayers processed with the NbTiSiAlCrZr and the NbTiSiAlCrMoZr powder mixture.
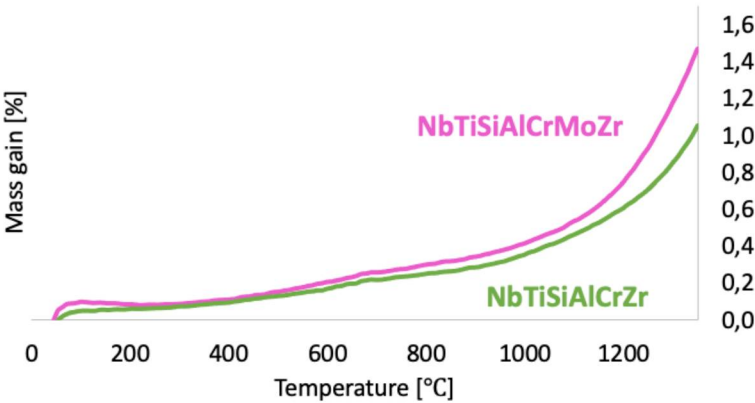
4.9. CONTRIBUTIONS TO THE UNDERSTANDING OF Nb SILICIDES

Nb silicides processed during the deposition of powder mixture required moderate solidification rates of PTA processing to allow for the synthesis to occur. Not even the large number of thermal cycles associated with LPBF allow for the complete syntheses of silicides

Solidification of the deposited powder mixtures starts with the formation of primary phases Nb_5Si_3 and Nb_{ss}. Changes in the composition of these phases occur depending on the powder mixture. Solidification paths induced by each of the primary phases occurs simultaneously.

The presence of Al and Cr in the powder mixture, individually or together, induces more segregation during solidification leading to the formation of anomalous and ternary eutectic. The addition of Mo to the powder mixture stabilizes the high temperature primary phases and mitigates the solidification of the anomalous eutectic.

Compared to the as-deposited condition, the remelting of previous layers resulted in the solidification of different phases for the multilayers processed with Cr and Mo addition. Thermal cycles induced coarse and overgrown silicides due to heat accumulation by the multiple processing cycles. The overgrown silicides cannot accommodate thermal stresses, consequence of different coefficient of thermal expansion of adjacent phases, allowing for cracks to nucleate and propagate, perpendicularly to the growth direction (higher heat flow). However, high tough phases surrounding the silicides confine cracks within the silicides.

The off-equilibrium solidification structure allows for segregation to occur during reheating thermal cycle resulting Ti segregation in the γNb_5Si_3 silicide. Depending on the composition of the powder mixtures other phases precipitate during reheating.

The average hardness of multilayers increased with the addition of Si to the powder mixture, Table 13, associated with the formation of the hard Nb silicides. However, considering the high deviation in hardness value, the hardness remains the same even with further element additions to the powder mixture.

Table 13 – Average hardness of the multilayers.

Multilayer	Hardness [HV]
Nb24Ti + 1Zr	392 ± 46
Nb24Ti18Si + 1Zr	864 ± 54
Nb24Ti18Si5Al + 1Zr	840 ± 36
Nb24Ti18Si5Al5Cr + 1Zr	869 ± 34
Nb24Ti18Si5Al5Cr2Mo + 1Zr	887 ± 90

The oxidation resistance improved considerably with Al addition to the powder mixture, compared to the first analyzed solid solution multilayer built with the NbTiZr powder mixture, Figure 81. The Al addition induced the formation of multiple eutectics and the Nb_{ss} is only solidified as a eutectic phase. However, the addition of Cr and Mo reduced the volume fraction of solidified eutectics, leading to a progressive increase in a continuous Nb_{ss} matrix. The higher vulnerability of the Nb_{ss} to high temperature oxidation resulted in a decrease in oxidation resistance after Cr and Mo addition.

Figure 81 - Mass loss of multilayers built with all powder mixtures only with PTA gas protection.
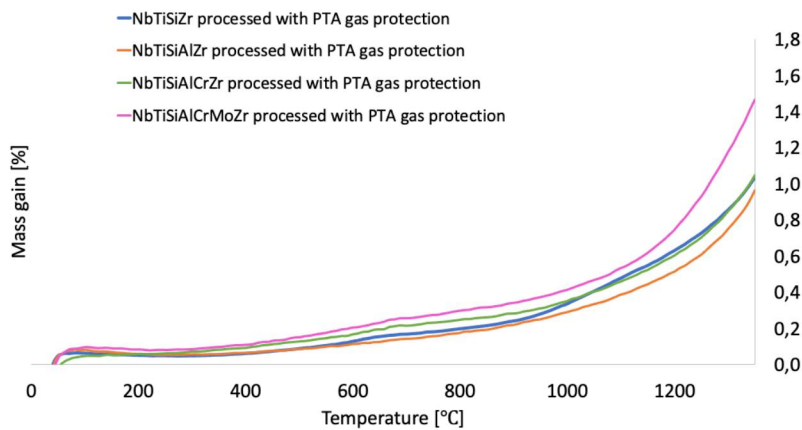
4.10. PROCESSING IN ARGON ATMOSPHERE

Processing Nb-based elemental powder mixtures, using standard deposition procedures available in industrial set up, has shown that it is possible to build silicide multilayer walls. However, the high affinity of Nb with oxygen requires an assessment of the impact of the processing environment on the processed multilayers. For that purpose, this chapter discusses the impact of and argon environment to perform the *in-situ* synthesis during the deposition of elemental powder mixtures in addition to the argon protection offered by the deposition equipment that includes plasma gas, feeding gas and protection gas.

Processing pure Nb with LPBF showed that even the use of an inert atmosphere does not avoid oxygen to be trapped in the microstructure. Adding alloying elements with higher affinity with oxygen can reduce oxygen content in microstructure.

Processing the solid solution NbTiZr powder mixture with PTA-DED inside the inert chamber, with oxygen levels lower than 100ppm, did not eliminate the segregation of the Nb particles between layers, suggesting that it might be a consequence of oxygen in powders.

It is timid the improvement on oxidation resistance gained when processing the solid solution multilayer NbTiZr in inert chamber, as show Figure 82. Only at temperatures higher than 1000°C is observed a difference in mass gain between multilayers processed with and without an inert chamber. Beyond this temperature, the solid solution multilayer processed in inert chamber shows a slightly reduction in the oxidation rate, suggesting that processing in inert atmosphere reduced the oxygen trapped in microstructure, and therefore the oxygen reservoir for oxidation processes.

Figure 83 shows the mass gain of Nb-Si multilayers built inside the inert chamber, whereas Figure 84 summarizes the mass gain for Nb-Si multilayers built only with the PTA gas protection. None of the multilayers processed inside the inert chamber show higher oxidation resistance compared to the NbTiSiAlZr multilayer built only with PTA gas protection (less than 1% mass loss). It suggests that, for the compositions tested and parameters used in this study, the PTA gas

protection might be as effective as an inert atmosphere on mitigating the oxygen solubility in melting pool.

Figure 82 - Mass gain for multilayers built with the solid solution NbTiZr elemental powder mixture.
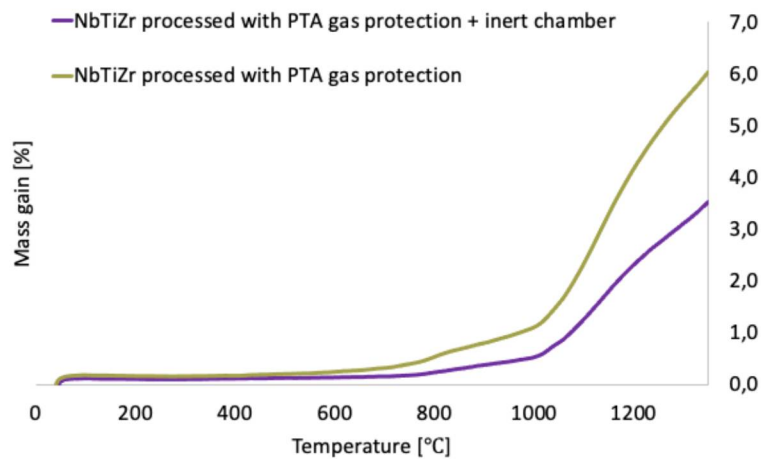
Figure 83 - Mass gain for multilayers built with the PTA gas protection and inside the inert chamber.
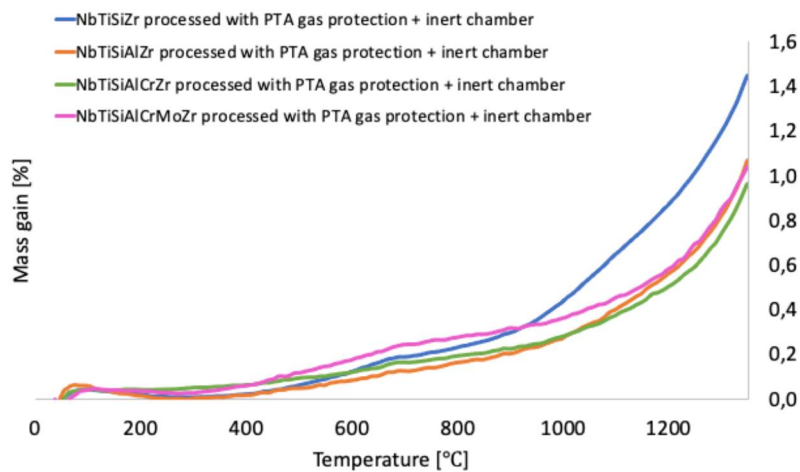
Figure 84 - Mass gain for multilayers built only with the PTA gas protection.
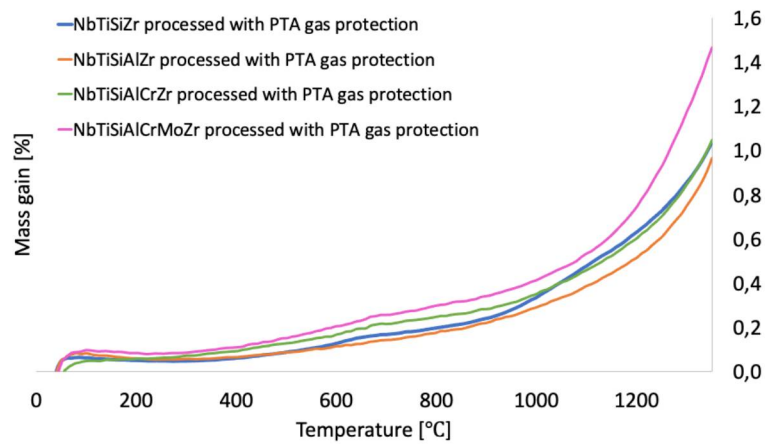
Although no relevant change in mass gain was measured between multilayers processed with and without a inert chamber, small changes in the microstructure are observed. Comparing solidification structures of multilayers processed in both conditions, Figure 85, it is possible to observe phases with the same morphology pattern, but varying slightly in volume fraction. For the multilayers processed in argon chamber, coarser silicides solidify, suggesting a lower cooling rate inside the inert chamber due to the intense heat accumulated into the smaller environment.

Figure 85 –Image from the top layer of multilayers built only with PTA gas protection and multilayers built inside inert chamber.
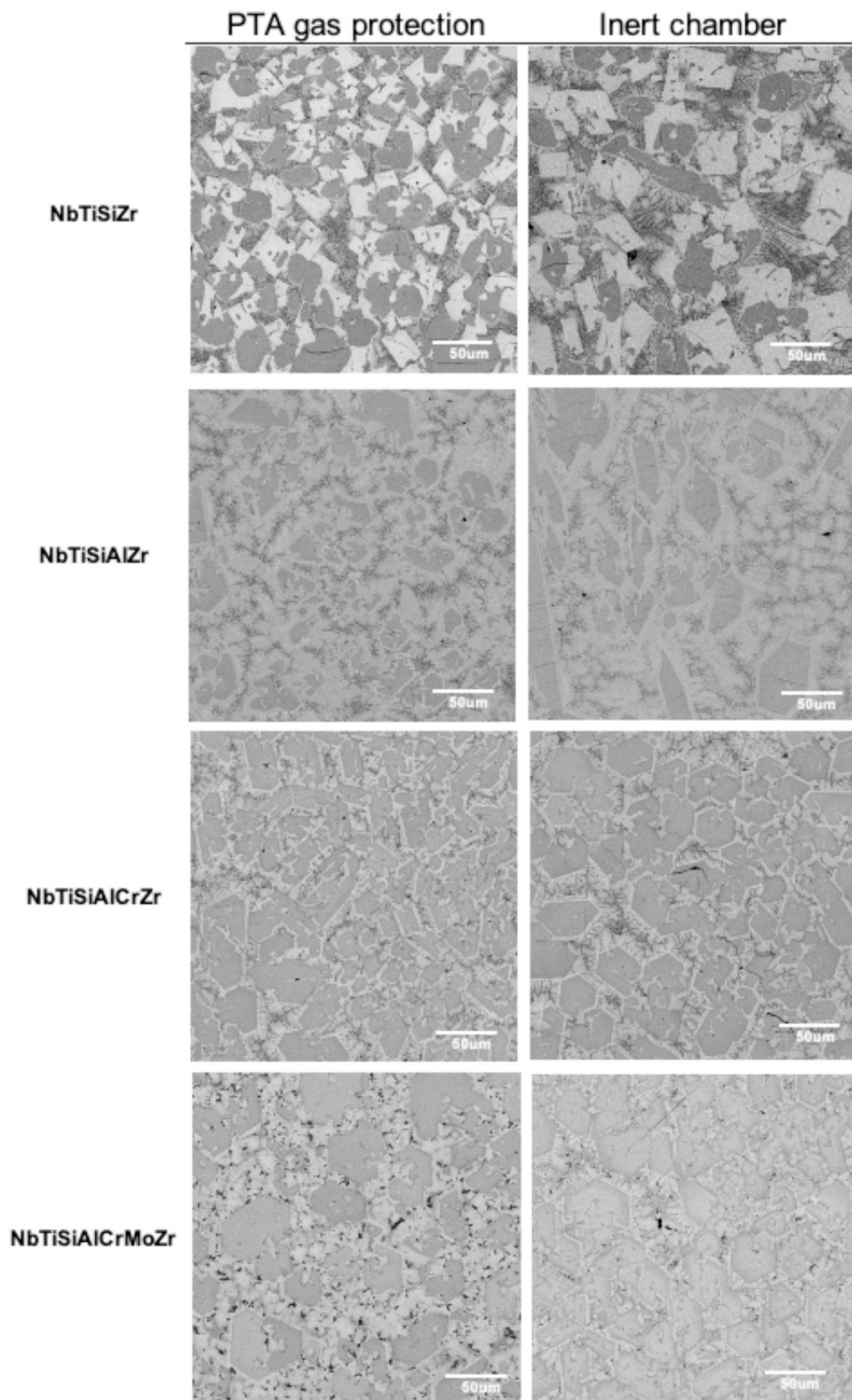
Table 14 shows that, considering the deviation, there is no difference between the average hardness of multilayers processed in both conditions.

Table 14 - Hardness of multilayers processed only with PTA gas protection and multilayers processed with inert chamber

Multilayer	Hardness [HV]					
	PTA gas protection			Inert chamber		
Nb24Ti + 1Zr	392	±	46	380	±	47
Nb24Ti18Si + 1Zr	864	±	54	860	±	47
Nb24Ti18Si5Al + 1Zr	840	±	36	852	±	48
Nb24Ti18Si5Al5Cr + 1Zr	869	±	34	880	±	66
Nb24Ti18Si5Al5Cr2Mo + 1Zr	887	±	90	814	±	71

Considering the data accessed from the samples processed with LPBF and PTA-DED, the in-situ synthesis of Niobium silicides requires lower cooling rates than that usually offered by LPBF processes. Furthermore, the presence and extent of the solid solution in the microstructure has a decisive influence on the oxidation resistance. The powder mixture complexity did not interfere directly in the complexity of the microstructure, solidification paths or stability to thermal cycles. Furthermore, processing into an argon atmosphere shows great influence in oxidation resistance of the single-phase solid solution microstructures. But when silicides are synthesized, this influence is not observed anymore.

5. CONCLUSIONS

Multilayers of elemental Nb powder were successfully built by LPBF with densification higher than 99%. It was revealed that, although processing was carried out in an inert chamber oxygen pick-up occurs and increases with the energy density used. The oxygen pick-up impacts performance because it increases Nb hardness and decrease the oxidation resistance.

A LPBF processing window for the Nb+WC powder mixture was also successfully obtained. The addition of WC reduces the oxygen trapped in builds and, consequently, slows down the oxidation rate of the material.The reduction in hardness of these builds is a consequence of the less significant strengthening of substitutional W and the removal of the interstitial oxygen in solid solution.

The LPBF *"in-situ"* synthesis of the Nb47Si10Al powder mixture, was not successful. *In-situ* synthesis was compromised by the fast solification rate indicating that low temperature gradients are required to successfully induce *in-situ* synthesis of Nb silicides.

In order to achieve lower thermal gradients, the PTA-DED process was chosen to investigate the build of multilayers performing *in-situ* synthesis of Nb-based alloys during the deposition of elemental powder mixtures. The investigation started by the NbTiZr powder mixture and evolved progressively to complex alloy compositions with further addition of Si, Al, Cr and Mo elemental powders.

The presence of Al and Cr in the powder mixture, individually or together, induces more segregation during solidification leading to the formation of anomalous and ternary eutectics. The addition of Mo to the powder mixture stabilizes the high temperature primary phases and mitigates the solidification of the anomalous eutectic.

Multiple thermal cycles lead to a decrease in thermal gradient, resulting in coarse microstructures with overgrown silicides that became more vulnerable to the thermal stresses caused by the different coefficient of thermal expansion between phases.

The reheating thermal cycle resulted in precipitation of new phases in multilayers processed with Al and Cr. For all multilayers the reheating leads to

segregation of the Ti solute mainly inside and at the boundaries of the γNb_5Si_3 silicide.

The powder mixture complexity did not interfere directly in the complexity of the microstructure, solidification paths or stability to thermal cycles. The addition of Si in the NbTiZr powder mixture eliminated Nb segregations and improved considerably the oxidation resistance. The main positive impact in oxidation resistance is offered by the solidification of silicides. The addition of Al resulted in a timid oxidation improve, whereas other alloying elements tested, Cr and Mo, did not reveal a further improve in oxidation resistance. Results suggest that the Nb_{ss} solidified as a large continuous matrix, outlining the primary silicides, can compromise oxidation resistance. Better oxidation resistance might be achieved when the Nb_{ss} solidifies as an eutectic phase, together with Nb silicides.

PTA-DED multilayers Nb based powder mixtures do not require extreme controlled of oxygen content during processing, suggesting that, for the materials and parameters used in this study, the PTA gas protection might be as effective as an inert atmosphere on mitigating the oxygen solubility in melting pool.

6. FUTURE WORK

As future work it is necessary to investigate Nb-Si pre-alloyed powders to understand the role of elemental powders in promoting segregations in the melting pool. Elemental powder also requires a higher energy density to perform both the melting of powders and the synthesis of the silicides. Processing pre-alloyed powders may also reduce the energy density demanded to deposit the multilayers. It will allow to achieve a lower cooling rate to solidify a refined microstructure, reported to improve the oxidation resistance of these alloys.

The overgrown silicides caused by thermal cycles during remelting impairs the microstructure due to crack nucleation and propagation inside the overgrown silicide. Further studies might be done to understand how to avoid the formation of these silicides along multilayers.

Further studies are also important to investigate the effect of homogenization heat treatment in multilayer microstructures.

REFERENCES

ABOULKHAIR, Nesma T.; EVERITT, Nicola M.; ASHCROFT, Ian; TUCK, Chris. Reducing porosity in AlSi10Mg parts processed by selective laser melting. **Additive Manufacturing**, vol. 1, p. 77–86, 2014. https://doi.org/10.1016/j.addma.2014.08.001.

ABREU, Heber O. C.; BUENO, Bruno P.; D'OLIVEIRA, Ana Sofia C.M. In situ processing aluminide coatings with and without tungsten carbide. **International Journal of Advanced Manufacturing Technology**, vol. 119, n° 1–2, p. 477–488, 1 mar. 2022. https://doi.org/10.1007/s00170-021-08032-z.

ALI, Haider; GHADBEIGI, Hassan; MUMTAZ, Kamran. Effect of scanning strategies on residual stress and mechanical properties of Selective Laser Melted Ti6Al4V. **Materials Science and Engineering A**, vol. 712, n° October 2017, p. 175–187, 2018. https://doi.org/10.1016/j.msea.2017.11.103.

ALLEN, A.; DOUGLAS, A. C.; FEITOSA, L. M.; QIAN, H.; LI, J.; DONG, H. B.; LIN, X.; LI, Y. Solidification of niobium-silicide-based alloys during laser additive manufacturing process. 529., 17 jun. 2019. **IOP Conference Series: Materials Science and Engineering** [...]. [*S. l.*]: Institute of Physics Publishing, 17 jun. 2019. vol. 529, . https://doi.org/10.1088/1757-899X/529/1/012006.

ALLEN, Adam John Sam. **Phase Stabilisation of Nb-Si-Ti Alloys via Elemental Additions and Post-Processing**. 2019. University of Leicester, United Kingdom, 2019.

ALMEIDA, V. B.; TAKANO, E. H.; MAZZARO, I.; D'OLIVEIRA, A. S.C.M. Evaluation of Ni-Al coatings processed by plasma transferred arc. **Surface Engineering**, vol. 27, n° 4, p. 266–271, 2011. https://doi.org/10.1179/026708410X12550773057866.

AMERICAN ROLLER COMPANY. https://americanroller.com/. 2015.

ARRAVIND, R.; VAIRAMUTHU, J.; STALIN, B.; SHANMUGAM, S.; BALAJI, R.; DHINAKARAN, V. Wear experimentation on Tantalum carbide-based Niobium MMC. 988., 15 dez. 2020. **IOP Conference Series: Materials Science and Engineering** [...]. [*S. l.*]: IOP Publishing Ltd, 15 dez. 2020. vol. 988, . https://doi.org/10.1088/1757-899X/988/1/012129.

ASM HANDBOOK COMMITTEE. **Powder Metal Technologies and Applications**. [*S. l.*]: ASM International, 1998. vol. 7.

BACH, D. EELS Investigations of Stoichiometric Niobium Oxides and Niobium-based Capacitors. **Thesis**, , p. 204, 2009.

BALSONE, S. J.; BEWLAY, B. P.; JACKSON, M. R.; SUBRAMANIAN, P. R.; ZHAO, J. C.; CHATTERJEE, A.; HEFFERNAN, T. M. Materials beyond

superalloys-exploiting high-temperature composites. **Proceedings of the International Symposium on Structural Intermetallics**, n° December 2015, p. 99–108, 2001.

BARRETT, Charles A.; COREY, James L. Oxidation Behavior of Binary Niobium Alloys. n° November, 1960.

BEDFORD, R. E.; BONNIER, G.; MAAS, H.; PAVESE, F. Recommended values of temperature on the International Temperature Scale of 1990 for a selected set of secondary reference points. **Metrologia**, vol. 33, n° 2, p. 133–154, 1996. https://doi.org/10.1088/0026-1394/33/2/3.

BEWLAY, B P; JACKSON, M R; ZHAO, J.-C; SUBRAMANIAN, P R. **A Review of Very-High-Temperature Nb-Silicide Based Composites**. [*S. l.: s. n.*], 2003. BEWLAY, B P; JACKSON, M R; ZHAO, J.-C; SUBRAMANIAN, P R; MENDIRATTA, M G; LEWANDOWSKI, J J. **Ultrahigh-Temperature Nb-Silicide-Based Composites**. [*S. l.: s. n.*], 2003. Disponível em: www.mrs.org/publications/bulletin.

BOND, Danielle; D'OLIVEIRA, Ana Sofia Clímaco Monteiro. Effect of current and atomized grain size distribution on the solidification of Plasma Transferred Arc coatings. **Materials Research**, vol. 15, n° 5, p. 770–774, 2012. https://doi.org/10.1590/S1516-14392012005000101.

BOULOS, Maher I; FAUCHAIS, Pierre; PFENDER, Emil. **Plasma Torches for Cutting, Welding and PTA Coating BT - Handbook of Thermal Plasmas**. Cham: Springer International Publishing, 2017. https://doi.org/10.1007/978-3-319-12183-3_47-1.

BRAUN, J.; KASERER, L.; STAJKOVIC, J.; LEITZ, K. H.; TABERNIG, B.; SINGER, P.; LEIBENGUTH, P.; GSPAN, C.; KESTLER, H.; LEICHTFRIED, G. Molybdenum and tungsten manufactured by selective laser melting: Analysis of defect structure and solidification mechanisms. **International Journal of Refractory Metals and Hard Materials**, vol. 84, 1 nov. 2019. https://doi.org/10.1016/j.ijrmhm.2019.104999.

CANGUE, Feliciano José Ricardo; D'OLIVEIRA, Ana Sofia Clímaco Monteiro. Influence of Al on the microstructure and carburization performance of a N-based alloy coating. **Materials Chemistry and Physics**, vol. 120, n° 2–3, p. 552–557, 2010. https://doi.org/10.1016/j.matchemphys.2009.11.046.

CARDOZO, Eloisa Pereira; D'OLIVEIRA, Ana Sofia C.M. Niobium Silicide Multilayers Processed by In Situ Synthesis During Deposition of Powder Mixtures. **Journal of Materials Engineering and Performance**, vol. 31, n° 5, p. 3998–4005, 1 maio 2022. https://doi.org/10.1007/s11665-021-06460-2.

CHAUDHARY, Shishir; SANKAR, M.; PRASAD, V. V.Satya; BALIGIDAD, R. G.; GOKHALE, A. A. Effect of tungsten and zirconium on structure and properties of niobium. **High Temperature Materials and Processes**, vol. 37, n° 8, p. 749–759, 28 ago. 2018. https://doi.org/10.1515/htmp-2016-0227.

CHAWLA, Nikhilesh; CHAWLA, Krishan K. **Metal Matrix Composites**. 1° ed. [*S. l.*]: Springer, 2006. vol. 1.

CHENG, Bo; SHRESTHA, Subin; CHOU, Kevin. Stress and deformation evaluations of scanning strategy effect in selective laser melting. **Additive Manufacturing**, vol. 12, p. 240–251, 1 out. 2016. https://doi.org/10.1016/j.addma.2016.05.007.

CHUNG, Dong-seok; ENOKI, Manabu; KISHI, Teruo. Microstructural analysis and mechanical properties of in situ Nb / Nb-aluminide layered materials. **Science and Technology of Advanced Materials**, , p. 129–135, 2002.

DEBROY, T.; WEI, H. L.; ZUBACK, J. S.; MUKHERJEE, T.; ELMER, J. W.; MILEWSKI, J. O.; BEESE, A. M.; WILSON-HEID, A.; DE, A.; ZHANG, W. Additive manufacturing of metallic components – Process, structure and properties. **Progress in Materials Science**, vol. 92, p. 112–224, 1 mar. 2018. https://doi.org/10.1016/j.pmatsci.2017.10.001.

DILIP, J. J.S.; ZHANG, Shanshan; TENG, Chong; ZENG, Kai; ROBINSON, Chris; PAL, Deepankar; STUCKER, Brent. Influence of processing parameters on the evolution of melt pool, porosity, and microstructures in Ti-6Al-4V alloy parts fabricated by selective laser melting. **Progress in Additive Manufacturing**, vol. 2, n° 3, p. 157–167, 1 set. 2017. https://doi.org/10.1007/s40964-017-0030-2.

DINDA, G. P.; DASGUPTA, A. K.; MAZUMDER, J. Laser aided direct metal deposition of Inconel 625 superalloy: Microstructural evolution and thermal stability. **Materials Science and Engineering A**, vol. 509, n° 1–2, p. 98–104, 25 maio 2009. https://doi.org/10.1016/j.msea.2009.01.009.

DYMEK, S.; DOLLA, A; DOLLÁR, A.; DYMEK, S.; DOLLA, A. Microstructure and high temperature mechanical properties of mechanically alloyed Nb3Al-based materials. **Intermetallics**, vol. 11, n° 4, p. 341–349, 2003. https://doi.org/10.1016/S0966-9795(03)00002-5.

FAIDEL, D.; JONAS, D.; NATOUR, G.; BEHR, W. Investigation of the selective laser melting process with molybdenum powder. **Additive Manufacturing**, vol. 8, p. 88–94, 1 out. 2015. https://doi.org/10.1016/j.addma.2015.09.002.

FANG, Xin; GUO, Xiping; QIAO, Yanqiang. Effect of Ti addition on microstructure and crystalline orientations of directionally solidified Nb–Si based alloys. **Intermetallics**, vol. 122, 1 jul. 2020. https://doi.org/10.1016/j.intermet.2020.106798.

FEITOSA, Leandro Moraes. **Solidification Behaviour and Microstructure Evolution of Refractory Metals-Based Alloys Under Rapid Solidification**. [*S. l.: s. n.*], 2018.

FITZPATRICK, M.E; FRY, A.T.; HOLDWAY, P.; KANDIL, F.A.; SHACKLETON, J.; SUOMINEN, L. **Determination of Residual Stresses by X-ray Diffraction**. 52° ed. United Kingdon: National Physical Laboratory, 2005. vol. 2.

FRAZIER, William E. Metal additive manufacturing: A review. **Journal of Materials Engineering and Performance**, vol. 23, n° 6, p. 1917–1928, 2014. https://doi.org/10.1007/s11665-014-0958-z.

FROMM, E.; JEHN, H. Reactions of niobium and tantalum with gases at high temperatures and low pressures. **Vacuum**, vol. 19, n° 4, p. 191–197, 1969. https://doi.org/10.1016/s0042-207x(69)80101-6.

GHOSH, G; OLSON, G B. Integrated design of Nb-based superalloys : Ab initio calculations , computational thermodynamics and kinetics , and experimental results. **Acta Materialia**, vol. 55, p. 3281–3303, 2007. https://doi.org/10.1016/j.actamat.2007.01.036.

GRIEMSMANN, Tjorben; ABEL, Arvid; HOFF, Christian; HERMSDORF, Jörg; WEINMANN, Markus; KAIERLE, Stefan. Laser-based powder bed fusion of niobium with different build-up rates. **International Journal of Advanced Manufacturing Technology**, vol. 114, n° 1–2, p. 305–317, 1 maio 2021. https://doi.org/10.1007/s00170-021-06645-y.

GU, Dongdong; DAI, Donghua; CHEN, Wenhua; CHEN, Hongyu. Selective laser melting additive manufacturing of hard-to-process tungsten-based alloy parts with novel crystalline growth morphology and enhanced performance. **Journal of Manufacturing Science and Engineering, Transactions of the ASME**, vol. 138, n° 8, 1 ago. 2016. https://doi.org/10.1115/1.4032192.

GUO, Meng; GU, Dongdong; XI, Lixia; DU, Lei; ZHANG, Hongmei; ZHANG, Jiayao. Formation of scanning tracks during Selective Laser Melting (SLM) of pure tungsten powder: Morphology, geometric features and forming mechanisms. **International Journal of Refractory Metals and Hard Materials**, vol. 79, p. 37–46, 1 fev. 2019. https://doi.org/10.1016/j.ijrmhm.2018.11.003.

GUO, Yueling; HE, Junyang; LI, Zhiming; JIA, Lina; SU, Haijun; ZHANG, Jun; ZHANG, Hu. Tuning microstructures and improving oxidation resistance of Nb-Si based alloys via electron beam surface melting. **Corrosion Science**, vol. 163, 1 fev. 2020. https://doi.org/10.1016/j.corsci.2019.108281.

GUO, Yueling; JIA, Lina; KONG, Bin; WANG, Na; ZHANG, Hu. Single track and single layer formation in selective laser melting of niobium solid solution alloy. **Chinese Journal of Aeronautics**, vol. 31, n° 4, p. 860–866, 1 abr. 2018. https://doi.org/10.1016/j.cja.2017.08.019.

GUO, Yueling; LIANG, Yao Jian; LU, Wenjun; JIA, Lina; LI, Zhiming; PENG, Hui; ZHANG, Hu. Competitive growth of nano-lamellae Nb/Nb3Si eutectics with enhanced hardness and toughness. **Applied Surface Science**, vol. 486, p. 22–27, 30 ago. 2019. https://doi.org/10.1016/j.apsusc.2019.04.263.

GUPTA, C. K. **Extractive Metallurgy of Niobium**. Boca Raton: CRCPress, 1993.

JENKINS, R; SNYDER, R. **Introduction to X-ray powder diffractometry**. Hoboken: Wiley, 2012. vol. 1.

KARPOV, M. I.; VNUKOV, V. I.; STROGANOVA, T. S.; PROKHOROV, D. V.; ZHELTYAKOVA, I. S.; GNESIN, B. A.; KIIKO, V. M.; SVETLOV, I. L. Effect of Silicon Content on the Microstructure and Mechanical Properties of Niobium–Silicon Alloy. **Bulletin of the Russian Academy of Sciences: Physics**, vol. 83, n° 10, p. 1235–1243, 2019. https://doi.org/10.3103/S1062873819100113.

KASERER, L.; BRAUN, J.; STAJKOVIC, J.; LEITZ, K. H.; TABERNIG, B.; SINGER, P.; LETOFSKY-PAPST, I.; KESTLER, H.; LEICHTFRIED, G. Fully dense and crack free molybdenum manufactured by Selective Laser Melting through alloying with carbon. **International Journal of Refractory Metals and Hard Materials**, vol. 84, 1 nov. 2019. https://doi.org/10.1016/j.ijrmhm.2019.105000.

KASHYAP, S.; TIWARY, C. S.; CHATTOPADHYAY, K. Microstructure and mechanical properties of oxidation resistant suction cast Nb-Si-Al alloy. **Materials Science and Engineering A**, vol. 559, p. 74–85, 1 jan. 2013. https://doi.org/10.1016/j.msea.2012.08.027.

KIM, Jin Hak; TABARU, Tatsuo; SAKAMOTO, Michiru; HANADA, Shuji. Mechanical properties and fracture behavior of an NbSS/Nb5Si3 in-situ composite modified by Mo and Hf alloying. **Materials Science and Engineering A**, vol. 372, n° 1–2, p. 137–144, 15 maio 2004. https://doi.org/10.1016/j.msea.2003.12.010.

KIM, Won-Yong; TANAKA, Hisao; KASAMA, Akio; HANADA, Shuji. Microstructure and room temperature fracture toughness of Nbss /Nb5Si3 in situ composites. **Intermetallics**, vol. 9, p. 827–834, 2001. Disponível em: www.elsevier.com/locate/intermet.

KONG, Bin; JIA, Lina; ZHANG, Hu; SHA, Jiangbo; SHI, Songxin; GUAN, Kai. Microstructure, mechanical properties and fracture behavior of Nb with minor Si addition. **International Journal of Refractory Metals and Hard Materials**, vol. 58, p. 84–91, 1 ago. 2016. https://doi.org/10.1016/j.ijrmhm.2016.04.004.

KOU, Sindo. **Welding Metallurgy**. 2° ed. [S. l.]: John Wiley & Sons, 2002.
LAING, M. Melting point, density, and reactivity of metals. **Journal of Chemical Education**, vol. 78, n° 8, p. 1054, 2001. https://doi.org/10.1021/ed078p1054.

LEONT'EV, L. I.; UDOEVA, L. Yu; CHUMAREV, V. M.; GULYAEVA, R. I.; PANKRATOV, A. A.; SEL'MENSKIKH, N. I.; ZHIDOVINOVA, S. v. Microstructure of a complex Nb–Si-based alloy and its behavior during high-temperature oxidation. **Russian Metallurgy (Metally)**, vol. 2016, n° 1, p. 67–75, 1 jan. 2016. https://doi.org/10.1134/S0036029516010109.

LI, Sheng; HASSANIN, Hany; ATTALLAH, Moataz M.; ADKINS, Nicholas J.E.; ESSA, Khamis. The development of TiNi-based negative Poisson's ratio structure using selective laser melting. **Acta Materialia**, vol. 105, p. 75–83, 15 fev. 2016. https://doi.org/10.1016/j.actamat.2015.12.017.

LI, Yunlong; LIN, Xin; HU, Yunlong; GAO, Xuehao; YU, Jun; QIAN, M.; DONG, Hongbiao; HUANG, Weidong. Microstructure and isothermal oxidation behavior of Nb-Ti-Si-based alloy additively manufactured by powder-feeding laser directed energy deposition. **Corrosion Science**, vol. 173, 15 ago. 2020. https://doi.org/10.1016/j.corsci.2020.108757.

LI, Yunlong; LIN, Xin; HU, Yunlong; KANG, Nan; GAO, Xuehao; DONG, Hongbiao; HUANG, Weidong. Zirconium modified Nb-22Ti-16Si alloys fabricated by laser additive manufacturing: Microstructure and fracture toughness. **Journal of Alloys and Compounds**, vol. 783, p. 66–76, 30 abr. 2019. https://doi.org/10.1016/j.jallcom.2018.12.280.

LIU, Y. B.; LIM, S. C.; LU, L.; LAI, M. O. Recent development in the fabrication of metal matrix-particulate composites using powder metallurgy techniques. **Journal of Materials Science**, vol. 29, n° 8, p. 1999–2007, 1994. https://doi.org/10.1007/BF01154673.

LORIA, E. A. Niobium-Base Superalloys via Powder Metallurgy Technology. **Journal of Metals**, , p. 22–26, 1987.

LOVRIĆ, E; IBRAHIM DINCER, MARC A. ROSEN, Pouria Ahmadi; FALLIS, A.G; IBRAHIM DINCER, MARC A. ROSEN, Pouria Ahmadi; FALLIS, A.G; IBRAHIM DINCER, MARC A. ROSEN, Pouria Ahmadi. Investigation of a ceramic metal matrix composite functional surface layer manufactured using gas tungsten arc welding. **Journal of Chemical Information and Modeling**, vol. 53, n° 9, p. 1689–1699, 2019. https://doi.org/10.1017/CBO9781107415324.004.

MANVATKAR, V.; DE, A.; DEBROY, T. Heat transfer and material flow during laser assisted multi-layer additive manufacturing. **Journal of Applied Physics**, vol. 116, n° 12, 28 set. 2014. https://doi.org/10.1063/1.4896751.

MARTINA, F.; MEHNEN, J.; WILLIAMS, S. W.; COLEGROVE, P.; WANG, F. Investigation of the benefits of plasma deposition for the additive layer manufacture of Ti-6Al-4V. **Journal of Materials Processing Technology**, vol. 212, n° 6, p. 1377–1386, 2012. https://doi.org/10.1016/j.jmatprotec.2012.02.002.

MARTINEZ, Edwin; MURR, Lawrence E.; HERNANDEZ, Jennifer; PAN, Xuemin; AMATO, Krista; FRIGOLA, Pedro; TERRAZAS, Cesar; GAYTAN, Sara; RODRIGUEZ, Emmanuel; MEDINA, Francisco; WICKER, Ryan B. Microstructures of Niobium Components Fabricated by Electron Beam Melting. **Metallography, Microstructure, and Analysis**, vol. 2, n° 3, p. 183–189, 1 jun. 2013. https://doi.org/10.1007/s13632-013-0073-9.

MATHIEU, S; KNITTEL, S; BERTHOD, P; MATHIEU, S; VILASI, M. On the oxidation mechanism of niobium-base in situ composites. **Corrosion Science**, vol. 60, p. 181–192, 2012. https://doi.org/10.1016/j.corsci.2012.03.037.

MENDIRATTA, Madan G.; LEWANDOWSKI, John J.; DIMIDUK, Dennis M. Strength and ductile-phase toughening in the two-phase Nb/Nb5Si3 alloys. **Metallurgical Transactions A**, vol. 22, n° 7, p. 1573–1583, 1991. https://doi.org/10.1007/BF02667370.

MENG, Xianyu; LUO, Liangshun; GUO, Nana; SHI, Mingxing; WANG, Fuxin; XU, Yanjin; SU, Yanqing; GUO, Jingjie. Thermodynamic analysis of the interactions between Nb-Si alloy and molding material. **Materials Research Express**, vol. 5, n° 1, 1 jan. 2018. https://doi.org/10.1088/2053-1591/aaa046.

MENON, E S K; MENDIRATTA, M G; DIMIDUK, D M. Oxidation behavior of complex Niobium-based alloys. 2001.

MENON, E. Sarath K; PARTHASARATHY, Triplicane A.; MENDIRATTA, Madan G. Microstructural Effects and Kinetics of High Temperature Oxidation in NB-Si Base Alloys. **Metallic Materials with High Structural Efficiency**. [S. l.]: Kluwer Academic Publishers, 2006. p. 315–326. https://doi.org/10.1007/1-4020-2112-7_32.

MERCELIS, Peter; KRUTH, Jean Pierre. Residual stresses in selective laser sintering and selective laser melting. **Rapid Prototyping Journal**, vol. 12, n° 5, p. 254–265, 2006. https://doi.org/10.1108/13552540610707013.

MITRA, Rahul. Oxidation Behavior of Silicides. **Diffusion Foundations**, vol. 21, p. 127–156, mar. 2019. https://doi.org/10.4028/www.scientific.net/df.21.127.

MITRA, Rahul. **Structural Intermetallics and Intermetallic Matrix Composites**. [S. l.]: CRC Press, 2015. https://doi.org/10.1201/b18434.

MOHAMED, Abd El Moez A.; ZOU, Ji; SHERIDAN, Richard S.; BONGS, Kai; ATTALLAH, Moataz M. Magnetic shielding promotion via the control of magnetic anisotropy and thermal Post processing in laser powder bed fusion processed NiFeMo-based soft magnet. **Additive Manufacturing**, vol. 32, 1 mar. 2020. https://doi.org/10.1016/j.addma.2020.101079.

MULSER, Marco; SEEMÜLLER, Christoph. **Influence of the Processing Technique on the Properties of Nb-Si Intermetallic Composites for High-Temperature Applications processed by MIM and HIP**. [S. l.: s. n.], 2014. Disponível em: https://www.researchgate.net/publication/303933962.

MURAKAMI, T.; SASAKI, S.; ICHIKAWA, K.; KITAHARA, A. Microstructure, mechanical properties and oxidation behavior of Nb-Si-Al and Nb-Si-N powder compacts prepared by spark plasma sintering. **Intermetallics**, vol. 9, n° 7, p. 621–627, 2001. https://doi.org/10.1016/S0966-9795(01)00042-5.

MURAYAMA, Yonosuke; HANADA, Shuji. High temperature strength, fracture toughness and oxidation resistance of Nb-Si-Al-Ti multiphase alloys. **Science and Technology of Advanced Materials**, vol. 3, n° 2, p. 145–156, mar. 2002. https://doi.org/10.1016/S1468-6996(02)00005-0.

OKAMOTO, H. C-W (Carbon-Tungsten). **Journal of Phase Equilibria and Diffusion**, vol. 29, n° 6, p. 543–544, 2008. https://doi.org/10.1007/s11669-008-9396-7.

PAPADIMITRIOU, I.; UTTON, C.; SCOTT, A.; TSAKIROPOULOS, P. Ab initio study of the intermetallics in Nb-Si binary system. **Intermetallics**, vol. 54, p. 125–132, 2014. https://doi.org/10.1016/j.intermet.2014.05.020.

PEART, Joanne. **Powder Electrostatics: Theory, Techniques and Applications**. [*S. l.: s. n.*], 2001.

PERKINS, R. A.; CHIANG, K. T.; MEIER, G. H. **Effect of alloying, rapid solidification, and surface kinetics on the high-temperature environmental resistance of niobium**. [*S. l.: s. n.*], 1987.

PHILIPS, N R; CARL, M; CUNNINGHAM, N J. New Opportunities in Refractory Alloys. **Metallurgical and Materials Transactions A**, 2020. https://doi.org/10.1007/s11661-020-05803-3.

QI, H.; AZER, M.; RITTER, A. Studies of standard heat treatment effects on microstructure and mechanical properties of laser net shape manufactured INCONEL 718. **Metallurgical and Materials Transactions A: Physical Metallurgy and Materials Science**, vol. 40, n° 10, p. 2410–2422, 2009. https://doi.org/10.1007/s11661-009-9949-3.

QIAO, Yanqiang; GUO, Xiping; ZENG, Yuxiang. Study of the effects of Zr addition on the microstructure and properties of Nb-Ti-Si based ultrahigh temperature alloys. **Intermetallics**, vol. 88, p. 19–27, 1 set. 2017. https://doi.org/10.1016/j.intermet.2017.04.008.

READ, Noriko; WANG, Wei; ESSA, Khamis; ATTALLAH, Moataz M. Selective laser melting of AlSi10Mg alloy: Process optimisation and mechanical properties development. **Materials and Design**, vol. 65, p. 417–424, 1 jan. 2015. https://doi.org/10.1016/j.matdes.2014.09.044.

REYES, David; MALARD, Virgil; DRAWIN, Stefan; COURET, Alain; MONCHOUX, Jean-Philippe; MONCHOUX MICROSTRUCTURE, Jean-Philippe. Characterization of high temperature mechanisms in a Nb-Ti-Si alloy. **Intermetallics**, vol. 144, p. 107509, 2022. DOI 10.1016/j.intermet.2022.107509ï. Disponível em: https://hal.archives-ouvertes.fr/hal-03588670.

SALA, Kasturi; KASHYAP, Sunil Kumar; MITRA, Rahul. Effect of Ti addition on the kinetics and mechanism of non-isothermal and isothermal oxidation of Nb–Si–Mo alloys at 900 °C–1200 °C. **Intermetallics**, vol. 138, 1 nov. 2021. https://doi.org/10.1016/j.intermet.2021.107338.

SALSI, Emilio; CHIUMENTI, Michele; CERVERA, Miguel. Modeling of microstructure evolution of Ti6Al4V for additive manufacturing. **Metals**, vol. 8, n° 8, 10 ago. 2018. https://doi.org/10.3390/met8080633.

SAMES, W. J.; LIST, F. A.; PANNALA, S.; DEHOFF, R. R.; BABU, S. S. The metallurgy and processing science of metal additive manufacturing. **International Materials Reviews**, vol. 61, n° 5, p. 315–360, 2016. https://doi.org/10.1080/09506608.2015.1116649.

SANKAR, M.; BALIGIDAD, R. G.; GOKHALE, A. A. Effect of oxygen on microstructure and mechanical properties of niobium. **Materials Science and Engineering A**, vol. 569, p. 132–136, 1 maio 2013. https://doi.org/10.1016/j.msea.2013.01.025.

SAVITSKII, E. M.; BURKHANOV, G. S. **Physical Metallurgy of Refractory Metals and Alloys**. Boston, MA: Springer US, 1995. https://doi.org/10.1007/978-1-4684-1572-8.

SERGI, Alessandro; KHAN, Raja H.U.; GEORGILAS, Konstantinos; MEISNAR, Martina; MAKAYA, Advenit; ATTALLAH, Moataz M. Powder HIP of pure Nb and C-103 alloy: The influence of powder characteristics on mechanical properties. **International Journal of Refractory Metals and Hard Materials**, vol. 104, 1 abr. 2022. https://doi.org/10.1016/j.ijrmhm.2022.105803.

SHABALIN, Igor L. **Ultra-High Temperature Materials I**. [*S. l.*]: Springer, 2014. SHEFTEL, E N; BANNYKH, O A. Niobium-Base Alloys. **Journal of Refractory Metals & Hard Materials**, vol. 12, p. 303–314, 1994.

SINGH, H.; JAIN, P. K. Past, present and future - the characterization of surface topography of plasma transferred arc coatings. **Mechanical and Industrial Engineering, Indian Institute of Technology Roorkee**, n° November, p. 5, 2015.

SMITH, R. THE DEVELOPMENT OF OXIDATION-RESISTANT Increased attention has recently been paid to niobium as the possible base for a new series of materials for use at high temperatures . Conventional creep-resisting alloys are proving inadequate at temperatures above. vol. 2, 1960.

SOLA, Antonella; NOURI, Alireza. Microstructural porosity in additive manufacturing: The formation and detection of pores in metal parts fabricated by powder bed fusion. **Journal of Advanced Manufacturing and Processing**, vol. 1, n° 3, jul. 2019. https://doi.org/10.1002/amp2.10021.

TAN, Chaolin; ZHOU, Kesong; MA, Wenyou; ATTARD, Bonnie; ZHANG, Panpan; KUANG, Tongchun. Selective laser melting of high-performance pure tungsten: parameter design, densification behavior and mechanical properties. **Science and Technology of Advanced Materials**, vol. 19, n° 1, p. 370–380, 31 dez. 2018. https://doi.org/10.1080/14686996.2018.1455154.

TIAN, Y. X.; GUO, J. T.; SHENG, L. Y.; CHENG, G. M.; ZHOU, L. Z.; HE, L. L.; YE, H. Q. Microstructures and mechanical properties of cast Nb-Ti-Si-Zr alloys. **Intermetallics**, vol. 16, n° 6, p. 807–812, jun. 2008. https://doi.org/10.1016/j.intermet.2008.03.005.

TIETZ, T. E.; WILSON, J. W. **Behavior and Properties of Refractory Metals**. Stanford: Stanford University Press, 1965.

TSAKIROPOULOS, P. Alloys for application at ultra-high temperatures: Nb-silicide in situ composites: Challenges, breakthroughs and opportunities. **Progress in Materials Science**, vol. 123, 1 jan. 2022. https://doi.org/10.1016/j.pmatsci.2020.100714.

TSAKIROPOULOS, Panos. On the alloying and properties of tetragonal Nb5Si3 in Nb-silicide based alloys. **Materials**, vol. 11, n° 1, 4 jan. 2018. https://doi.org/10.3390/ma11010069.

VANDENBROUCKE, Ben; KRUTH, Jean Pierre. Selective laser melting of biocompatible metals for rapid manufacturing of medical parts. **Rapid Prototyping Journal**, vol. 13, n° 4, p. 196–203, 7 ago. 2007. https://doi.org/10.1108/13552540710776142.

WANG, Fuxin; LUO, Liangshun; MENG, Xianyu; XU, Yanjin; WANG, Liang; SU, Yanqing; GUO, Jingjie; FU, Hengzhi. Morphological evolution of primary β-Nb5Si3 phase in Nb-Mo-Si alloys. **Journal of Alloys and Compounds**, vol. 741, p. 51–58, 15 abr. 2018. https://doi.org/10.1016/j.jallcom.2018.01.112.

WANG, Na; JIA, Lina; KONG, Bin; GUO, Yueling; ZHANG, Huarui; ZHANG, Hu. Eutectic evolution of directionally solidified Nb-Si based ultrahigh temperature alloys. **International Journal of Refractory Metals and Hard Materials**, vol. 71, p. 273–279, 1 fev. 2018. https://doi.org/10.1016/j.ijrmhm.2017.11.001.

WANG, Qi; WANG, Xiaowei; CHEN, Ruirun; ZHOU, Zhecheng; SU, Yanqing; FU, Hengzhi. Improvement of microstructure and fracture toughness of MASC alloy by element substitution of Zr for Hf. **Journal of Alloys and Compounds**, vol. 892, 5 fev. 2022. https://doi.org/10.1016/j.jallcom.2021.162127.

WANG, Yan Hang; LIN, Jun Pin; HE, Yue Hui; WANG, Yan Li; LIN, Zhi; CHEN, Guo Liang. Reaction mechanism in high Nb containing TiAl alloy by elemental powder metallurgy. **Transactions of Nonferrous Metals Society of China (English Edition)**, vol. 16, n° 4, p. 853–857, 2006. https://doi.org/10.1016/S1003-6326(06)60339-7.

WESTBROOK, J. H.; FLEISCHER, R. L. Intermetallic Compounds Principe and Pratice. vol. 3, n° 9, p. 1689–1699, 2013. https://doi.org/10.1017/CBO9781107415324.004.

WITHERS, P J; BHADESHIA, H K D H. Editorial Board. **Environment International**, vol. 97, p. IFC, 2001. https://doi.org/10.1016/s0160-4120(16)30771-1.

YADROITSEV, Igor; YADROITSAVA, Ina. Evaluation of residual stress in stainless steel 316L and Ti6Al4V samples produced by selective laser melting. **Virtual and Physical Prototyping**, vol. 10, n° 2, p. 67–76, 2015. https://doi.org/10.1080/17452759.2015.1026045.

YANG, Ping Jiong; LI, Qing Jie; HAN, Wei Zhong; LI, Ju; MA, Evan. Designing solid solution hardening to retain uniform ductility while quadrupling yield strength. **Acta Materialia**, vol. 179, p. 107–118, 15 out. 2019. https://doi.org/10.1016/j.actamat.2019.08.024.

YUAN, S. N.; JIA, L. N.; MA, L. M.; JIANG, H.; ZHANG, H. Microstructure and room temperature mechanical properties of hypereutectic Nb-Si based alloy processed by directional solidification. 30., jan. 2014. **Materials Science and Technology (United Kingdom)** [...]. [*S. l.: s. n.*], jan. 2014. vol. 30, p. 75–80. https://doi.org/10.1179/1743284713Y.0000000303.

ZELENITSAS, K. **Study of Niobium Silicide-based alloys for operational temperatures beyond 1150C**. 2005. 2005.

ZHOU, Xin; LIU, Xihe; ZHANG, Dandan; SHEN, Zhijian; LIU, Wei. Balling phenomena in selective laser melted tungsten. **Journal of Materials Processing Technology**, vol. 222, p. 33–42, 2015. https://doi.org/10.1016/j.jmatprotec.2015.02.032.

APPENDIX I

Table 15 – First DoE for LPBF with the Nb47Si20Al mixture

	Sample ID	Laser Power (W)	Sanning Speed (mm/s)	Hatch Space (mm)	Layer Thickness (μm)
A	1	200	300	0,05	30
	2	200	400	0,05	30
	3	200	500	0,05	30
	4	200	600	0,05	30
	5	325	300	0,05	30
B	1	225	300	0,05	30
	2	225	400	0,05	30
	3	225	500	0,05	30
	4	225	600	0,05	30
	5	325	400	0,05	30
C	1	250	300	0,05	30
	2	250	400	0,05	30
	3	250	500	0,05	30
	4	250	600	0,05	30
	5	325	500	0,05	30
D	1	275	300	0,05	30
	2	275	400	0,05	30
	3	275	500	0,05	30
	4	275	600	0,05	30
	5	325	600	0,05	30
E	1	300	300	0,05	30
	2	300	400	0,05	30
	3	300	500	0,05	30
	4	300	600	0,05	30
	5	300	700	0,05	30

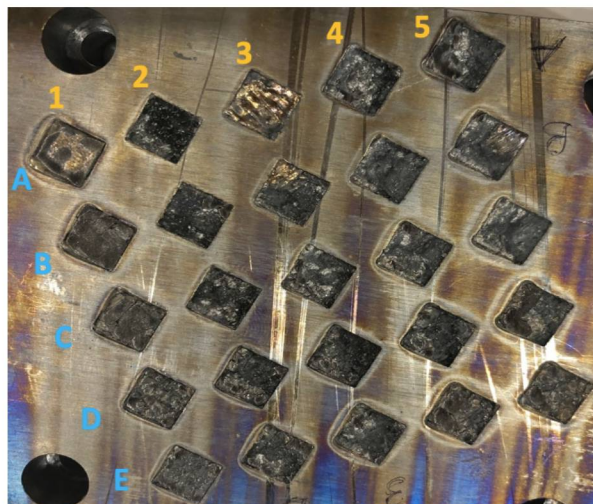Figure 86 - Cubes obtained with the first DoE for LPBF Nb-Si-Al alloy.

Table 16 - Second DoE for LPBF with Niobium-Silicide based alloy.

Sample ID		Laser Power [W]	Scanning Speed [mm/s]	Hatch Space [mm]	Layer Thickness [µm]
A	1	275	1750	0,05	30
	2	325	2250	0,05	30
	3	375	1750	0,05	30
	4	325	1750	0,05	30
	5	325	2250	0,05	30
B	1	225	750	0,05	30
	2	225	1250	0,05	30
	3	225	1750	0,05	30
	4	225	2250	0,05	30
	5	225	2250	0,05	30
C	1	275	750	0,05	30
	2	275	1250	0,05	30
	3	275	1750	0,05	30
	4	275	2250	0,05	30
	5	275	2250	0,05	30
D	1	325	750	0,05	30
	2	325	1250	0,05	30
	3	325	1750	0,05	30
	4	325	2250	0,05	30
	5	325	2250	0,05	30
E	1	375	750	0,05	30
	2	375	1250	0,05	30
	3	375	1750	0,05	30
	4	375	2250	0,05	30
	5	375	2250	0,05	30

Figure 87 - Cubes obtained with the second DoE for LPBF Nb-Si-Al alloy.
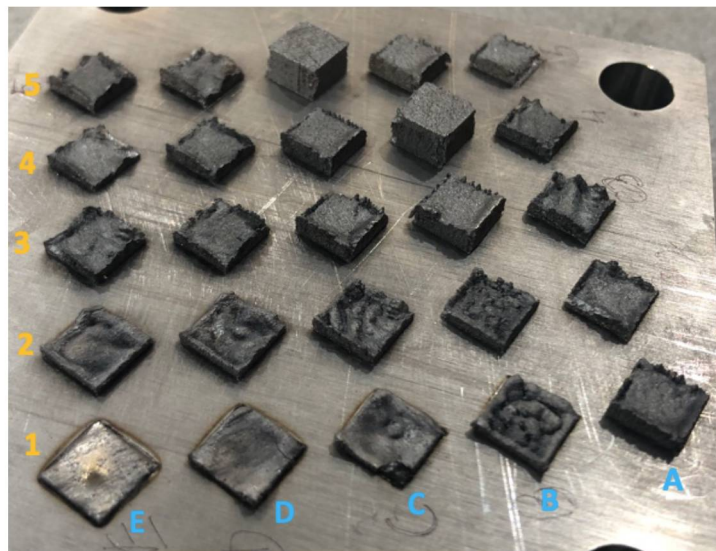
Multilayers processed with NbSiAl powder mixture

Multilayers processed with the ternary powder mixture (Nb47Si20Al) exhibited a very smooth composition gradient across layers, again with a much richer Nb content (88.8-90.6wt%) compared to that of the deposited powder mixture.

As with the binary powder mixture, "in-situ" synthesis of intermetallic compounds, silicides, and aluminides, successfully occurred during deposition of the ternary powder mixture, Figure 89. The presence of Nb_{ss} and the lack of ternary phases can be accounted for by the mentioned exothermal in-situ synthesis and fast solidification rate of intermetallics, together with the high heat input imposed by the selected processing parameters. The absence of ternary phases contrasts with the results from solid state processing reported by MURAKAMI et al. (2001). The formation of alumina and the eventual evaporation of aluminum in the powder mixture during processing may also contribute to preventing the formation of the ternary phase.

Figure 88 - XRD from the top of the multilayers processed with the Nb47Si20Al mixture.
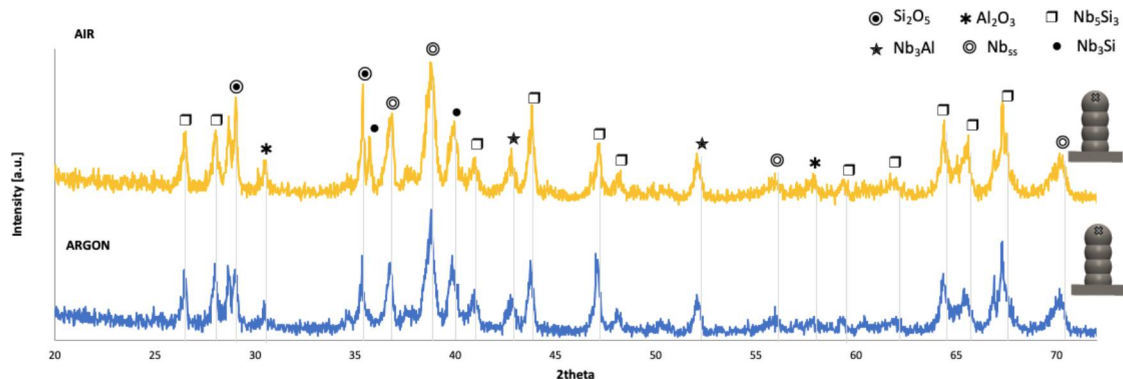

The solidification structure of multilayers processed in both environments exhibits Nb_5Si_3 dendrites with Al in solid solution, surrounded by an interdendritic eutectic containing Nb_{ss}, Figure 90. The major impact from air processing is the larger amount of Al_2O_3 particles (black dots) and the smaller fraction of the Nb_{ss}

phase in the interdendritic eutectic. It is interesting to note that, in spite of controlling the oxygen at 53ppm, small oxide particles still form in multilayers processed in argon environment, suggesting that Al powder particles might have carried oxygen into the melt pool.

Multilayers processed with the ternary powder mixture show a small and reduced number of cracks confined within the Nb_5Si_3 dendrites, as shown in Figure 90 (b). As previously observed with the binary powder mixture, the ductile eutectic Nb_{ss} contributed to mitigate crack propagation throughout the microstructure, as predicted in studies by WANG et al. (2018) and YUAN et al. (2014).

Figure 89 - Bottom layer of the multilayer processed in air (a); bottom layer of the multilayer processed in argon (b) and the EDS composition map (c) of the multilayer processed in air.
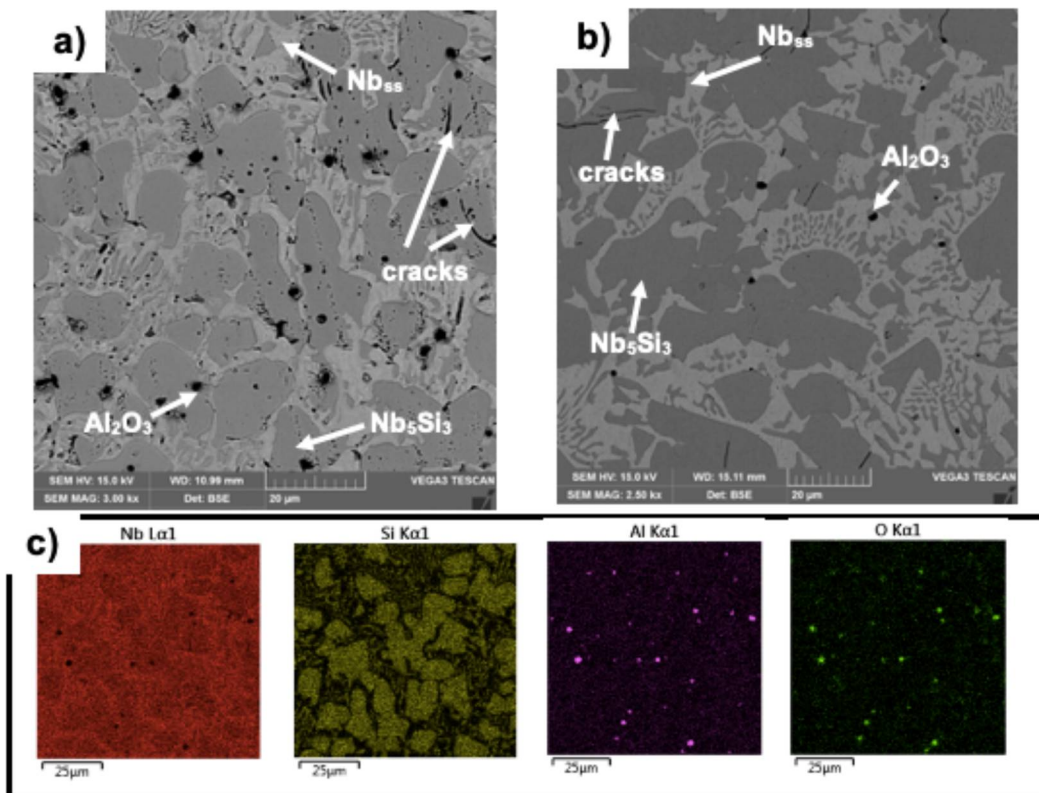
Phase distribution is similar in both multilayers and the observed differences are a consequence of oxygen and aluminum content in solution in the melt pool, Figure 90 (a) and (b). Al trapped in the Al_2O_3 particles depletes the

composition of the solidifying melt pool, as shown by the difference in Al content in phases of builds processed in air and argon, Table 18. The Al content in Nb_{ss} is observed in both environments but processing in argon resulted in a higher Al content in $Nb_{ss,}$ in agreement with the reduced oxide particles in the microstructure. The observed phase distribution agrees with predictions from the phase diagram considering each layer composition. The isothermal section of the Nb-Si-Al ternary phase diagram at 1000°C, Figure 91, reveals that the Nb_5Si_3 and Nb_{ss} phases are stable in a wide composition range (BAETZNER, BEUERS, 2009). Al content up to 8at% stabilizes the Nb_{ss} in the microstructure, whereas high oxygen content induces an Al depletion, shifting the system to compositions that favors the Nb_{ss}/Nb_5Si_3 eutectic.

Table 17 - Average content of niobium, silicon, and aluminum in each phase of the ternary multilayer processed in air (T-air) and the ternary multilayer processed in argon (T-argon), accessed by EDS analysis.

		T-air			T-argon		
		Average composition [at%]			Average composition [at%]		
		Nb	Si	Al	Nb	Si	Al
Powder Mixture		33	47	20	33	47	20
Interdendritic	Nb_{ss}	91.35±0.4	1.48±0.2	**7.15±0.5**	87.50±0.9	2.70±1.1	**9.73±0.9**
	Nb_5Si_3	70.33±4.1	24.10±4.8	5.55±0.9	68.58±2.2	23.85±2.5	7.58±0.3
Dendrite	Nb_5Si_3	64.30±0.2	32.35±0.7	3.35±0.5	64.38±0.3	29.55±1.3	6.10±1

Further consequences of using different processing environments can be assessed by comparing the phase distribution of both multilayers, Figure 92. A change in hardness across layers of ~150HV was measured in multilayers processed in both environments. The higher hardness of multilayers processed in air is associated with the density and dispersion of oxide particles, Al_2O_3. SHCHETANOV et al. (2019) also reported that impurities, such as oxygen, can form oxides that lead to dispersion strengthening.

Figure 90 - Segment of the isothermal section of the Nb-Si-Al ternary phase diagram at 1000°C highlighting the composition of each layer processed in air and argon.
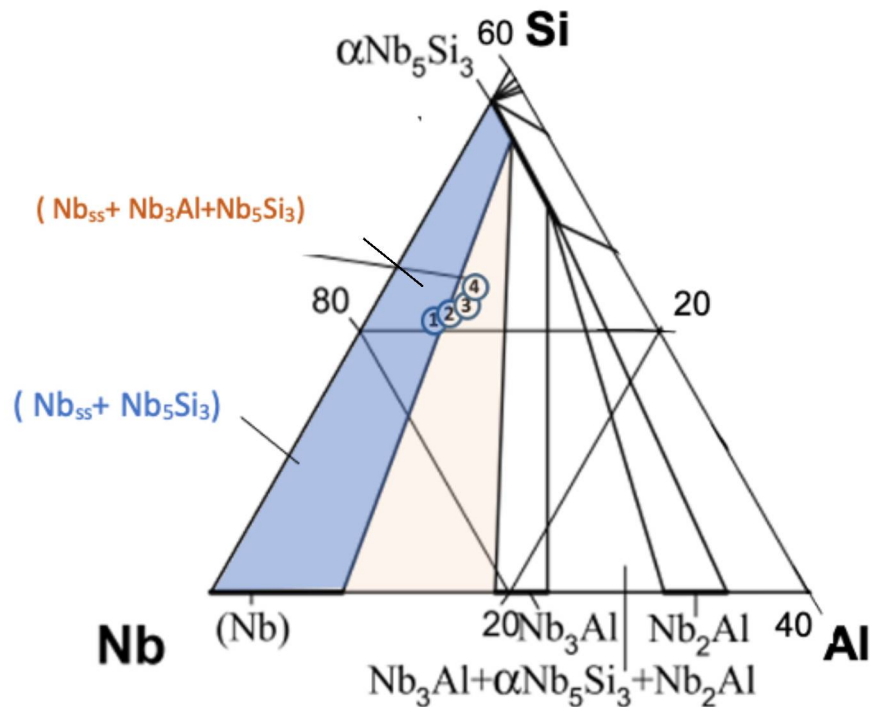

Figure 91 - Ternary alloy microstructure evolution along the multilayers

	1st layer	2nd layer	3rd layer	4th layer
Hardness	749HV	754HV	862HV	912HV
T-air				
Hardness	715HV	811HV	806HV	851HV
T-argon				

Phase analysis at the top layer suggests the presence of intermediate compounds Nb_3Si and Nb_3Al, also identified in the XRD, in a small volume fraction in the solidification structure. Multiple thermal cycles induced the dissolution of these intermediate compounds in previously deposited layers. These compounds are expected to be scattered as a consequence of the segregation and turbulence in the melt pool during the process, which is a typical feature of welding techniques (KOU, 2002). MIN; VADEEV, (2019) reported having mitigated segregation effect during the processing of Nb-Si alloys by adding remelting steps to improve the distribution of alloying elements. Further studies are required to better address the impact of segregation in the microstructure and are outside the scope of this investigation.
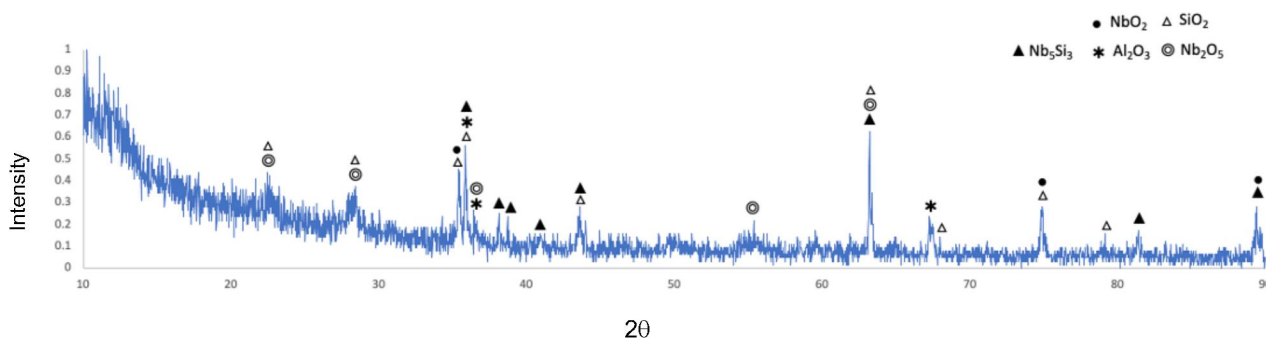
Similarities between multilayers processed with the ternary powder mixture in both environments extended to their behavior under the temperature scan used in DSC and TGA tests, Figure 93. Oxidation behavior assessed by dynamic TG analysis, Figure 93 (b), shows that mass gain is significantly reduced when compared to multilayers processed with the binary powder mixtures in air. Comparing binary and ternary multilayers fabricated in air, the reduction from 25mg mass gain to 11mg (~56%) can be associated with the lack of running cracks and improved soundness of multilayers processed in air with the Nb-Si-Al powder mixture. However, the ternary multilayer processed in argon exhibit poorer oxidation behavior. The 5mg mass gain of multilayers processed with the NbSi powder mixture was increased to 9mg in multilayers processed with the NbSiAl powder mixture, which can be associated with competing growth of oxides at the surface (Nb_2O_5 above 500°C, silica above 800°C and alumina above 1000°C) that does not allow to form a continuous and stable scale.

Figure 92 - DSC and TG analysis of multilayers processed with the Nb47Si20Al powder mixture in air and argon.
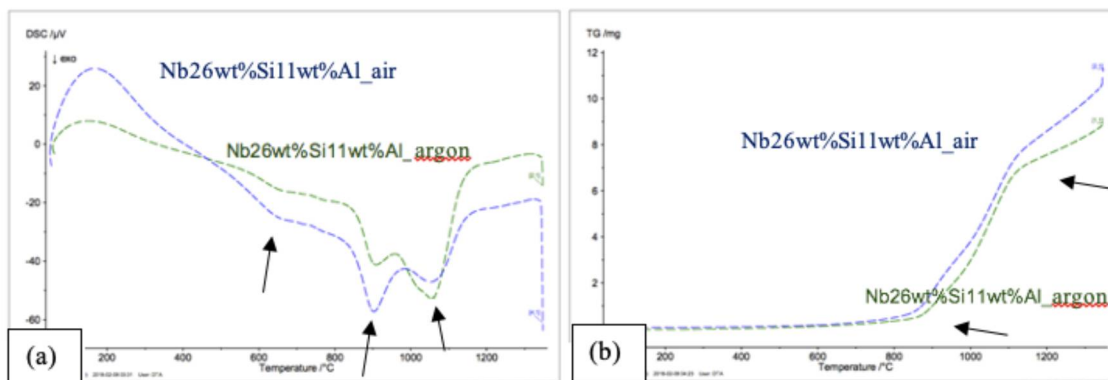
XRD analysis after the oxidation of the Nb-Si-Al layers, show a mixture of oxides together with the Nb_3Si_5 silicide, Figure 94. Similar behavior was reported by MURAKAMI and SASAKI (2003) during their investigation of powder mixtures with a similar composition by spark plasma sintering.

Figure 93 - X-Ray Diffraction of multilayers processed with the Nb47Si20Al mixture after oxidation until 1350°C.

Although multilayers processed in both environments exhibit similar oxidation resistance, processing in argon favored the presence of alumina in the final multi oxide scale, Figure 95. A competitive growth between oxides Al_2O_3, Nb_2O_5, and SiO_2 is observed regardless of the processing environment.
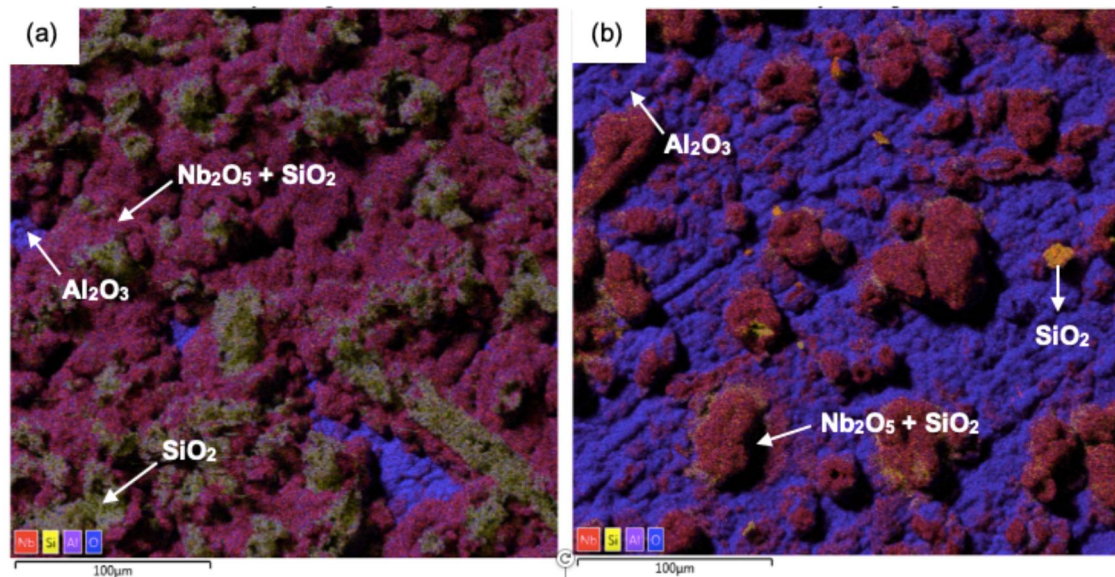
137

Figure 94 - EDS composition mapping of the multilayer processed in air (a) and argon (b), after oxidation.